STUDY OF FERROELECTRIC NANOSHEETS FOR WATER PURIFICATION APPLICATIONS

CAI HAOZHAO

MPhil

The Hong Kong Polytechnic University

2024

The Hong Kong Polytechnic University

Department of Applied Physics

Study of Ferroelectric Nanosheets for Water Purification Applications

CAI Haozhao

A thesis submitted in partial fulfilment of the requirements

for the degree of Master of Philosophy

August 2023

Certificate of Originality

I hereby declare that this thesis is my own work and that, to the best of my knowledge and belief, it reproduces no material previously published or written, nor material that has been accepted for the award of any other degree or diploma, except where due acknowledgement has been made in the text.

_____ (Signature)

_CAI Haozhao__ (Name of candidate)

Abstract

The photocatalytic oxidation process has been widely adopted for the decomposition and degradation of organic pollutants, as well as for the generation of hydrogen through the splitting of water molecules. Due to its environmentally friendly characteristics and economic advantages, this process is gaining increasing significance in the treatment of various wastewater types, particularly those originating from the textile, pharmaceutical, and agricultural industries. However, the practical application effectiveness of semiconductors has been restricted by their inherent limitations, including a wide bandgap, low light absorption capability, and a high electron-hole recombination rate. These factors collectively impede their photocatalytic efficiency. Ferroelectric materials, characterized by a polar unit cell and the ability to display reversible spontaneous polarization upon the application of an external electric field, have garnered significant attention. On the other hand, there is a mounting interest in exploring the impact of ferroelectric polarization on adsorption properties, encompassing both physical adsorption and chemical adsorption. In this study, our objective is to explore the potential of ferroelectric materials for water purification through adsorption and photocatalysis.

In this work, bismuth layer-structured ferroelectric $Na_{0.5}Bi_{4.5}Ti_4O_{15}$ (NBiT) has been chosen as the based material due to its layer structure with strongly anisotropic ferroelectric properties along the c-axis. Also, it is suggested that the reduced the optical band gap and particle size can be promoted through acceptor doping. Fe^{3+} was chosen as the dopant for replacing Ti^{4+} in the NBiT nanosheets because they have comparable radii. 0, 1, 2 mol

of Fe^{3+} and 0, 0.5, 1, 2 mol of excess Fe^{3+} are doped in NBiT nanosheets to fabricate $Na_{0.5}Bi_{4.5}Fe_xTi_{4-x}O_{15}$ + yFe (NBiFeT x-y, x=0,1,2; y=0,0.5,1,2) nanosheets.

To investigate the appropriate mole ratio of the salt mixture and product in molten salt synthesis technique, NBiFeT 0-0 is synthesized using mole ratios of 1:15:15, 1:45:45, and 1:60:60. Based on a comprehensive scanning electron microscope (SEM) analysis, the optimal salt-to-product ratio as 1:60:60. As substantiated by X-ray diffraction (XRD) patterns, all the NBiFeT nanosheets have the standard crystal structure of $Na_{0.5}Bi_{4.5}Ti_4O_{15}$. Furthermore, an expansion of the lattice spacing of NBiFeT nanosheets is resulted after the Fe (exact) doping, resulting in a shift of the XRD pattern towards lower 2θ values. Moreover, the doping induces a reduction in the particle size. Interestingly, it has been found that an excessive amount of Fe leads to the creation of $BiFeO_3$ (BFO), which can improve the adsorption capability. The TEM analysis shows that the exposed plane of the NBiFeT 0-0 nanosheets is primarily {001} facet. The ferroelectric property has also been investigated by the dielectric properties and P-E loop measurements, in the form of ceramic disk. As the temperature increases from room temperature to 100°C, observed remnant polarization (P_r) increase from 0.3 μC/cm² to 1.39 μC/cm², while the observed saturated polarization (P_s) from 1.4 μC/cm² to 3.3 μC/cm². When Fe or an excess amount of Fe is doped into the NBiFeT 0-0 nanosheets, the band gap decreases significantly.

Undoped and Fe-doped NBiFeT nanosheets have been studied for their photocatalytic performances. The results demonstrate a significant degradation rate of 98% for RhB after 180 minutes of irradiation with NBiFeT 0-0 nanosheets. A hypochromic shift is observed in the absorption maximum of the RhB solution during the photocatalytic degradation process. The de-ethylation mechanism of RhB serves as a reliable indicator for the

photocatalytic degradation process. Also, the investigation indicates that the inherent spontaneous polarization within the NBiFeT x-y nanosheets contributes to the enhancement of their photocatalytic performance. Moreover, an investigation into the effectiveness of Fe-doped NBiFeT 0-0 nanosheets for photocatalytic degradation. The degradation efficiency of RhB for NBiFeT 1-0 and NBiFeT 2-0 are 92% and 67%, respectively. About the effect of excessive Fe doping on photocatalytic degradation, the degradation efficiencies of RhB are measured as 98%, 96%, and 90% for NBiFeT 0-0, NBiFeT 0-0.5 and NBiFeT 0-2, respectively. The results highlight a decrease in photocatalytic performance as the increased level of excess Fe doping. Moreover, the results of trapping experiment of active species suggested that superoxide radicals ($\bullet O_2^-$) is the main species in RhB photocatalytic degradation. Then, the effect of pH values on photocatalytic performance is examined. The surface activity of NBiFeT 0-0 nanosheets exhibit optimal behavior at a pH of 7.1. Conversely, under alkaline conditions with a pH of 11, the abundance of hydroxyl groups (OH^-) hinders the occurrence of the adsorption effect.

The adsorption capability of Fe-doped NBiFeT 1-0 nanosheets is investigated. Among all the nanosheets, the NBiFeT 1-1 nanosheets exhibit the highest adsorption capability, which can adsorb 92% of RhB. The adsorption capability increases after Fe doping, while the adsorption efficiency of NBiFeT 0-0 is 7% and NBiFeT 1-0 is 67%. On the other hand, the adsorption capability of NBiFeT 2-0 is measured as 22%. The decrease in adsorption capability observed in NBiFeT 2-0 nanosheets should be attributed to the retardation caused by dye molecules within the pore channels. To study the effect of excess Fe doping on adsorption, NBiFeT 1-y (y=0,0.5,1,2) nanosheets have been used. The result demonstrates that by increasing the level of excess Fe doping, the adsorption capability

increased. This should be attributed to the high concentration of Fe, which has the potential to react with Bi during the synthesis process, leading to the formation of $BiFeO_3$. It has been reported that $BiFeO_3$-coated material can enhance the adsorption capability. Additionally, the pH value of the RhB solution also exerts an influence on the adsorption. In an alkaline system, almost no dark adsorption occurs. Conversely, the adsorption capability experiences an enhancement in an acidic environment attributed to the attractive force between nanosheets and RhB dye. Finally, Ni and Eu are doping into the NBiFeT 1-1 nanosheets to enhance their magnetic properties. The M_s value increases from the initial 0.12 emu/g to 1.22 emu/g after the Ni, Eu doping. However, it is important to note that the adsorption capability of NBiFeT 1-1 decreases from 92% to 81% after the magnetism enhancement.

Acknowledgements

Firstly, I would like to extend my deepest appreciation to my chief supervisor, Prof. K. W. Kwok, for his constant patience, unwavering guidance, genuine support, and unwavering encouragement throughout my entire academic journey.

Secondly, I am deeply grateful for the invaluable technical assistance provided by the Materials Research Centre and Applied Physics Department at the Hong Kong Polytechnic University. Their support was instrumental in the successful completion of my experiment. Furthermore, I would like to express my sincere gratitude to my colleagues and friends who have created a supportive atmosphere for collaboration, idea sharing, and motivation, especially Mr. Ze Long Wang, Mr. Chiu Shek Wong, Mr. Ki Hei Wong and Mr. Chun Hung Suen.

Finally, I am so grateful to my family for always being there for me with their love, support, and sacrifices. They have always believed in me and encouraged me to achieve my goals. I couldn't have made it this far without their unconditional backing, and I am forever thankful for them.

Table of Contents

List of Figures

List of Tables

Chapter 1 Introduction

Environmental pollution poses a significant challenge to modern societies, particularly concerning the treatment of wastewater, as industrial production continues to rise. In recent years, the improper handling and unauthorized discharge of colored effluents from industries such as textiles, food processing, papermaking, and related sectors have exacerbated environmental issues [1]. According to Yao et al., the textile industry around the world uses up more than 10,000 tonnes of dyes every year, with an estimated 100 tonnes/year being released into water streams [2]. The contamination of groundwater and surface water by these colored effluents poses a potential threat to drinking water sources. Due to their affordability and a vast variety of color variations, synthetic dyes, also known as artificially created dyes, have largely supplanted natural dyes in today's world. The molecular structure of dyes encompasses highly complex arrangements, often characterized by aromatic rings, contributing to their heightened stability and comparatively slower biodegradability [3]. For certain types of dyes, even at low concentration (1 ppm) in water bodies, their presence is readily observable. This has an adverse effect on the ecosystem's aesthetic value as well as its photosynthetic activity. Moreover, specific dyes or their by-products have been identified as having toxic, mutagenic, and carcinogenic properties [4], [5]. They can gravely injure people by interfering with their central nervous, brain, reproductive, and renal systems [6]. Therefore, it is essential to develop effective techniques for removing dye from wastewater.

While various techniques exist for water purification, such as activated carbon adsorption [7], chemical oxidation [8], and biological treatments [9], the potential of ferroelectric materials in adsorption and photocatalysis for dye removal has gained attention in recent years [10], [11], [12]. Ferroelectric materials, with their unique polarization properties, exhibit promising characteristics for interacting with dye molecules through electrostatic forces. This interaction can enhance the adsorption capability and selectivity of the materials. Moreover, the integration of ferroelectric materials into photocatalytic systems can lead to improved charge separation, enhanced light absorption, and prolonged charge carrier lifetimes, resulting in more efficient dye degradation. Recent research studies show that substances with spontaneous polarization exhibit increased effectiveness in photocatalytic reactions [12]. For example, Liu et al. have reported that when compared to $KNbO_3$, polarized $KNbO_3$ has a photocatalytic efficiency for the degradation of PE and PP that is about 210% and 140% higher [13]. Dunn et al. reported $LiNbO_3$ exhibits ferroelectric properties that enhance the photocatalytic degradation of RhB [14]. Also, Zhang et al. have studied that the ferroelectric property of $LiNbO_3$ can enhance the attractive force between the surfaces and the D-cysteine molecules. [15]. The purpose of this research thesis is to investigate the utilization of ferroelectric materials in the water purification through adsorption and photocatalysis.

The first part of this chapter will provide a succinct overview of ferroelectric materials. The functioning mechanisms of adsorption and photocatalysis will next be explored. The most typical dye in industrial applications will next be discussed. Finally, this study's objectives and motivations will be laid forth.

1.1. Introduction of ferroelectric material

Ferroelectric materials show reversible spontaneous polarization due to their polar unit cell when an external electric field is applied [16]. The atomic arrangement of the ions inside the crystal structure is what causes this switchable spontaneous polarization to occur [17]. The perovskite group, the bismuth layer-structured group, the tungsten-bronze group, and the ilmenite compounds group are four separate classifications for ferroelectric materials [18], [19], [20]. All of these have been extensively studied for different applications, such as computer memory, energy harvesting and transducers.

As illustrated in Figure 1.1, $BaTiO_3$ is a typical perovskite oxide within the ABO_3 general formula [21]. Each A and B represents a single cation element or a compound made up of two or more cations. The Pm_3m space group, typified by a straightforward cubic lattice with a basis of five atoms, is the ideal space group to which the high-symmetry structure adheres in its ideal state. The Ti ion is located in the center of this lattice, surrounded by six oxygen atoms. These octahedra are arranged in a simple-cubic network, where Ba atoms fill the larger holes to establish a coordination of 12 nearest neighbors for each Ba atom. However, the cubic structure experiences structural frustration due to the mismatch between the Ti and Ba positions within the holes, resulting in a minor polar distortion. Each transition in BaTiO3 involves minor atomic displacements that are principally controlled by the Ti ion's movement in relation to the oxygen octahedron network and a macroscopic strain.

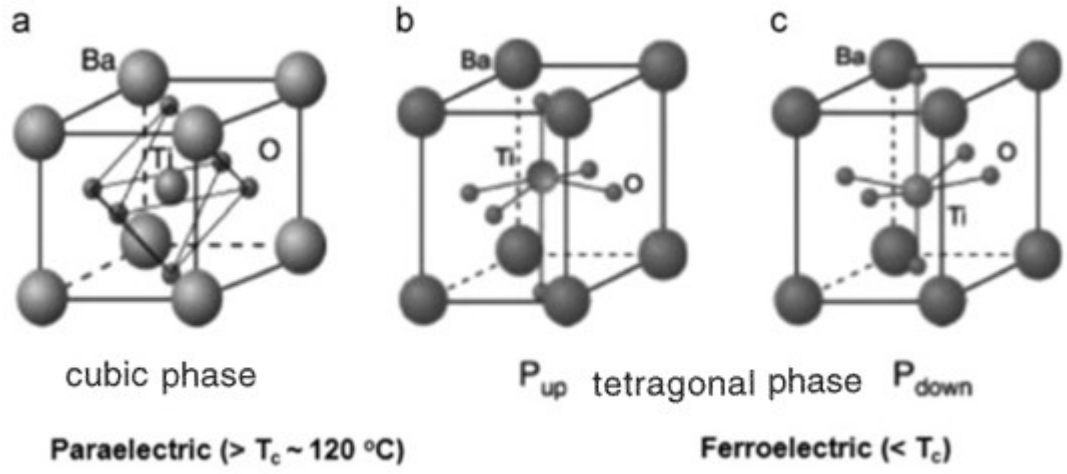

Figure 1.1 The schematic diagram of $BaTiO_3$, which exhibits a tetragonal phase in the ferroelectric phase and a cubic structure in the paraelectric phase [21].

At lower temperatures, the majority of ferroelectric materials structurally change from a paraelectric phase to a ferroelectric phase. The Curie temperature (T_c) is the name given to this transitional temperature [22]. The phase transition from the ferroelectric phase to the paraelectric phase occurs when the material is heated over the Curie temperature [18]. As illustrated in Figure 1.1, when $BaTiO_3$ is subjected to temperatures above 120 °C, it exists in a cubic paraelectric phase, where the Ti atom remains at the geometric center of the structure. Consequently, the crystal structure becomes symmetric, leading to the loss of net polarization and the ferroelectric properties of $BaTiO_3$.

1.1.1. Bismuth layer-structured ferroelectrics

Bismuth layer-structured ferroelectrics (BLSFs) have garnered significant attention alongside the ABO_3-type perovskite piezoelectric materials [23]. Dating back to 1949, Aurivillus et al. synthesized a series of mixed bismuth oxides with the formula $(Bi_2O_2)^{2+}(A_{n-1}B_nO_{3n+1})^{2-}$, where A represents the A-site cation exhibiting 12-coordinate

perovskite structure, B denotes the cation with octahedral coordination, and n signifies the number of octahedral layers. Ordinarily, the pseudo-perovskite layer $(A_{n-1}B_nO_{3n+1})^{2-}$ with Bi^{3+} at the A-site which interleave with the fluorite layers $(Bi_2O_2)^{2+}$ along the c-axis, exhibiting strongly anisotropic ferroelectric properties [24]. The BLSFs can be categorized into four main groups: (1) $Bi_4Ti_3O_{12}$, (2) Bi_3TiNO_9 (N = Nb, Ta), (3) $MBi_4Ti_4O_{15}$ (M = Ca, Sr, Ba, $K_{0.5}Bi_{0.5}$, $Na_{0.5}Bi_{0.5}$), and (4) $MBi_2N_2O_9$ (N = Nb, Ta) [19]. By varying the value of n (Fig. 1.2), different material systems can be obtained, where larger n values correspond to lower Curie temperatures and higher piezoelectric constants.

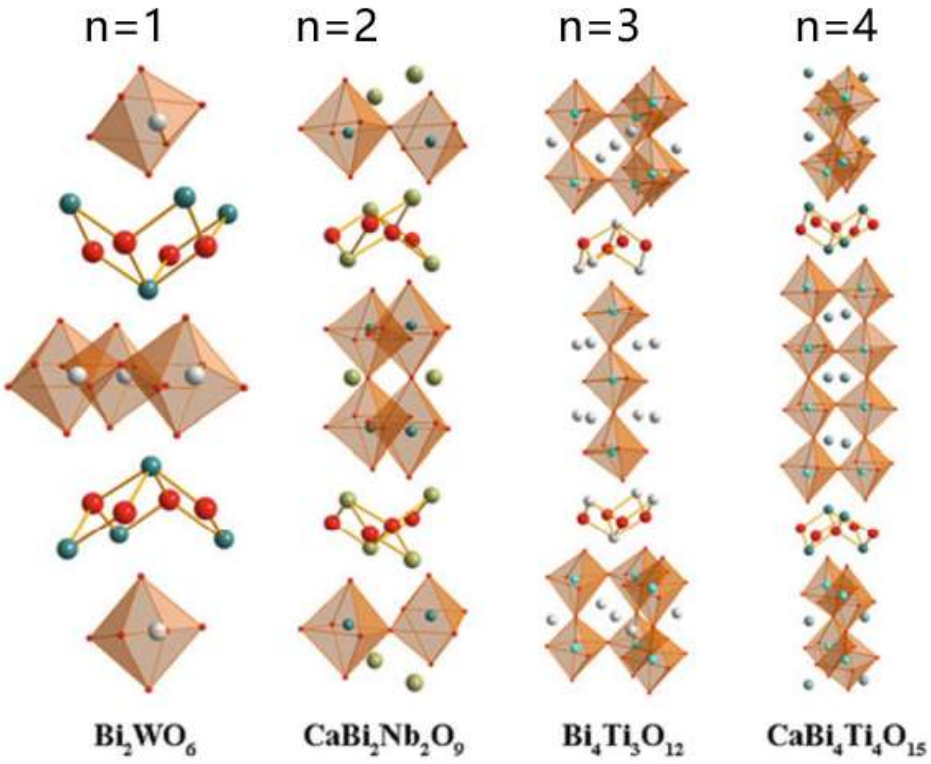

Figure 1.2 The schematic diagram of bismuth layer-structured ferroelectrics [19].

The bismuth layer-structured ferroelectric materials offer numerous advantages. Their well-organized layer-structured effectively prolong the lifetimes of photogenerated carriers and inhibit the recombination of photoinduced carriers [25]. For example, the oxidation and reduction sites are distinctly segregated and isolated on the surface and

edges of the unit layer, facilitating the diffusion of photogenerated electrons and holes to the surface within short distances [26]. Therefore, the holes generated in the layer structured only need to diffuse a small distance to carry out the oxidation process. This fast hole-trapping process enables electrons to freely and efficiently. Recent studies have demonstrated that exposed polarized facets enhance the photocatalytic performance of bismuth layer-structured ferroelectrics (BLSFs) by inducing internal space modifications. For instance, $Bi_4Ti_3O_{12}$ nanosheets with {001} facets exhibit superior efficiency in degrading RhB compared to irregular particles [27]. Additionally, the inherent polarization of $Bi_2O_2(OH)(NO_3)$ nanosheets with active surfaces of {001} makes it easier to separate and transfer photogenerated carriers, leading to exceptional performance in the degradation of a variety of industrial pollutants and medicines [28]. In the study, the BLSFs materials are chosen as adsorbents and photocatalysts.

1.2. Introduction of Photocatalysis

The photocatalytic oxidation process has gained widespread adoption for the decomposition and degradation of organic pollutants, as well as for the generation of hydrogen through water molecule splitting [29], [30], [31]. This process utilizes a photocatalyst capable of harnessing solar energy to start and facilitate specific reduction and oxidation (redox) reactions without being consumed. Due to its environmentally friendly nature and economic benefits, this process is becoming increasingly important in the treatment of wastewaters, particularly those generated by textile, pharmaceutical, and agricultural industries. It has been effective in degrading highly concentrated toxic pollutants with complex chemical compositions and low biodegradability.

In general, photocatalysts with suitable band gaps can utilize solar energy to generate electron-hole pairs. When incoming photons collide with a semiconductor's surface and

have energy equivalent to or more than the semiconductor's bandgap energy, the electrons are excited from valence band to the conduction band. Therefore, the holes will create in valence band after this transition. These holes have the capacity to oxidize donor molecules and interact with water molecules to produce hydroxyl radicals, which have a potent oxidizing effect and are in charge of degrading contaminants. On the other hand, the conduction band electrons interact with dissolved oxygen species, leading to the formation of superoxide ions. These carriers play a crucial role in inducing redox reactions. A schematic representation of the semiconductor photocatalytic mechanism is depicted in Figure 1.3 [32].

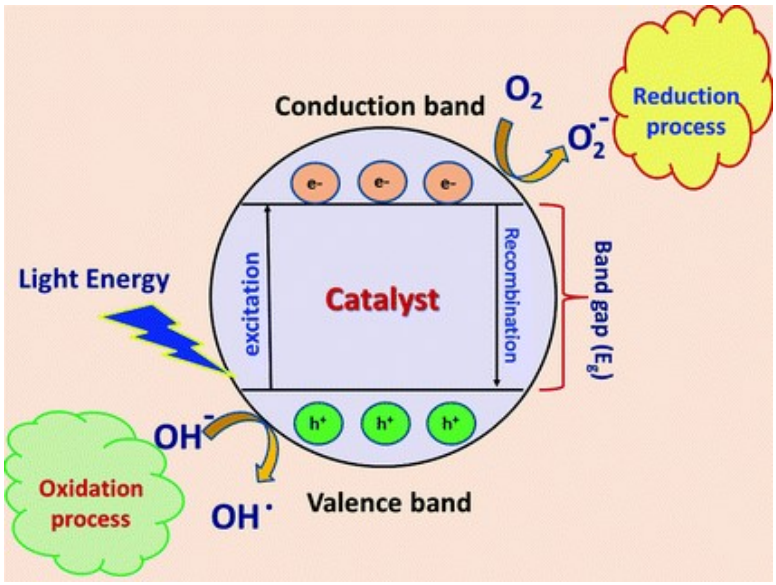

Figure 1.3 The fundamental working principle of photocatalysis [32].

Titanium dioxide (TiO_2) is a semiconductor oxide material that has been extensively studied for its potential uses in photocatalytic applications, such as fuel production, environmental remediation, artificial photosynthesis, and microbial disinfection. This is

largely due to its remarkable stability [33]. However, their effectiveness in practical applications has been limited by their inherent drawbacks, such as a wide bandgap, low light absorption capacity, and high electron-hole recombination rate, which hinder their photocatalytic efficiency. For example, the bandgap of most of the semiconductor oxides are wide (> 3 eV) that limits their solar energy absorption to less than 8% of the solar spectrum. To address these limitations, various strategies, such as doping and heterojunction formation, have been explored to improve the performance of photocatalysis. Among these strategies, composite photocatalysts with heterojunction interfaces have garnered significant attention as they can mitigate the major challenge of high electron-hole recombination rates [33], [34]. Heterojunctions are typically formed by combining semiconductor photocatalysts with noble metals (e.g., Au/TiO_2) and/or other semiconductors (e.g., SnO_2/TiO_2). Due to the different Fermi energy levels, an internal electric field is generated at the junction, resulting in the separation of photo-generated electron-hole pairs and facilitating their migration towards the surfaces for redox reactions. However, relying solely on heterojunctions can introduce technical and production challenges related to stability and compatibility. Therefore, there is a strong need for a single-phase material with a permanent and controllable internal electric field, which would eliminate the complications associated with heterojunctions. Such a material would exhibit an inherent electric field throughout its structure, not limited to a thin heterojunction layer, enabling the efficient separation and transfer of photo-generated charges to the surfaces for redox reactions.

In addition, there is much research on perovskite ferroelectric materials in photocatalysis. For instance, Zhang et al. have studied the photocatalytic activity of Gd-doped $BiFeO_3$ (BFO) nanoparticles [35]. Figure 1.4 shows the photocatalytic degradation of

Rhodamine B (RhB) as a function of the irradiation time under visible light for the as-prepared pure $BiFeO_3$ and Gd-doped $BiFeO_3$ samples. The result shows that only 22% of RhB can be degraded by pure $BiFeO_3$. It is due to the high recombination rate of the photogenerated electrons and holes in BFO [36]. Therefore, there are some methods to enhance the photocatalytic performance including doped materials and formation of heterojunctions [37], [38]. However, these methods may also produce the challenges related to stability and compatibility mentioned above.

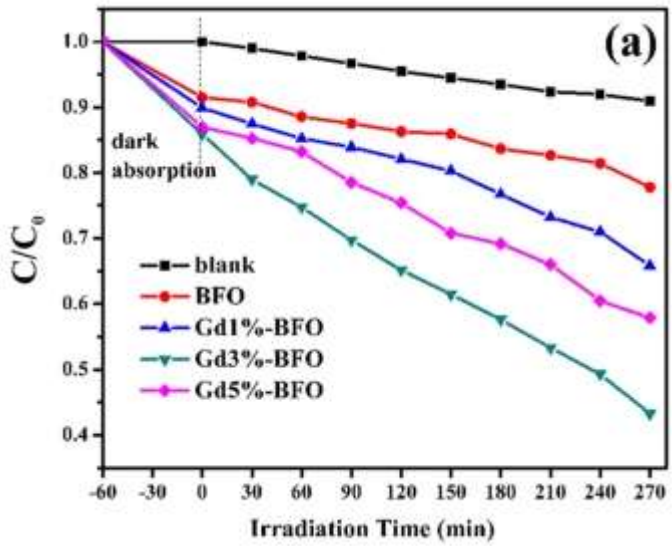

Figure 1.4 The photocatalytic degradation of Rhodamine B (RhB) as a function of the irradiation time under visible light for the as-prepared pure BiFeO3 and Gd-doped BiFeO3 samples [35].

As mentioned, bismuth layer-structured ferroelectrics with spontaneous polarization have the ability to enhance the lifetime of photo-carriers, which is beneficial for addressing the aforementioned issues. Figure 1.5 presents schematic diagrams illustrating the possible photocatalytic mechanism for $SrBi_2Ta_2O_9$ (SBTO) with a ferroelectric polarization field [39]. The layered structure of SBTO facilitates the transfer and separation of photoinduced charges. Under light irradiation, photoinduced electrons mainly transport

through $(A_{m-1}B_mO_{3m+1})^{2-}$, while holes mainly transport through $(Bi_2O_2)^{2+}$, and thus facilitating the reactions of the photoinduced charge carriers with absorbed antibiotics. Furthermore, a significant polar reaction is induced by SBTO's extremely anisotropic crystal structure. There is a significant spontaneous polarization along the c-axis as a result of the Ta-O octahedron's deformation and the perovskite B site's displacement. The photo-induced electrons and holes can build up on opposing sides of the SBTO nanocube because of the internal electric field. Consequently, a greater number of photo-induced charges can participate in the degradation process, thereby enhancing the efficiency of photocatalysis.

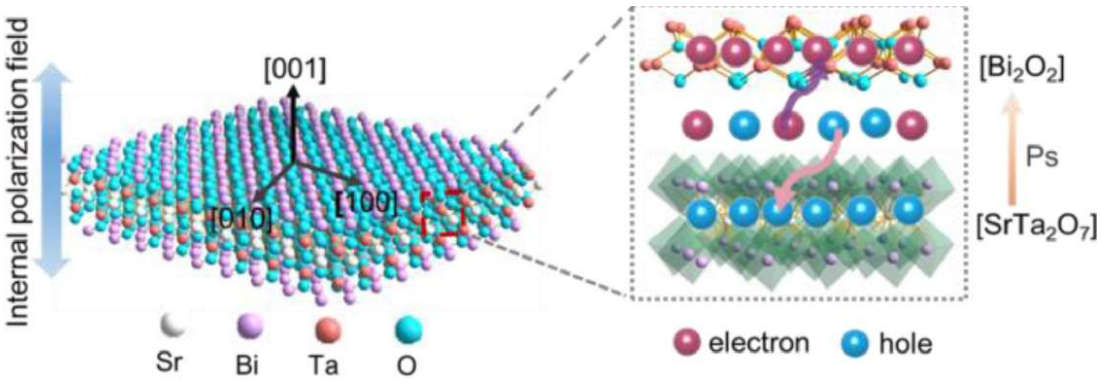

Figure 1.5 Schematic diagrams of $SrBi_2Ta_2O_9$ (SBTO) under visible light irradiation [39].

1.3. Introduction of Adsorption

The process of atoms, ions, or molecules from a gas, liquid, or dissolved solid adhering to the surface of another substance is referred to as adsorption. The material on which adsorption takes place is known as the adsorbent, and the substance that collects at the contact is known as the adsorbate [40]. Chemical adsorption and physical adsorption are the two basic types of adsorptions. Chemical adsorption includes the creation of strong chemical bonds, often by electron exchange, between the adsorbate and the adsorbent

[41]. This kind of adsorption cannot be reversed. However, physical adsorption is reversible because of the weak van der Waals force between the adsorbent and adsorbate [41]. In most cases, adsorption on various adsorbents is primarily governed by physical forces. The primary physical factors that govern adsorption include van der Waals forces, hydrogen bonds, polarity and dipole-dipole interaction [42]. Adsorption is widely recognized as a preferred technique for wastewater treatment, particularly for dye removal, compared to other conventional methods. This is mainly due to its advantages, such as low costs, simplicity and the ability to remove most types of dye [43]. Researchers have proposed a wide range of unconventional and affordable adsorbents, including natural materials, biosorbents, and waste products from different sectors and agriculture. Some examples of these reported adsorbents include clay materials, siliceous materials, agricultural waste materials, and biosorbents [44]. However, the regeneration and disposal of the adsorbent pose challenges. An ideal adsorbent should possess properties such as larger surface area for higher adsorption capability, suitable pore size, and cost-effectiveness [45].

A increasing body of research is being done to determine how ferroelectric polarization affects the characteristics of both chemical and physical adsorption [46], [47], [48]. It is generally known that the domain orientation (c^+/c^-) is specific to electron-exchange reactions at liquid-solid interfaces and that the orientation of dipoles can affect adsorption and reaction processes on ferroelectric surfaces [12]. Recent studies have provided compelling evidence for the enhanced adsorption capacity demonstrated by ferroelectric materials. Lin et al. conducted a study on $BiFeO_3/\alpha\text{-}Fe_2O_3$ core/shell composite and reported a remarkable adsorption affinity towards MO molecules [49]. In this study, we anticipate that the small particle size and layered structure of bismuth layer-structured ferroelectrics (BLSFs) will enhance adsorption during the experimental process.

1.3.1. Effect of solution pH

The pH value of a solution, or solution pH, is recognized as one of the key factors influencing the adsorption capacity of adsorbents. The degree of adsorption efficiency relies heavily on the pH value of the solution. Any changes in the pH value can lead to changes in the ionization level of the adsorptive molecule and the surface properties of the adsorbent [50]. Chowdhury et al. investigated the effect of pH value on the adsorption capability Ananas comosus leaf powder [51]. They observed that the maximum dye removal ratio occurred at a solution pH of 10. The point of zero charge (pH_{pzc}) is a crucial metric that identifies the kind of surface active centers and their capacity for adsorption [52]. It describes the pH value at which a material's surface charge is zero and is frequently used to describe a surface's electrokinetic characteristics [52].

1.4. Introduction of Rhodamine B

Rhodamine B (RhB), classified as a xanthene dye, belongs to the category of cationic dyes [53]. It has gained wide utilization in various industries due to its remarkable water solubility, exceptional brightness, and good stability [54]. Additionally, RhB has been found suitable for numerous biological applications [55]. The molecular structure of RhB is depicted in Figure 1.6 [53]. RhB exists as a reddish-violet colored powder and possesses a molecular formula of $C_{28}H_{31}N_2O_3Cl$, with a molecular weight of 479 g/mol [56]. Among the xanthene dyes, it is recognized as the most toxic [57]. RhB demonstrates high solubility in water and is commonly employed as a synthetic dye with a long history of use [58]. RhB dyes offer certain advantageous qualities, but they also pose several environmental and health risks. They are often harmful to the environment, neurotoxic, and cancer-causing [56]. Moreover, RhB has the potential to irritate the respiratory tract, eyes,

and human skin. RhB cannot be degraded in the absence of light due to its persistence. Similarly, RhB cannot undergo degradation in the presence of light without the addition of a photocatalyst [59].

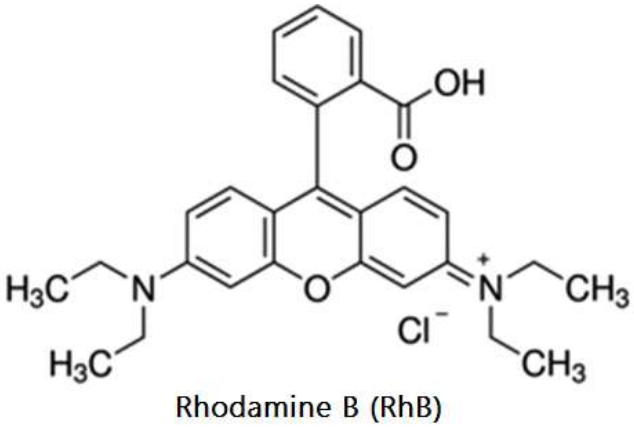

Figure 1.6 The structure of Rhodamine B [53].

Due to the detrimental health and environmental effects caused by RhB dyes, various techniques have been employed to remove them from wastewater; however, these methods are not without limitations. As a result, alternative approaches are being investigated for their efficient removal. Among these methods, photocatalysis and adsorption have been extensively explored. Although these techniques have demonstrated effectiveness, their implementation requires materials that can serve as both photocatalysts and adsorbents. Unfortunately, many of the currently available adsorbents and photocatalysts possess undesirable properties. Therefore, in this study, the utilization of ferroelectric materials as photocatalysts and adsorbents is being investigated.

1.5. Motivation of Research

Despite the potential of ferroelectric materials in dye removal, further research is needed to explore their applications in adsorption and photocatalysis. Specifically, the synthesis and characterization of ferroelectric-based adsorbents and photocatalysts, as

well as their performance in removing RhB dyes, need to be investigated. Additionally, the process optimization parameters, such as pH value and surface area, must be explored to maximize the efficiency of dye removal using ferroelectric materials.

In this study, we will develop nanosheets based on bismuth layer-structured ferroelectric $Na_{0.5}Bi_{4.5}Ti_4O_{15}$ (referred to as NBiT) for photocatalytic and adsorption applications. The crystal structure of NBiT consists of alternating layers of pseudo-perovskite $(Na_{0.5}Bi_{2.5}Ti_4O_{13})^{2-}$ and bismuth oxide $(Bi_2O_2)^{2+}$ along the c-axis [19]. The spontaneous polarization of NBiT arises from the simultaneous rotation of TiO_6 octahedra in different modes. The displacements of the Ti ions contribute significantly to the polarization within the pseudo-perovskite layers in the a-b plane. The insulating paraelectric layers composed of $(Bi_2O_2)^{2+}$ contribute to the electronic response, such as electrical conductivity. We anticipate that the internal electric field generated by the spontaneous polarization can be efficiently separated photo-induced electron-hole pairs. Specifically, electrons can be transferred to the pseudo-perovskite $(Na_{0.5}Bi_{2.5}Ti_4O_{13})^{2-}$ layers, while holes can migrate to the $(Bi_2O_2)^{2+}$ layers. This characteristic is highly advantageous for reducing the rate of electron-hole recombination and ultimately enhancing the efficiency of photocatalysis. Additionally, NBiT exhibits a high Curie temperature, around 668°C, above which the spontaneous polarization diminishes, making it suitable for applications under harsh conditions.

Based on the conduction and valence band structures, as well as the crystal structure, the excitation across the bandgap in the NBiT involves a charge transfer process from oxygen ions to Ti ions in the TiO_6 octahedra. The efficiency of this charge transfer process is influenced by the difference in electronegativities between these ions [60]. Due to the low electronegativity of Ti compared to O (1.54 vs 3.44 on the Pauling scale), the bandgap

of NBiT is wide (> 3 eV). In contrast, BiFeO3, which is extensively studied for photovoltaic and photocatalytic applications, exhibits a relatively narrow bandgap of approximately 2.7 eV, mainly attributed to the high electronegativity of Fe (1.83) [61]. Furthermore, by doping Fe into $LaNiO_3$, the surface area can be increased, facilitating the formation of a porous structure [62]. Consequently, the adsorption capability will be enhanced. Therefore, our intention is to modify the structure of NBiT by introducing a certain amount of Fe doping at the B-site. It is anticipated that even with a high doping level, the Fe-doped NBiT oxides will retain their ferroelectric characteristics at room temperature due to their high Curie temperature of 668°C.

1.6. Scope of work

The purpose of this research thesis is to investigate the utilization of ferroelectric materials in water purification through adsorption and photocatalysis. The primary objectives include:

(1) Developing the bismuth layer-structured ferroelectrics $Na_{0.5}Bi_{4.5}Fe_xTi_{4-x}O_{15}$ + yFe (NBiFeT x-y, x=0,1,2; y=0,0.5,1,2) nanosheets for dye removal, where x is the amount of Fe doped, y is the excess amount of Fe doped.
(2) Assessing the photocatalytic efficiency of NBiFeT x-y nanosheets.
(3) Evaluating the adsorption capability and selectivity of NBiFeT x-y nanosheets.
(4) Optimizing the process parameters to enhance the performance of NBiFeT x-y nanosheets in water purification.

The thesis consists of six chapters:

Chapter 1 provides the background of dye pollution and the ferroelectric materials. This chapter encompasses a comprehensive review of photocatalysis mechanisms in semiconductor materials as well as bismuth layer-structured ferroelectric materials. Furthermore, the background of adsorption and Rhodamine B are thoroughly discussed. The potential applications of bismuth layer-structured materials as both adsorbents and photocatalysts are explored. Lastly, the motivation and objectives of this study are given.

Chapter 2 introduces the synthesis process of the NBiFeT x-y nanosheets. Addi-tionally, it offers the methods for characterizing the NBiFeT x-y nanosheets' crystal structure, grain size, optical properties, and surface area. The equipment setup for the measurements of the dielectric, ferroelectric property, adsorption, and photocatalytic performance is also provided in this chapter.

Chapter 3 gives the results of crystalline structure, particle size, dielectric, ferroelectric properties of the NBiFeT x-y nanosheets. The studies of the relationship between the ratio of salt mixture, grain size and surface area are also presented in this chapter.

Chapter 4 discusses the photocatalytic performance of the NBiFeT x-y nanosheets. Different pH values of the dye solution are used for studying the relation of solution pH and the photocatalytic performance of the NBiFeT x-y nanosheets.

Chapter 5 demonstrates the adsorption capability of the NBiFeT x-y nanosheets. The adsorption capacities of the NBiFeT x-y nanosheets synthesized under different conditions are compared. In addition, different pH values of the dye solution are used for studying the relation of pH values and the adsorption.

Chapter 6 provides the work's conclusion.

Chapter 2 Methodology

2.1. Sample preparation

$Na_{0.5}Bi_{4.5}Fe_xTi_{4-x}O_{15}$ + yFe (NBiFeT x-y, x=0,1,2; y=0,0.5,1,2) nanosheets were synthesized through molten salt synthesis (MSS). This approach allows for precise control of the particle size of the sample while reducing the reaction temperature and time, thereby conserving energy [63]. The choice of a smaller particle size for our samples is crucial, as it results in a larger surface area, which can significantly enhance the photocatalysis performance and adsorption capability. A thorough mixture of the precursor powders including Bi_2O_3 (99.9%), TiO_2 (99.9%), Na_2CO_3 (99%) and Fe_2O_3 (99.5%) in the stoichiometric ratios was first prepared. The powder mixture will then be well mixed with a salt mixture of NaCl and KCl. The mole ratio of nominal NBiFeT x-y nanosheets to the salt mixture varies from 15 to 60 (1:M: M M=15,45,60.). The salt mixture will be completely molten at 800°C according to the eutectic point for facilitating the dissolution, diffusion, and precipitation of the reactants to form the NBiFeT x-y nanosheets. Different molar ratios were used to optimize the morphology and size of the nanosheets [27]. The overall mixture was heated at different high temperatures (> 800°C) and durations (> 2 h) in air for obtaining the nanosheets with optimum morphology and size. The mixture will then be washed thoroughly with hot de-ionized water to remove the remaining salts. Figure 6 shows the process of the molten salt synthesis.

Additionally, a conventional solid-state reaction method was employed to fabricate the NBiFeT x-y nanosheets into bulk ceramics for the characterization of dielectric and ferroelectric properties.

Figure 2.1 Flowchart of the critical steps of molten salt synthesis [63].

2.2. Characterization

2.2.1. Scanning electron microscope (SEM)

Analyzing specimen surfaces is the best choice with a scanning electron microscope (SEM). To generate an image, it needs to project and scan a concentrated stream of electrons across a surface. The standard configuration of a SEM is shown in Figure 2.2, which also comprises the electron gun (electron source and accelerating anode), electromagnetic lenses to concentrate the electrons, a vacuum chamber containing the specimen stage, and a variety of detectors to gather signals emitted by the specimen [64]. Under the operation mode, the SEM generates a highly focused beam of electrons that impacts the specimen

inside a vacuum chamber. The sample is hit by this electron beam, which scatters primary electrons, secondary electrons, backscattered electrons, and X-rays as well as other important signals. The majority of microstructural characterization investigations are based on these signals since they are simple to gather, and plentiful. In this study, the morphologies and sizes of the samples were studied by SEM using a Tescan VEGA3 microscope.

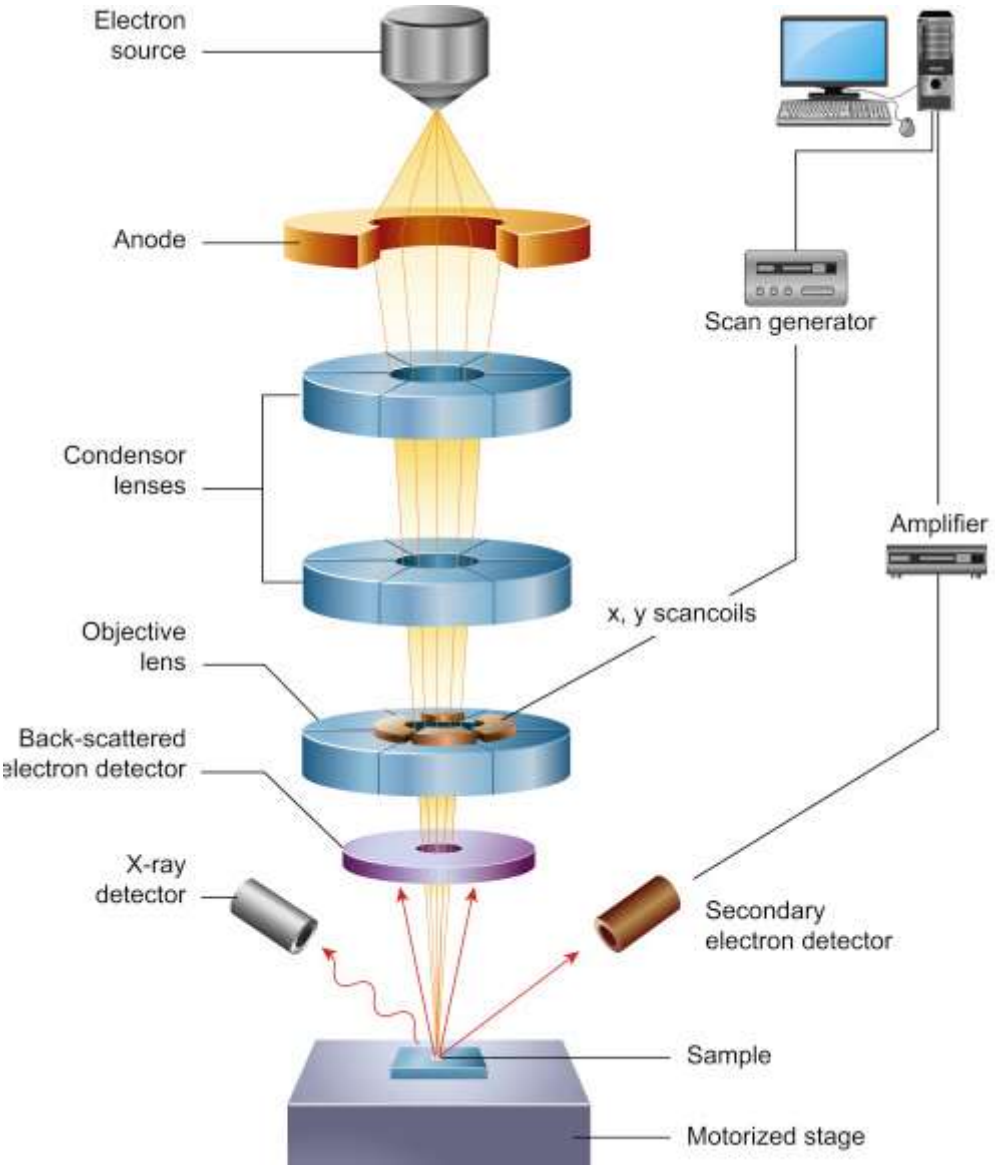

Figure 2.2 The standard configuration of a SEM microscope [64].

2.2.2. Transmission electron microscope (TEM)

The ideal method for analyzing specimens' interior microstructures and assessing nanostructures including particles, fibers, and thin coatings is transmission electron microscopy (TEM). The electron cannon, electrostatic lenses for focussing electrons before and after the specimen, and a transmitted electron detection system are the main elements of a TEM microscope [64]. Figure 2.3 presents a schematic illustration of TEM.

TEM images display variations in contrast based on the way electrons are illuminated, scattered within the specimen, and transmitted through the post-specimen lenses, apertures, and detection system. There have been several different modes developed to achieve maximum benefit from transmission electron microscopy (TEM), including bright-field imaging, high-resolution TEM, scanning TEM, and high-angle annular dark field (HAADF) imaging. These modes make it possible to observe crystal structure, dislocations, and grain boundaries.

In this study, the morphologies and lattice constants of the samples were studied by TEM using a JEOL-2100F electron microscope.

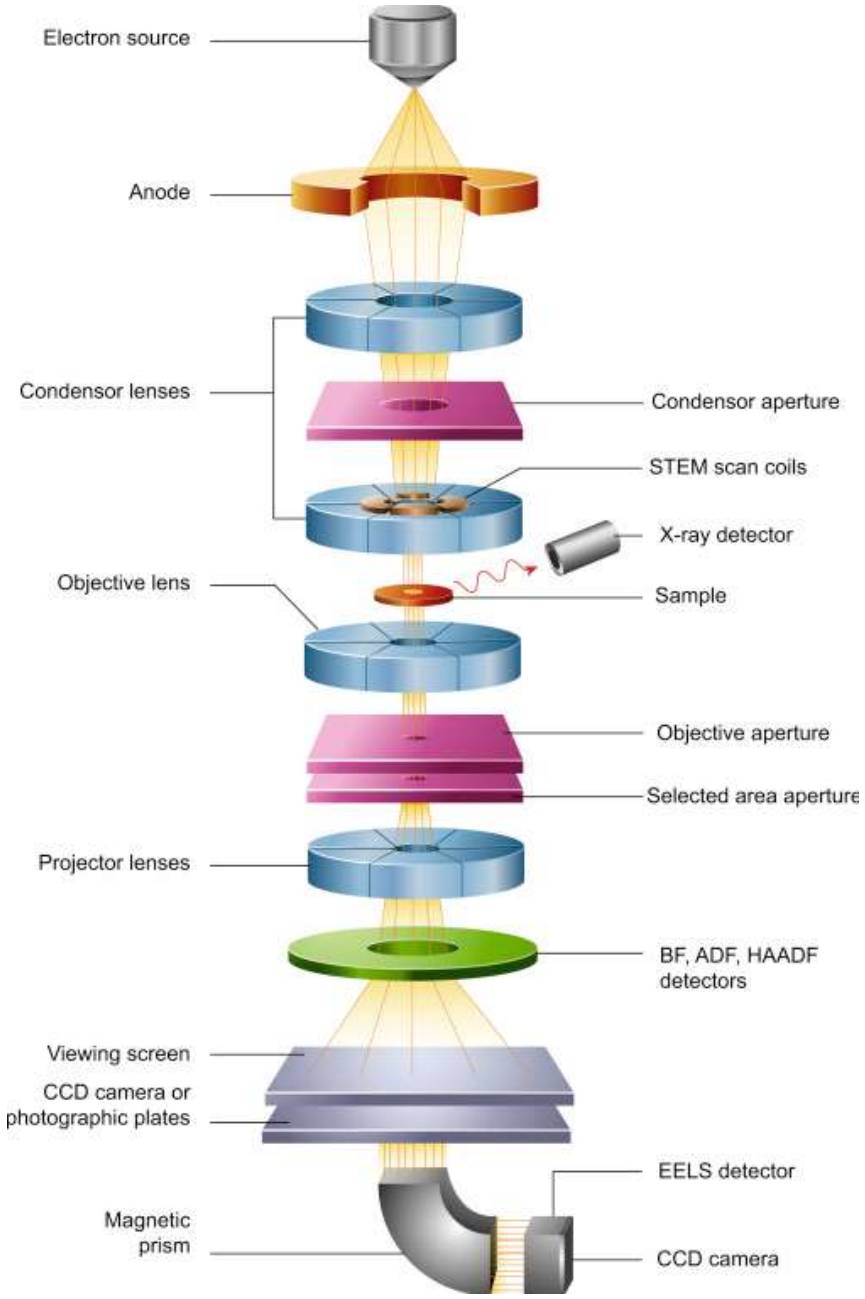

Figure 2.3 The standard configuration of a TEM microscope [64].

2.2.3. X-ray diffraction (XRD)

One technique used to analyze the properties of various types of samples is X-ray diffraction (XRD). This non-destructive method can be applied to powder, solid, and liquid samples. XRD offers crucial insights into the phase composition, crystal structure,

and orientation of materials [65]. Numerous substances are made up of microscopic crystallites, and the chemical makeup and crystallographic structure of these crystals are referred to as the material's "phase". These materials can be composed of either one phase or multiple phases, and may contain both crystalline and non-crystalline elements. X-ray diffractometers can differentiate between various crystalline phases by their unique diffraction patterns.

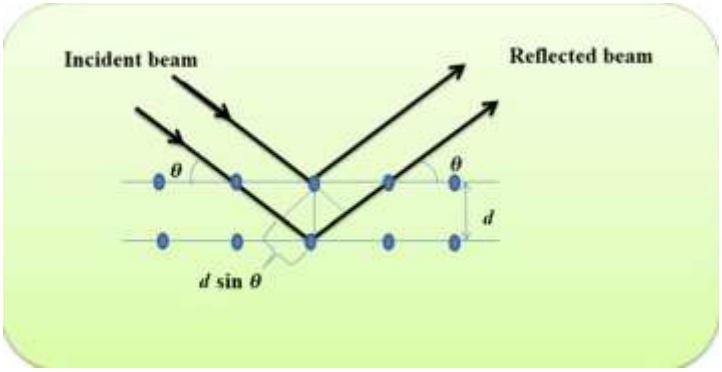

Figure 2.4 The working principle of X-ray diffraction [65].

Figure 2.4 illustrates the working principle of X-ray diffraction [65]. In X-ray generation, a high voltage is applied between the electrodes, causing electrons to be attracted towards a metal target. Upon impacting with the target, X-rays are emitted in all directions. These X-rays are then collimated and directed towards a finely ground powder sample. When X-rays interact with a crystal lattice, scattering occurs. Each crystalline material possesses a distinctive atomic structure, and therefore, it diffracts X-rays in a unique pattern. Bragg's equation is employed to measure the angle of diffraction, which is given by

$$2dsin\theta = n\lambda$$

where d represents the spacing between the planes, θ is the incidence angle, n is the order of diffraction, and λ denotes the beam wavelength [66].

In this study, X-ray diffraction patterns of the samples were collected by a Rigaku SmartLab 9kW - Advance diffractometer over scattering angles from 20° to 80° using Cu Kα radiation.

2.2.4. Piezoresponse force microscopy (PFM)

A potent method for describing the electromechanical coupling in piezo- and ferroelectric materials is piezoresponse force microscopy (PFM). Electromechanical coupling is an intrinsic property that plays a vital role in the functionalities of various material systems [67]. For instance, piezoelectricity is a phenomenon where electric charges accumulate in a material when subjected to pressure or mechanical stress. This effect arises due to the linear interaction between electrical and mechanical states in piezoelectric materials. Additionally, piezoelectricity can exhibit the converse effect, where motion is generated in response to an applied electrical field. The presence of ferroelectricity can be indicated by the PFM images and the PFM hysteresis loops [68].

PFM is based on the principles of atomic force microscopy (AFM). In this technique, a conductive AFM tip applies a local voltage to the surface of the sample for inducing deformation. This localized expansion or contraction causes deflection of the cantilever, and the mechanical response is measured to determine the sample's piezoelectric properties, typically in the order of approximately 1-100 pm/V [67]. The measurement is performed at a high frequency, where the voltage is applied as an AC voltage, and the deflection is measured using a lock-in amplifier at the same frequency. This can improve the signal-to-noise ratio of the measurement, making the results more accurate and reliable. Figure 2.5 shows the experimental setup of PFM.

In this study, the ferroelectricity of the samples was evaluated through the PFM measurement with Asylum MFP-3D Infinity.

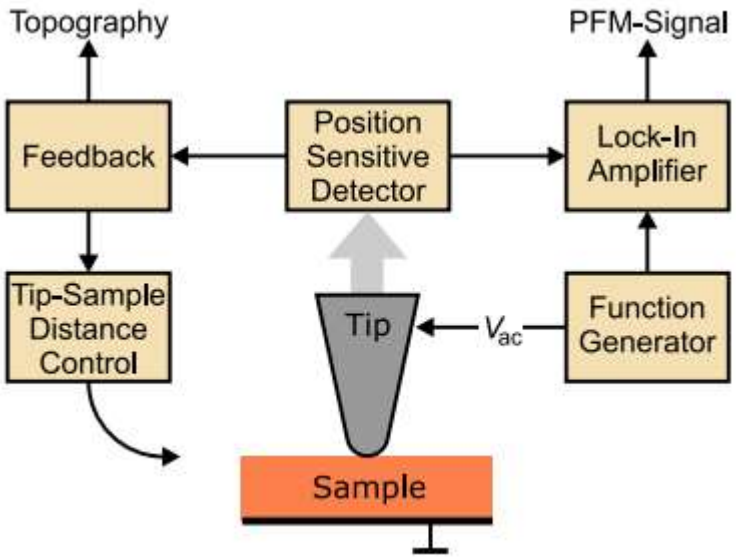

Figure 2.5 The schematic diagram of piezoresponse force microscopy [67].

2.2.5. Brunauer–Emmett–Teller (BET)

A key method used to calculate the surface area of solid or porous materials is the Brunauer-Emmett-Teller (BET) theory. This theory provides crucial insights into the physical structure of materials, as the surface area plays a significant role in determining how a solid interacts with its surrounding environment [69]. Many characteristics of a material, including dissolving rates, catalytic activity, moisture retention, and shelf life, are strongly correlated with its surface area. As a result, surface area analysis holds immense importance in the design and manufacturing of solids, making it one of the most widely utilized methods in material characterization.

The solid sample is first subjected to a vacuum during the surface area measurement. Then, the liquid nitrogen is used to low down the experiment temperature. The solid sample acts as an adsorbent and is exposed to nitrogen gas in controlled increments. After

each dose of nitrogen gas, the system is allowed to reach equilibrium and the weight of the adsorbed nitrogen is measured. The relative pressure (P/P_0) is monitored during the process. This stepwise process allows the calculation of the surface area of the solid material based on the amount of nitrogen adsorbed at different pressures. The BET equation was depicted by:

$$\frac{x}{V(1-x)} = \frac{1}{V_m * c_{BET}} + \frac{x*(c_{BET}-1)}{V_m * c_{BET}}$$

where V represents the volume of adsorbed molecules, V_m denotes the monolayer volume, c_{BET} represents the BET constant, and x represents the relative pressure (P/P_0)[70].

In this study, specific surface areas of the samples were measured by the BET method using ASAP 2020 Automatic Micropore Chemisorption Physisorption Analyzer, equipping with N_2 gas cylinder.

2.3. Optical band gap estimation

To determine the band gap of the samples, a UV-vis spectrophotometer (UV-2550, Shimadzu Co.) was used. The samples were analyzed for diffuse reflectance across a wavelength range of 300 nm to 800 nm. $BaSO_4$ powder was utilized as a reference material during the measurements. Figure 2.6 illustrates the setup of the diffuse reflectance measurement. Subsequently, the band gap of the samples was estimated through the application of the Kubelka-Munk (K-M) function and Tauc plot method.

.

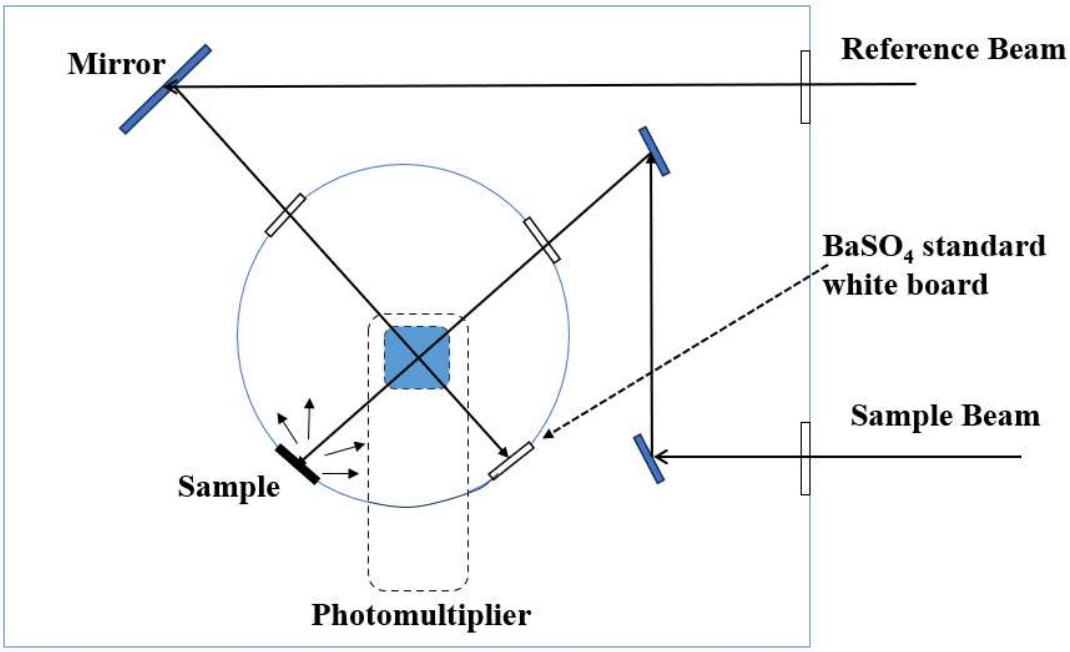

Figure 2.6 The schematic diagram of diffuse reflectance measurement.

The Kubelka-Munk function below can be used to translate the observed reflectance spectra into the matching absorption spectra [71]:

$$\alpha = \frac{(1-R)^2}{2R} = \frac{K}{S}$$

where K and S stand for the absorption and scattering coefficients, respectively, and R is the observed reflectance. The optical bandgap was estimated using the Tauc's plot after the absorption coefficient α was determined. The Tauc equation is expressed as follows:

$$(\alpha h\nu)^n = A(h\nu - E_g)$$

where h is Planck's constant, v is the frequency of the incident photons, A is the slope of the Tauc's plot in the linear region and E_g is the band gap energy. The types of electron transition affects the n factor, where n=2 for the direct permitted transition and n=0.5 for

the permitted indirect transition [71]. For example, Figure 2.7 illustrates the band gap of TiO_2 [71].

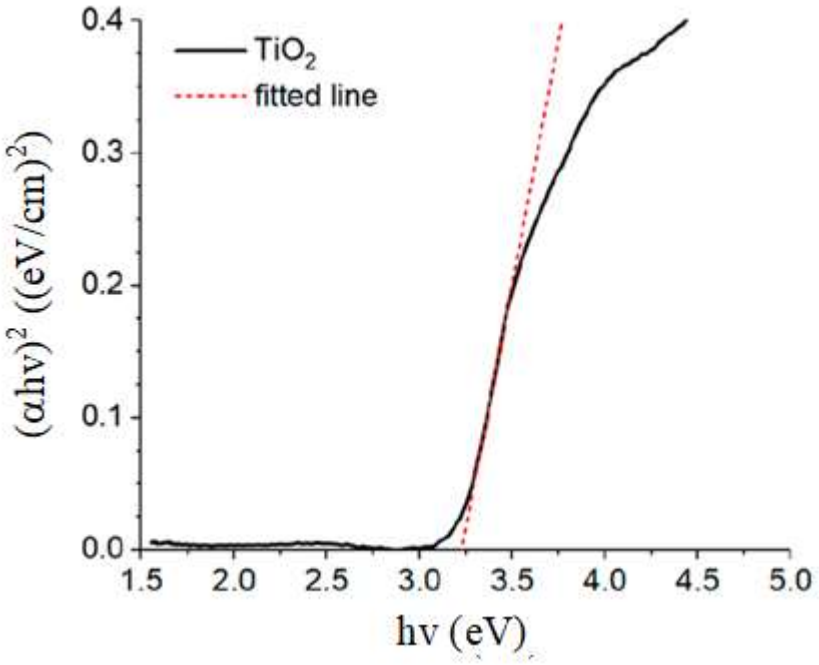

Figure 2.7 The band gap of TiO_2 (3.22 eV) which estimating by Tauc's plot.

2.4. Temperature dependence of dielectric properties

In order to explore the ferroelectric characteristics of the samples in the form of ceramic disk, the temperature-dependent dielectric properties of the samples were determined. The sandpaper was used to smooth out the surfaces of the ceramics, then the silver electrodes were coated on both even and polished surfaces and heated at a temperature of 750°C for 30 minutes. The ceramic samples were then placed on a temperature-controlled probe stage (Linkam HFS600E-PB4) which connected to an impedance analyzer (Hewlett Packard 4194A) for measuring the temperature-dependent dielectric properties. A LabVIEW program was developed to regulate the stage's temperature and collect data from the impedance analyzer. Figure 2.8 shows the setup of the temperature-dependent dielectric measurement.

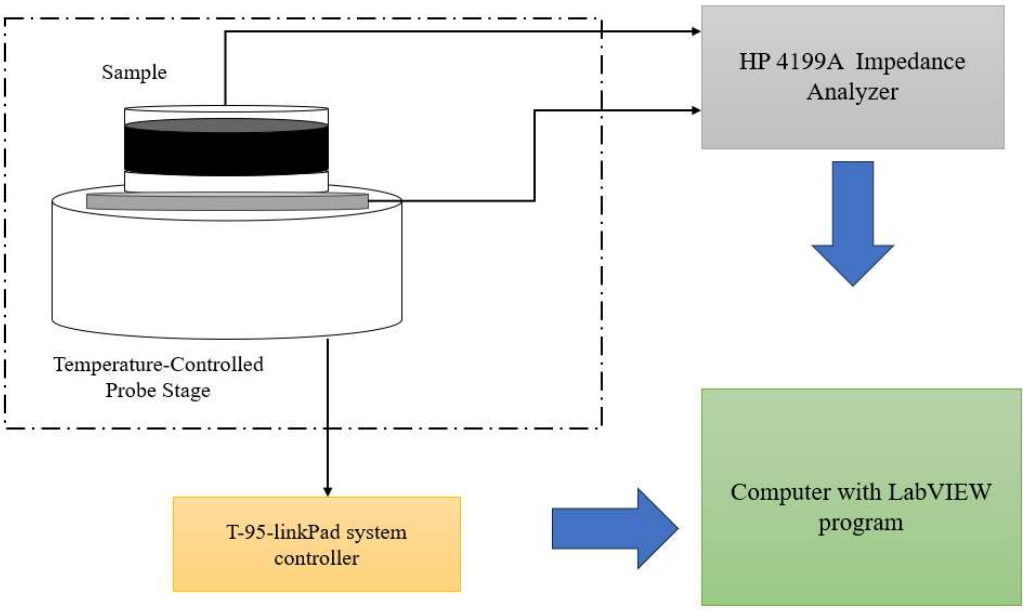

Figure 2.8 The setup for temperature-dependent dielectric measurement.

2.5. Ferroelectric Hysteresis Measurement (P-E loop)

Apart from the temperature-dependent dielectric properties measurements, the ferroelectric hysteresis measurement (P-E loop) can also be used to evaluate the ferroelectric property. The remnant polarization (P_r) and saturation polarization (P_s) of the material can all be determined from the measured P-E loops. The modified Sawyer-Tower circuit was utilized to obtain the P-E loops of ceramic samples at a frequency of 100 Hz. The setup for the P-E loop measurement is shown in Figure 2.9. The ceramic sample was submerged in silicon oil during the experiment to prevent electrical failure. Also, the experiment was conducted at 100 ℃ for facilitating the switching the spontaneous polarization or to "open'' the P-E loop.

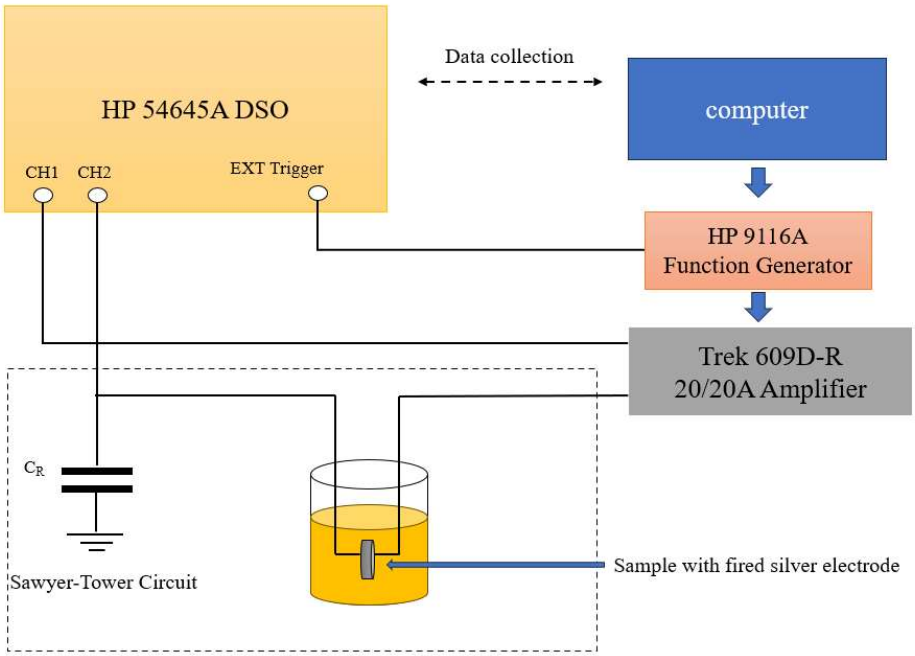

Figure 2.9 The setup for the P-E loop measurement.

A function generator (HP 91164A) produced an AC voltage signal with a sinusoidal waveform, which was then amplified 2000 times using a high-voltage amplifier (Trek 609D-R 20/20A). The charges produced by the sample were collected using a reference capacitor whose capacitance was 1000 times greater than that of the ceramic sample. Then, a digital oscilloscope was used to detect the voltages across the sample and the reference capacitor. A LabVIEW programme was used to record the results. The polarization (P) of the samples was calculated using the following equation:

$$\boldsymbol{P = \frac{C_r V_0}{A}}$$

where A is the silver electrode's area, C_r is the reference capacitor's capacitance and V_0 is the voltage applied across the capacitor.

2.6. Photocatalytic measurements

The photocatalytic performance of the nanosheets were evaluated based on their capability to degrade organic dyes, such as rhodamine B (RhB). A predetermined amount of NBiFeT x-y nanosheets (e.g., 0.4 g) was dispersed in a solution containing the dye (e.g., 10 ppm, 100 mL). Before conducting the photo-degradation measurement, the solution will be continuously stirred in the dark for 30 minutes to achieve an adsorption-desorption equilibrium. During the measurement, the stirred suspension was irradiated at a constant light intensity (e.g., 300mW/cm^2) using a solar simulator with AM1.5 standard spectrum (Newport 91160). At regular intervals (e.g., 40 minutes), a portion of the suspension (5 mL) will be extracted. The nanosheets were be removed from this portion through centrifugation, and the RhB concentration of the remaining solution was analyzed using a UV-vis spectrometer (UV-2550, Shimadzu Co.). The degradation kinetics and photocatalytic performance of the nanosheets were evaluated based on the changes in the RhB concentration.

In this study, the intensity of the light transmitted through the solution was measured and the absorbance at a wavelength of 554 nm was focused used to calculate the RhB Concentration since the absorption band of RhB is 554nm [72]. For calibration purposes, solutions with various RhB concentrations were prepared and the relationship between the measured absorbance and the RhB concentration was determined and shown in Figure 2.10. The slop refers to the specific absorption coefficient and was used to calculate the RhB concentration of the solution collected during the measurement as follows:

$$\text{RhB concentration (mg/L)} = \frac{\text{Absorbance}(a.u.)}{Spe\text{specific Absorption Coefficient (Lmg}^{-1}\text{ cm}^{-1})}$$

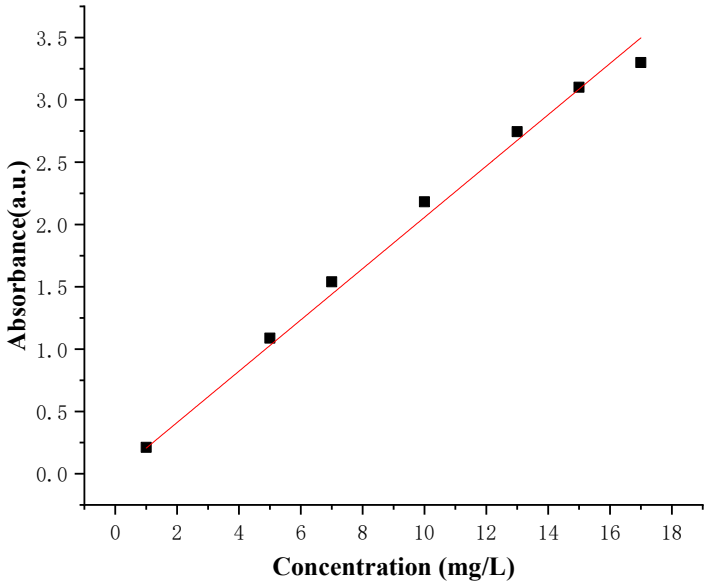

Figure 2.10 Absorbance (peak at 554nm) against concentration.

2.6.1. Active species trapping experiments

To investigate the photocatalytic mechanism, main reactive species (radicals and holes) were detected through radical scavenging experiments during the photocatalytic process. EDTA (h^+ scavenger), benzoquinone (•OH scavenger) and isopropyl alcohol ($•O_2^-$ scavenger) were added into the photocatalytic degradation system for trapping the holes (h^+), hydroxyl radical (•OH), and superoxide radical ($•O_2^-$), respectively. In this study, 1 mmol L^{-1} of EDTA, benzoquinone and isopropyl alcohol were added into 100 mL RhB solution with 0.4g NBiFeT x-y nanosheets. The suspension was then irradiated with a solar simulator for the same duration. Finally, the removal rate of the dye was calculated to determine the main role of active species.

2.7. Adsorption measurement

The dye-adsorption capability of the NBiFeT x-y nanosheets was evaluated based on the amount of adsorbed RhB. A specific quantity of nanosheets (e.g., 0.4 g) was dispersed in a dye solution (e.g., 10 ppm, 100 mL). Subsequently, the solution was continuously stirred in the dark for 80 minutes, and at regular intervals, samples of the solution was taken out. The dye concentration in the solution was analyzed using a UV-visible spectrometer.

2.7.1. Magnetic modification experiment

To enhance the magnetic recyclability of the nanosheets, Ni and Eu were added to the NBiFeT x-y system for improving the magnetism. In this study, 0.1 mol Ni was doped to replace Fe and 0.1 mol Eu was chosen to substitute for Bi. The magnetic properties of the nanosheets were evaluated based on the magnetic hysteresis loops determined using a Quantum Design Physical Property Measurement System (PPMS).

2.8. Effect of pH value

The pH value of the dye solution was adjusted using different amounts of NaOH solution in order to investigate the effect of the pH value on the photocatalytic and adsorption reactions. Prior to adding the adsorbent and photocatalyst, the pH value of the solution was varied within the range of 7 to 11 using NaOH solutions. Subsequently, 0.4 g of NBiFeT x-y nanosheets were introduced into a 10 ppm (100 ml) RhB solution for evaluating the photocatalytic and adsorption performances and then the effect of the pH value.

Chapter 3 Characterization of NBiFeT x-y nanosheets

3.1. Introduction

In this chapter, the characterization results of the NBiFeT x-y nanosheets are discussed. As mentioned in Chapter 1, the surface area plays a crucial role in determining the photocatalytic performance and adsorption capability. A smaller particle size led to a larger surface area, which in turn enhances these properties. Hence, controlling the particle size during the synthesis process becomes essential. Previous research studies have demonstrated that the particle size can be easily regulated by adjusting the amounts of salt mixture in the molten salt synthesis [27]. In this chapter, the particle size analysis of the NBiFeT 0-0 nanosheets synthesized with different M value are presented. The results reveal a significant influence of the amounts of added salt mixture on the particle size, which may subsequently affect the photocatalytic performance and adsorption capability of the samples. Scanning Electron Microscopy (SEM) images show that the NBiFeT 0-0 nanosheets synthesized from a higher amount of added salt mixture exhibits a smaller grain size, which is consistent with the findings of the previous research works.

Furthermore, the ferroelectric properties of the NBiFeT 0-0 nanosheets have been explored through the P-E loop, Piezoresponse Force Microscopy (PFM), and dielectric property analyses.

Additionally, this chapter also presents the material characterizations of the NBiFeT x-y nanosheets doped with exact and excess amount of Fe. The results shed light on the effects of Fe doping, in particular the excess doping of Fe, on the properties of the NBiFeT x-y nanosheets. These results should provide valuable insights into the structural and functional modifications induced by the doping process.

3.2. Characterization of NBiFeT 0-0 nanosheets

3.2.1. Crystalline structure

The crystalline structure of the NBiFeT 0-0 nanosheets prepared by the solid state reaction (SSR) method and prepared by molten salt synthesis (MSS) technique were subjected to examination through X-ray diffraction (XRD) analysis. As illustrated in Figure 3.1, the XRD pattern of the NBiFeT 0-0 nanosheets synthesized by the solid state reaction method is denoted as NBiFeT 0-0 (SSR) while those synthesized by the molten salt method with different M values are denoted as NBiFeT 0-0 (M= 15, 45, or 60). The XRD peaks observed in the range of 20°–80° for all the samples can be well matched with the standard pattern of $Na_{0.5}Bi_{4.5}Ti_4O_{15}$ (JSPDS NO. 74-1318), suggesting that the NBiFeT 0-0 nanosheets with well crystalline structures and phases have been successfully prepared. More specifically, the major diffraction peaks observed for all the samples at 2θ angles of 21.8°, 23.4°, 30.5°, 32.9°, 39.9°, 47.3°, and 48.6°, respectively. These XRD peaks serve as a distinctive fingerprint of the crystalline structure of $Na_{0.5}Bi_{4.5}Ti_4O_{15}$, thereby confirming the successful fabrication of NBiFeT 0-0 nanosheets with different amounts of added salt mixture. The XRD results then provide substantial evidence for the desired crystalline structure and phase formation in the NBiFeT 0-0 nanosheets. For NBiFeT (SSR), the additional diffraction peaks at 35.1° and 44.6° should be attributed to the impurity Bi_2O_3.

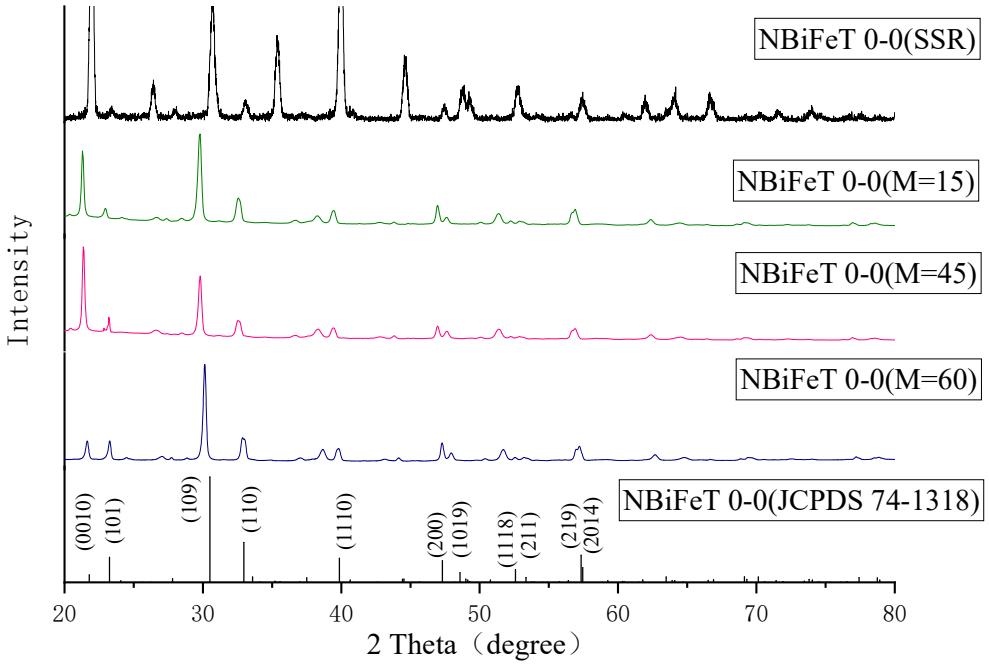

Figure 3.1 The XRD patterns of the NBiFeT 0-0 prepared by SSR and prepared by MMS in difference M values (M=15,45,60) in the range of 20° - 80°.

3.2.2. SEM image of the NBiFeT 0-0 nanosheets

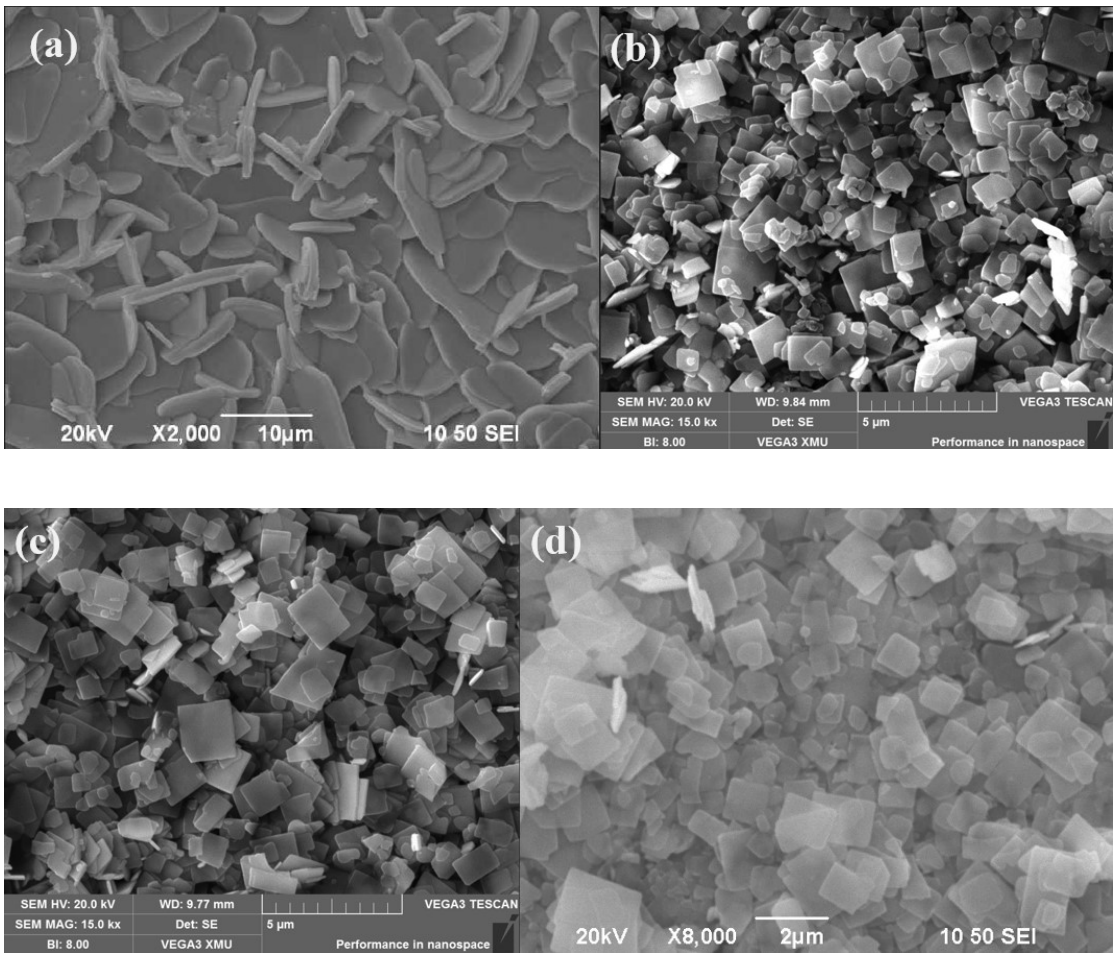

Figure 3.2 SEM micrograph of NBiFeT 0-0 nanosheets prepared by (a) SSR method and MSS in different molar ratio of the NBiFeT nanosheets to salt mixture (b) 1:15:15 (c) 1:45:45 (d) 1:60:60.

The SEM images provided in Figure 3.2 depict the diverse morphological characteristics of the NBiFeT 0-0 nanosheets when synthesized with different amounts of salts mixture. As demonstrated in Figure 3.2a, NBiFeT 0-0 (SSR), i.e., the sample prepared by the SSR method, exhibits irregular particle shapes with a large dimension of 8-10 µm. In contrast, as shown isn Figure 3.2b-d, the nanosheets prepared by the MSS method, i.e.,

NBiFeT 0-0 (M=15, 45, 60) exhibit notably uniform plate-like nanostructures. It is evident that the change in the amount of the added salt mixture can modulate the particle size of the NBiFeT 0-0 nanosheets. As the added salt mixture M increases from 15 to 45 to 60, the average particle size decreases from 2.2 to 1.9 to 1.49 μm. The reduction in the particle size should be attributed to the increase in the mass transport distance between the $Na_{0.5}Bi_{4.5}Ti_4O_{15}$ nanosheets resulted from the higher content of the molten salts (larger M values), which could impede the growth rate of $Na_{0.5}Bi_{4.5}Ti_4O_{15}$ [73].

Based on the SEM results and the synthesis process, a plausible explanation can be put forth to elucidate the evolution of morphology in the synthesized materials under the influence of different molten salts. In the absence of the molten salts, the NBiFeT 0-0 nanosheets may tend to aggregate through inter-plane connections in order to reduce surface energy. This clustering tendency results in the formation of irregular nanosheets [74]. Conversely, the addition of the molten salts significantly curbs the formation of these nanosheet clusters, then impede the growth of NBiFeT 0-0 nanosheets [75].

The findings show that by adjusting the amount of the binary molten salts (NaCl and KCl) used, it is simple to vary the particle sizes of the NBiFeT 0-0 nanosheets by MSS method. In line with theory, the reduction in the particle size is expected to lead to an enhancement in the performance of photocatalytic degradation and adsorption. Consequently, it is reasonable to anticipate that NBiFeT 0-0 (M=60) will engender higher efficiency in adsorption and photocatalytic oxidative degradation of RhB. As a result, NBiFeT 0-0 (M=60) will be used as the main material for the subsequent investigation of the effects of Fe doping.

3.2.3. TEM image of the NBiFeT 0-0 nanosheets

Transmission electron microscopy (TEM) and high-resolution transmission electron microscopy (HRTEM) were employed to provide deeper insights into the microstructure of the synthesized products. The TEM images of the NBiFeT 0-0 (M=60) nanosheet is presented in Figure 3.3a. Clearly, the nanosheet is characterized by a rectangular morphology and a particle size of 1.64 μm, which is in good agreement with the SEM findings as depicted in Figure 3.2d. Figure 3.3b shows the HRTEM images of the NBiFeT 0-0 (M=60) nanosheet. The lattice spacings, as discerned and marked, are measured as 0.272 nm, corresponding to the (1 1 0) atomic planes of $Na_{0.5}Bi_{4.5}Ti_4O_{15}$. The corresponding selected area electron diffraction (SAED) pattern is shown in Figure 3.3c, illustrating that nanosheet belong sto single crystals. Based on the results described above, the in-plane surfaces of the nanosheet lie on (0 0 1) facets as shown in Figure 3.3d.

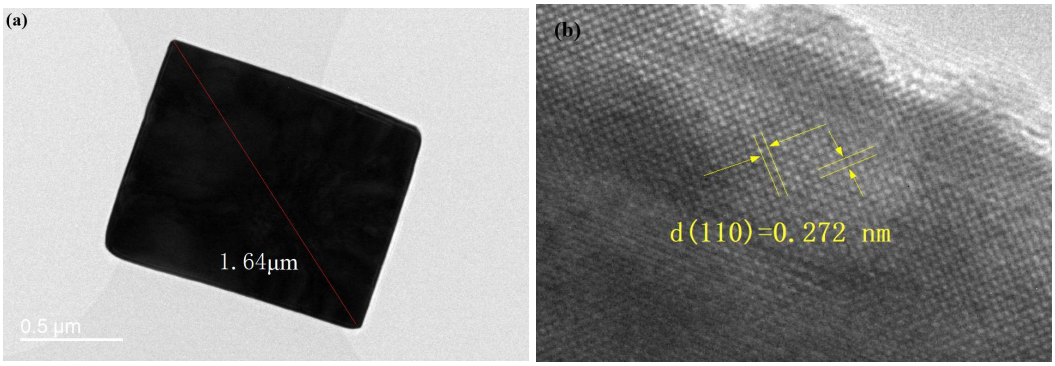

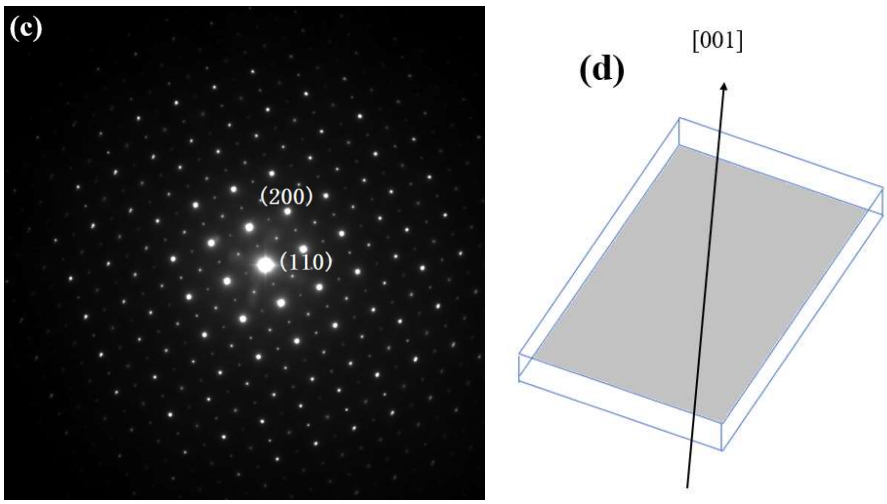

Figure 3.3 (a) TEM, (b) HRTEM and (c) SAED images of NBiFeT 0-0 (M=60) nanosheet prepared by MSS method at 800 °C calcined for 2 h (d) schematic illustration of the crystal orientation of the NBiFeT 0-0 (M=60) nanosheet.

3.2.4. Temperature dependence of dielectric property

The temperature-dependent dielectric properties of the NBiFeT 0-0 (SSR) ceramic sample were measured for investigating the ferroelectric characteristics. The dielectric constant (ε_r) of the sample was measured at a frequency of 1 kHz in a temperature range of 30°C to 400°C, giving the results shown in Figure 3.4. Notably, the observed ε_r exhibits an incremental trend without exhibiting a discernible peak up to 400°C. As discussed in Chapter 1, ferroelectric materials are typically associated with a transition from a ferroelectric tetragonal phase (at low temperature) to a paraelectric cubic phase (at high temperature). This phase transition is characterized by the Curie temperature (T_c). Below Tc, εr generally increases with rising temperature, reaching a maximum at the T_c [76], [77], [78]. Also, the T_c of $Na_{0.5}Bi_{4.5}Ti_4O_{15}$ is 668°C. Therefore, the lack of an observable phase transition at temperatures below 400°C for the sample implies the presence of ferroelectric property, including spontaneous polarization, at room temperature.

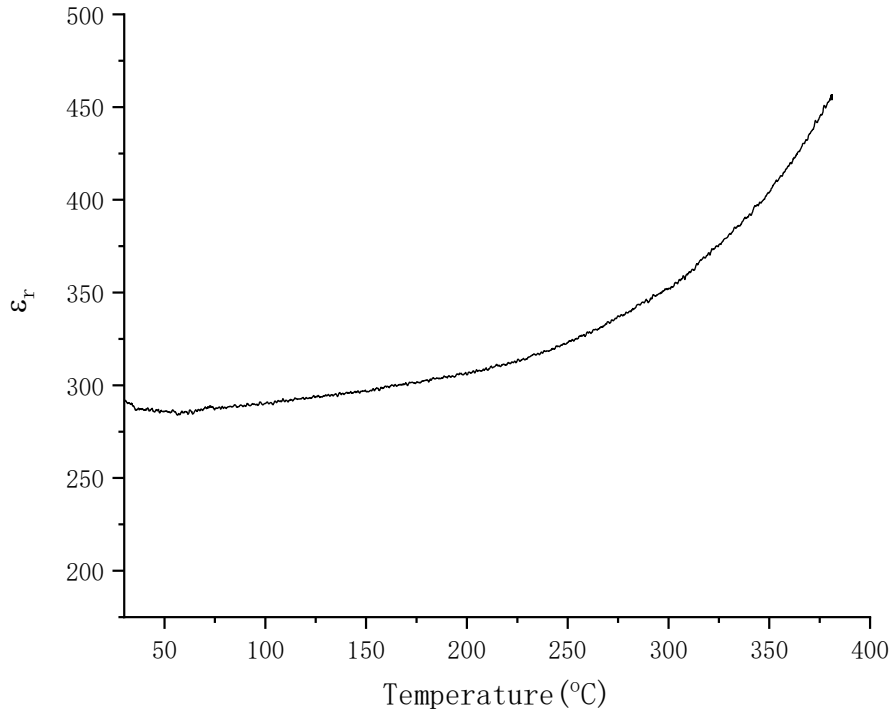

Figure 3.4 Temperature dependence of dielectric constant of NBiFeT 0-0 ceramic at 1 kHz.

3.2.5. Ferroelectric Hysteresis Measurement (P-E loop)

The ferroelectric properties of the NBiFeT 0-0 (SSR) ceramic sample are demonstrated through the P-E loop measurements. The P-E loops were obtained by subjecting the NBiFeT 0-0 (SSR) ceramic to electric fields of 6 kV/mm and 8 kV/mm at a frequency of 100 Hz under both room temperature and 100°C conditions. As depicted in Figure 3.5, the P-E loops confirm the ferroelectric nature of the sample at room temperature. Notably, when the P-E loop measurements were conducted at 100°C, a substantial widening of the P-E loop was observed. Furthermore, increases in the observed saturated polarization (P_s) and remnant polarization (P_r) were noted when comparing the results obtained at room temperature to those at 100°C. Specifically, the observed P_s for the sample increased from

1.4 μC/cm² to 3.3 μC/cm², while the observed P_r increased from 0.3 μC/cm² to 1.39 μC/cm² when the temperature was raised to 100°C. Also, it is difficult to obtain the saturated typical P-E loop since the coercive electric field of the sample is high, which means it needs a higher electric field to switch the ferroelectric domains [79]. The coercive field decreases with increasing temperature, so a substantial widening of the P-E loop was observed at 100°C. This observation validates the consistency between the ferroelectric characterization and the temperature-dependent dielectric property measurements, that the sample exhibits the ferroelectric property at low temperature.

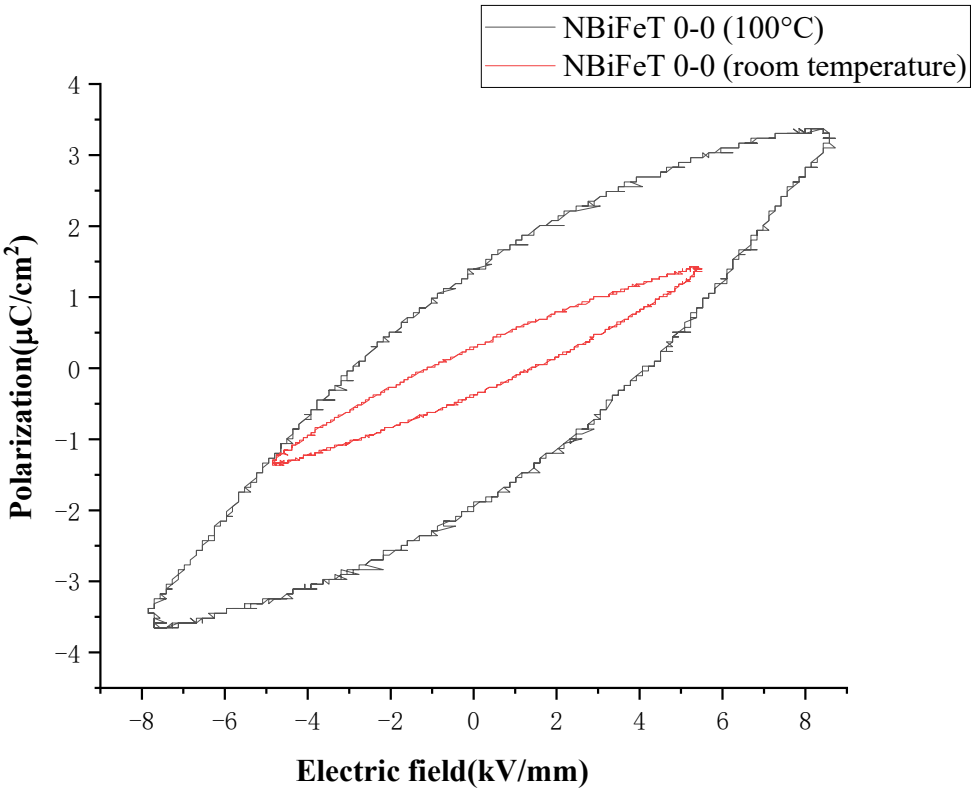

Figure 3.5 The P-E Loops of NBiFeT 0-0 (SSR) ceramic at room temperature and 100°C.

3.2.6. PFM measurement

Figure 3.6 illustrates the topography and phase images of the polished NBiFeT 0-0 nanosheets, as captured through the PFM measurements. The topography of the NBiFeT 0-0 (M=60) nanosheets is depicted in Figure 3.6a, which is in agreement with the observations from TEM and SEM analyses. Additionally, the phase image presented in Figure 3.6b reveals distinct domains exhibiting different phase angles. Notably, the presence of different polarization directions within a single sample is discernible from these images. This observation substantiates the assertion that the NBiFeT 0-0 nanosheets indeed possess inherent ferroelectric properties.

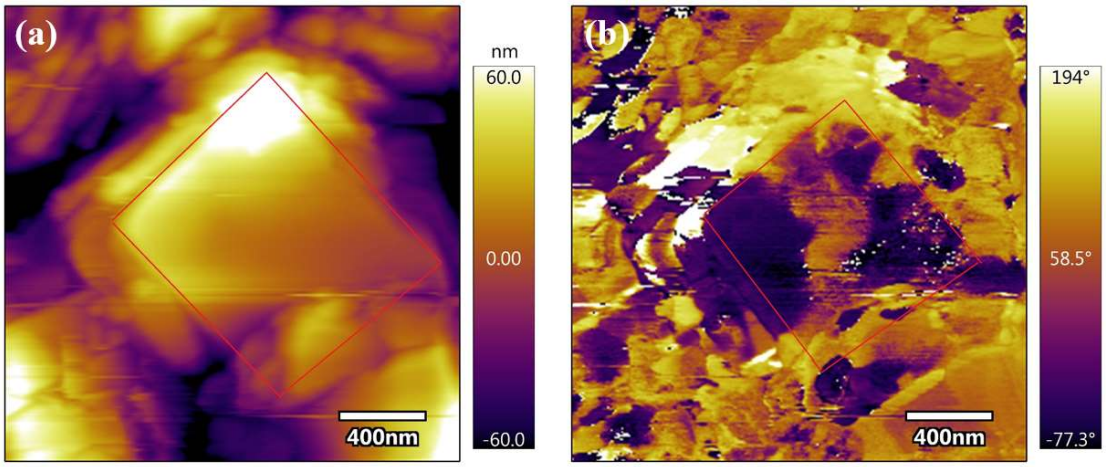

Figure 3.6 (a)The topography and (b) phase images of NBiFeT 0-0 (M=60) nanosheets. The image size is 1.63 x 1.63 μm^2.

3.3. Characterization of Fe-doped NBiFeT nanosheets

3.3.1. Crystalline structure

The XRD patterns of the NBiFeT x-0 (x=0,1,2) nanosheets are presented in Figure 3.7. The patterns show that the most intense peaks appeared of at 2θ angles 21.8°, 23.4°, 30.5°, 32.9°, 39.9°, 47.3°, and 48.6°. These peaks align well with the standard reference $Na_{0.5}Bi_{4.5}Ti_4O_{15}$ (JSPDS NO. 74-1318), confirming the well crystalline structures and phases of the nanosheets. In comparing the XRD patterns of the doped (x=1 and 2) and undoped (x=0) nanosheets, it can be seen that the diffraction peaks of the doped nanosheets shift towards the lower 2θ values. The shift, which increases with the dopant content, should be attributed to the difference in ionic radius and valence between the host ion Ti^{4+} and the dopant Fe^{3+} [80]. The introduction of a new ion with distinct size and valence induces notable lattice distortions. Moreover, the substitution of smaller ionic radius Ti^{4+} with larger Fe^{3+} leads to an expanded interplanar (d) distance in the doped material [62]. These outcomes collectively affirm the successful incorporation of Fe^{3+} in the NBiFeT 0-0 nanosheets.

Furthermore, the XRD pattern of the NBiFeT 2-0 nanosheets contain an additional peak at 2θ of 22.4°, and 32°, which should be attributed to the existence of $BiFeO_3$ (BFO). The increased proportion of Fe_2O_3 during synthesis likely enhances the likelihood of re-action with Bi, resulting in the formation of BFO.

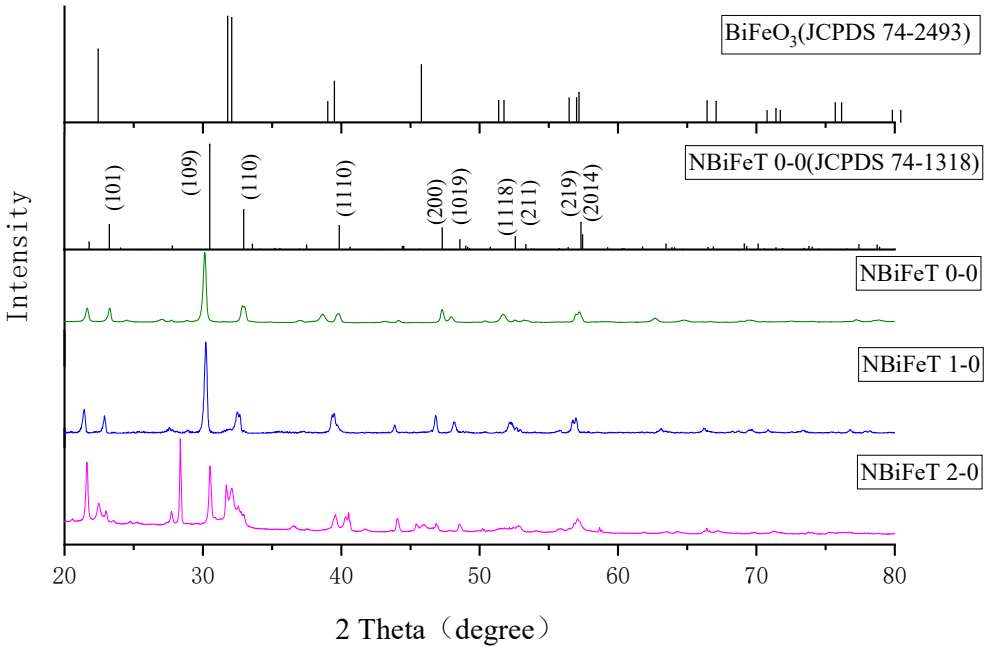

Figure 3.7 The XRD patterns of the NBiFeT x-0 (x=0,1,2) prepared by MMS in the range of 20° - 80°.

3.3.2. Surface morphology

The surface morphology of the NBiFeT x-0 (x=0,1,2) nanosheets has been investigated using SEM, giving the result presented in Figure 3.8. All samples exhibit the characteristic flat-plate structure typical of bismuth layered compounds. As depicted in Figure 3.8, the average particle size of the NBiFeT x-0 nanosheets varies from 1.49 μm for x=0 to 3.82 μm and 2.13 μm for x=1 and 2, respectively. Notably, the average particle size of the nanosheets displays a considerable change as the Fe doping content increases from 0 to 1. This phenomenon could be attributed to the expansion of the interplanar (d) distance in the doped nanosheets [62]. Conversely, the average particle size of the nanosheets decreases as x increase from 1 to 2, implying that the added Fe^{3+} restrains the growth rate of the a-b plane perpendicular to the c-axis, thus impeding particle growth [80].

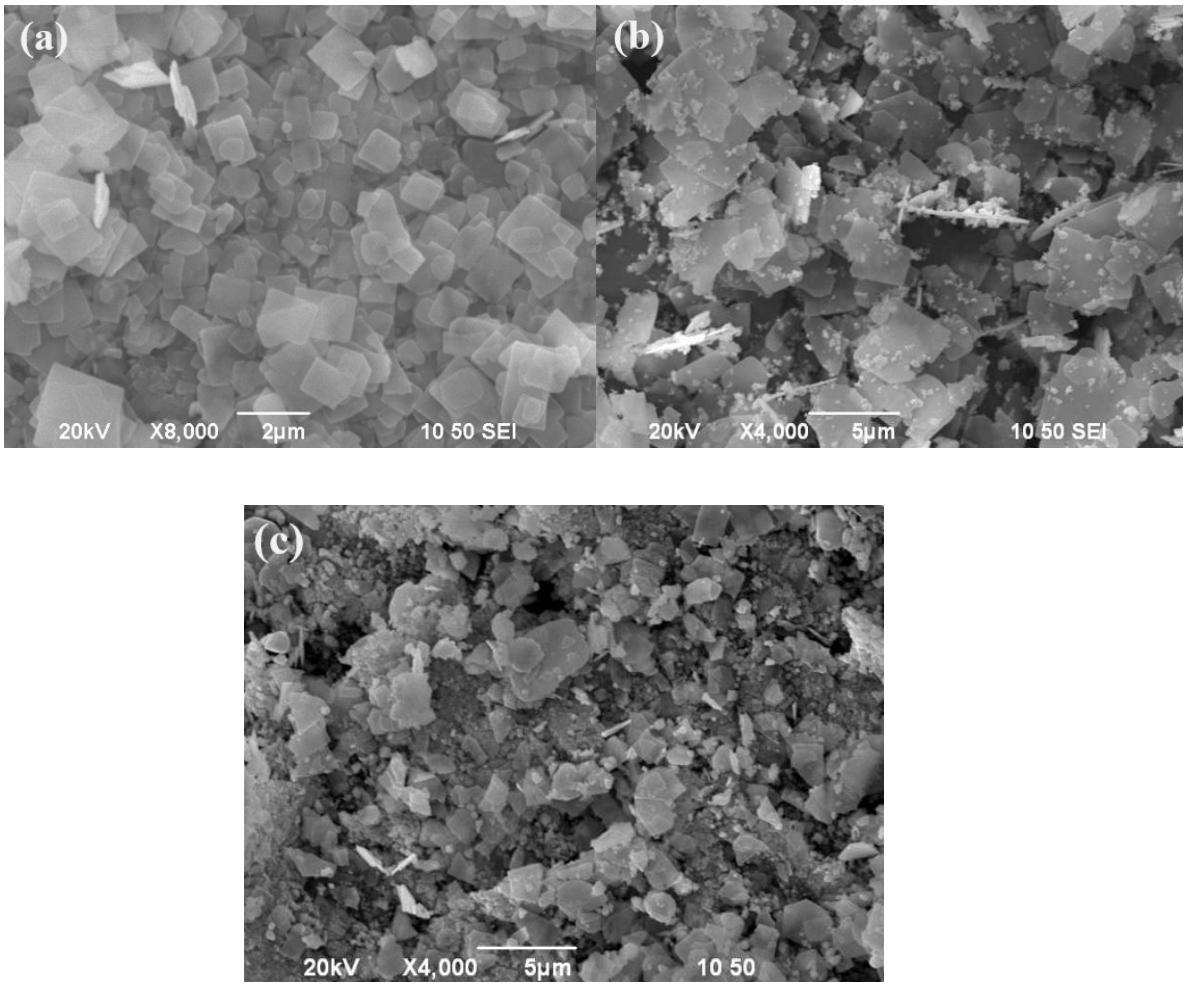

Figure 3.8 SEM of NBiFeT x-y nanosheets (a) NBiFeT 0-0 (b) NBiFeT 1-0, (c) NBiFeT 2-0 nanosheets.

The particle size, shape, and lattice parameters were further evaluated through TEM analysis. Figure 3.9 presents the TEM and HRTEM images of the NBiFeT 1-0 nanosheets. In Figure 3.9a, well-defined nanosheets exhibit a plate- like morphology, with a particle size of 3.82 μm. This observation corroborates the SEM findings as shown in Figure 3.8b. Additionally, Figure 3.3b displays the HRTEM images of the NBiFeT 0-0 nanosheet. The lattice spacing is measured as 0.392 nm, which is higher than that of the undoped nanosheet. This outcome is consistent with the XRD analysis, the Fe-doping increases the lattice parameter.

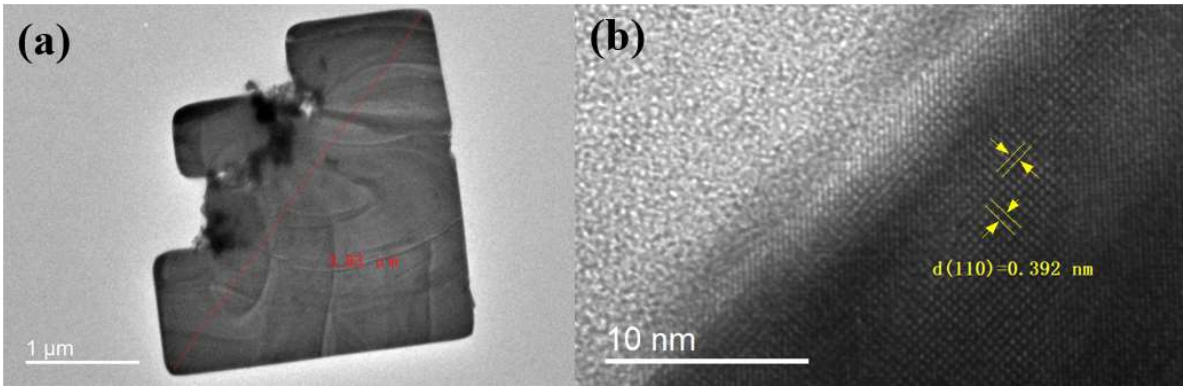

Figure 3.9 (a) TEM (b) HRTEM of NBiFeT 1-0 nanosheets.

3.3.3. PFM measurement

To assess the ferroelectric properties of the Fe-doped NBiFeT nanosheets, PFM measurements were conducted. Figure 3.10 shows the topography and phase images of the NBiFeT 1-0 nanosheet. As shown in Figure 3.10a, several nanosheets are stacked together, displaying varying heights. Furthermore, the phase image presented in Figure 3.10b highlights distinct domains characterized by different phase angles. Notably, these domains exhibit diverse polarization directions even at the same height level. This observation underscores that the ferroelectricity remains preserved in the nanosheets after the Fe-doping.

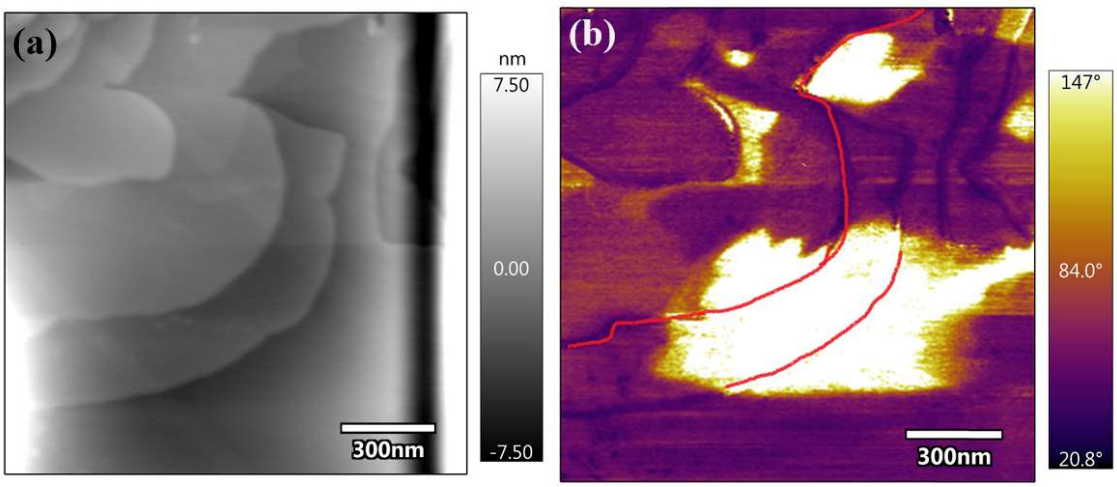

Figure 3.10 (a)The topography and (b) phase images of NBiFeT 1-0 nanosheets. The image size is 1.5 x 1.5 μm^2.

3.4. Characterization of excess Fe-doped NBiFeT nanosheets

3.4.1. Crystalline structure

The XRD patterns of the NBiFeT x-y (x=0,1, y=0, 0.5, 1, 2) nanosheets are presented in Figures 3.11 and 3.12. For all the patterns, the most intense peaks are observed at 2θ of 21.8°, 23.4°, 30.5°, 32.9°, 39.9°, 47.3°, and 48.6°, which closely match the standard reference $Na_{0.5}Bi_{4.5}Ti_4O_{15}$ (JSPDS NO. 74-1318). Additionally, Figure 3.12 exhibits results similar to those of the NBiFeT 2-0 nanosheets (Figure 3.7). As the amount of excess Fe doping (i.e., y) increases to 2, distinct peaks appear at 22.4° and 32°, suggesting that the likelihood of $BiFeO_3$ generation increases with increasing the Fe content. The higher Fe content, the more opportunities for reaction with Bi2O3 and the formation of BFO.

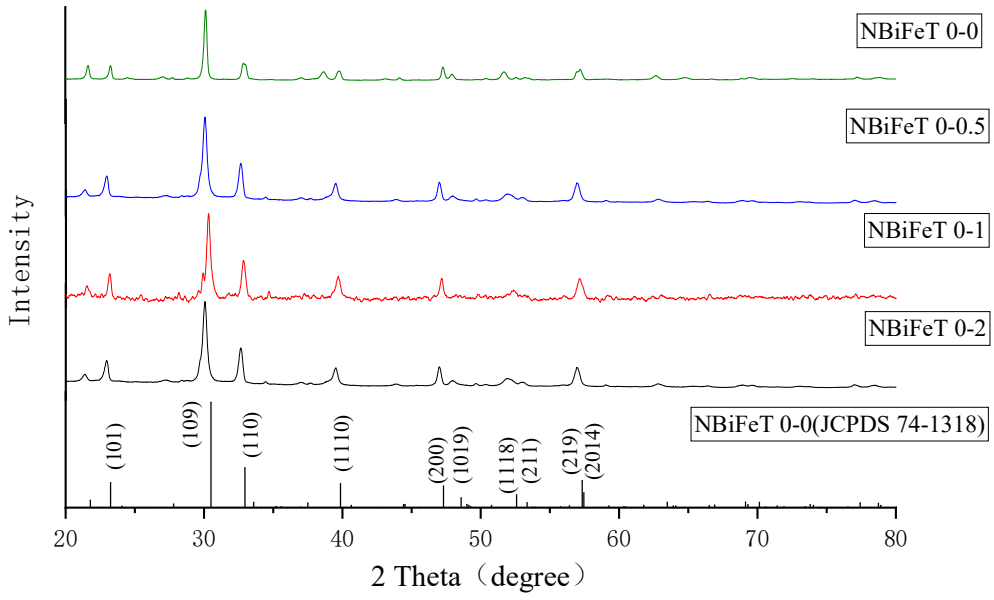

Figure 3.11 The XRD patterns of the NBiFeT 0-y (y=0,0.5,1,2) in the range of 20° - 80°.

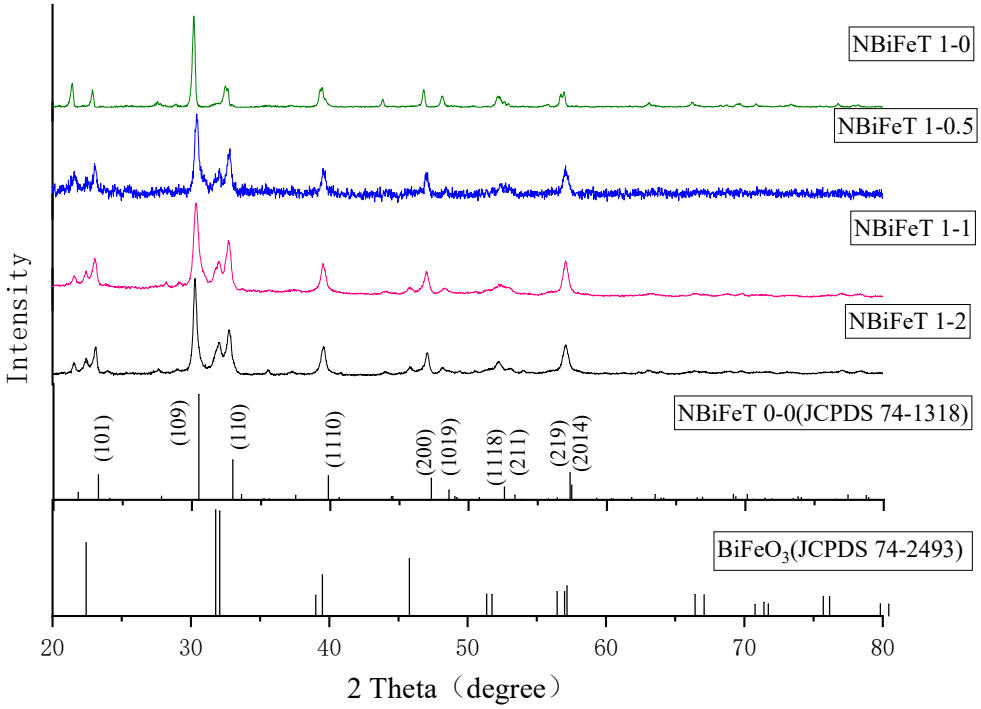

Figure 3.12 The XRD patterns of the NBiFeT 1-y (y=0,0.5,1,2) in the range of 20° - 80°.

3.4.2. Surface Morphology of excess Fe-doped NBiFeT nanosheets

The microstructure of the excess Fe-doped NBiFeT nanosheets has been analyzed, giving the results shown in Figures 3.13 a-d. A comparative assessment of the SEM surface images of samples with different doping contents enables the observation of the impact of excess Fe doping on the microstructure. Two notable effects are observed for the excess doping process: reduction in particle size and emergence of $BiFeO_3$ (as previously affirmed by XRD measurements). As shown in Figure 3.13a, the NBiFeT 1-0 (without excess Fe doping) nanosheets exhibit an average particle size of 3.82 μm. Subsequently, the gradual inclusion of excess Fe induces a substantial reduction in particle size, as evident in Figures 3.13 b-d. As the excess Fe content increase to 0.5 to 1 to 2, the average

particle size decreases successively to 0.58 μm to 0.35 μm to 0.32 μm. The size reduction should be attributed to the accumulation of excess dopants at grain boundaries, impeding the particle growth [81]. Furthermore, BFO begins to form on the surfaces of the NBiFeT 1-0.5, NBiFeT 1-1 and NBiFeT 1-2 nanosheets. This phenomenon agrees with the outcomes of Tseng et al.'s research [49]. Tseng et al. have reported that Fe_2O_3 nanoparticles selectively adsorb onto the surface of $BiFeO_3$ particles, creating raspberry-like core/shell structures. Also, Shuang et al. reported that the $BiFeO_3$ coated on carbon fibers shows smaller BFO particle size, leading to larger surface area [82]. These support the existence of BFO as indicated in the preceding XRD pattern. Consequently, higher levels of excess Fe doping promote an increased likelihood of BFO formation and adsorption onto the NBiFeT x-y nanosheets during the synthesis process.

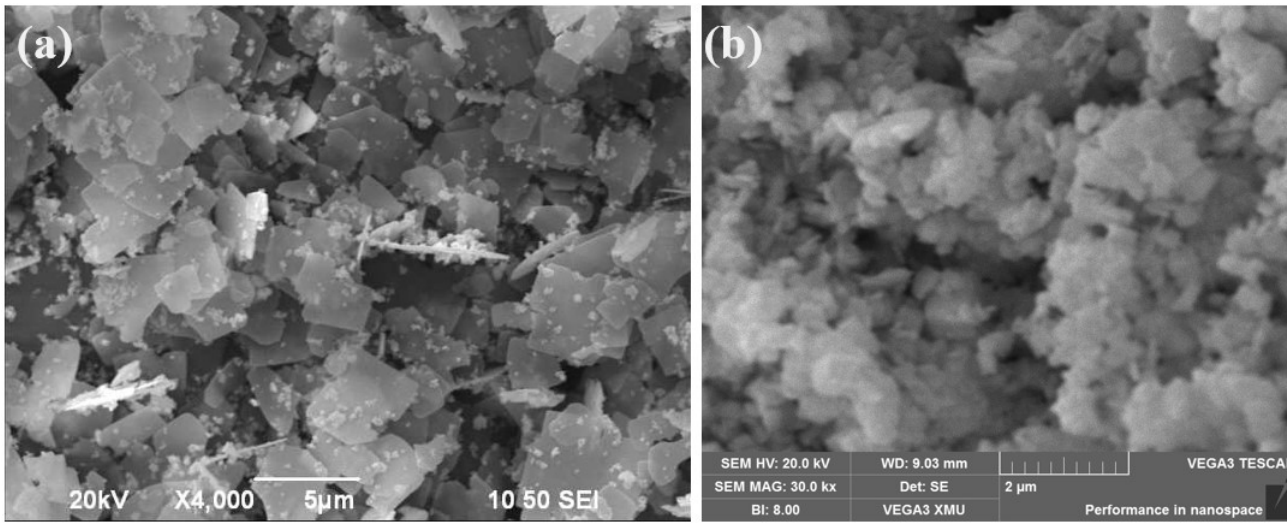

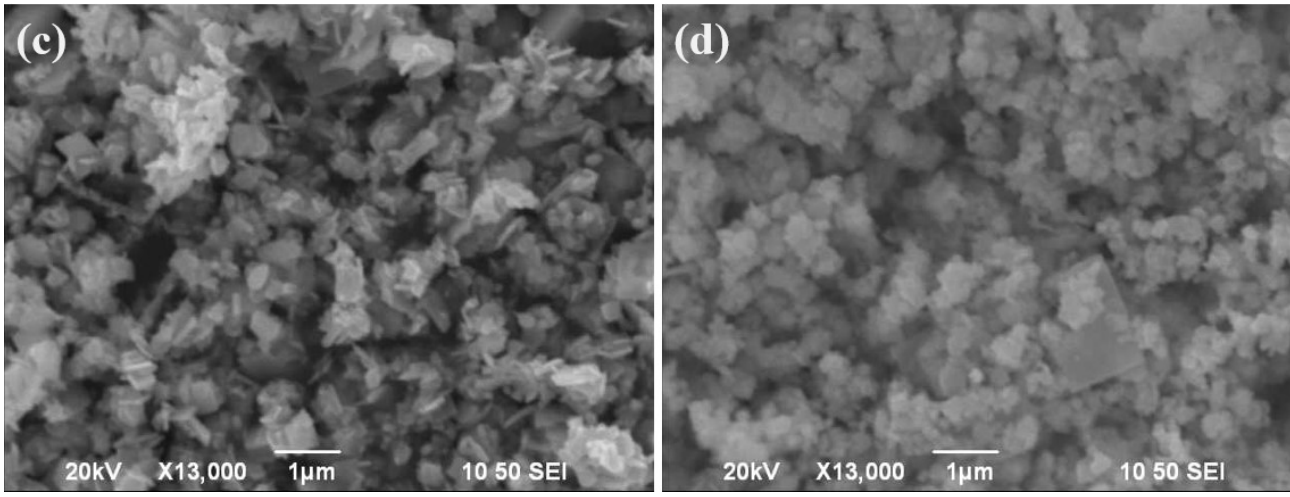

Figure 3.13 SEM of (a) NBiFeT 1-0 (b) NBiFeT 1-0.5 (c) NBiFeT 1-1 (d) NBiFeT 1-2 nanosheets.

3.4.3. PFM measurement

PFM measurements on the NBiFeT 1-2 nanosheets, as examples, have been conducted evaluating the effect of excess Fe doping on the ferroelectric properties of the NBiFeT nanosheets, giving the results shown in Figure 3.14. The topographical features of the NBiFeT 1-2 nanosheets are outlined in Figure 3.14a, with clear annotations indicating the distinctive shapes of these nanosheets. Moreover, the phase image presented in Figure 3.14b also provides evidence of varying polarization directions across the same nanosheet. This significant observation underscores the preservation of ferroelectric properties even after the incorporation of excess Fe into the NBiFeT x-y nanosheets.

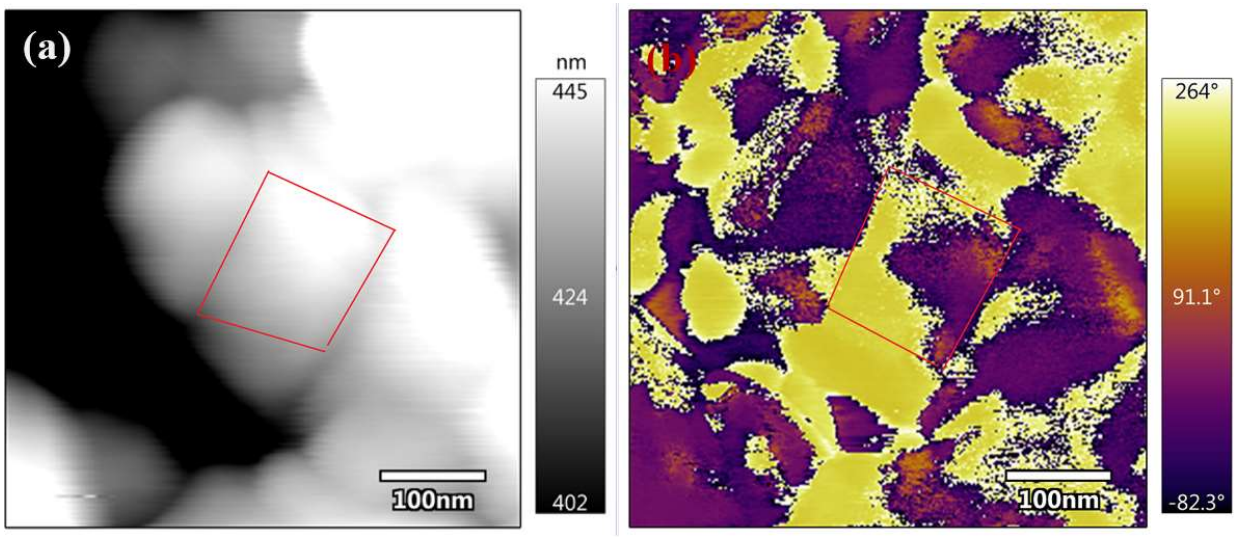

Figure 3.14 (a)The topography and (b) phase images of NBiFeT 1-2 nanosheets. The image size is 0.5 x 0.5 μm^2.

3.5. Optical bandgap estimation

The Tauc's plots of the NBiFeT x-y nanosheets (x=0,1,2 y=0, 0.5,1,2) are shown in Figure 3.15. The band gap of the NBiFeT 0-0 (undoped) nanosheet is 3.28 eV. After the doping Fe or excess Fe, the band gap decreases significantly. This is in agreement with previous research works, in which the decrease in the band gap has been suggested to be arisen from intervalence transitions between two species of Fe^{3+} and Ti^{4+} [83]. The bandgaps of the NBiFeT x-y nanosheets are summarized in Table 3.1.

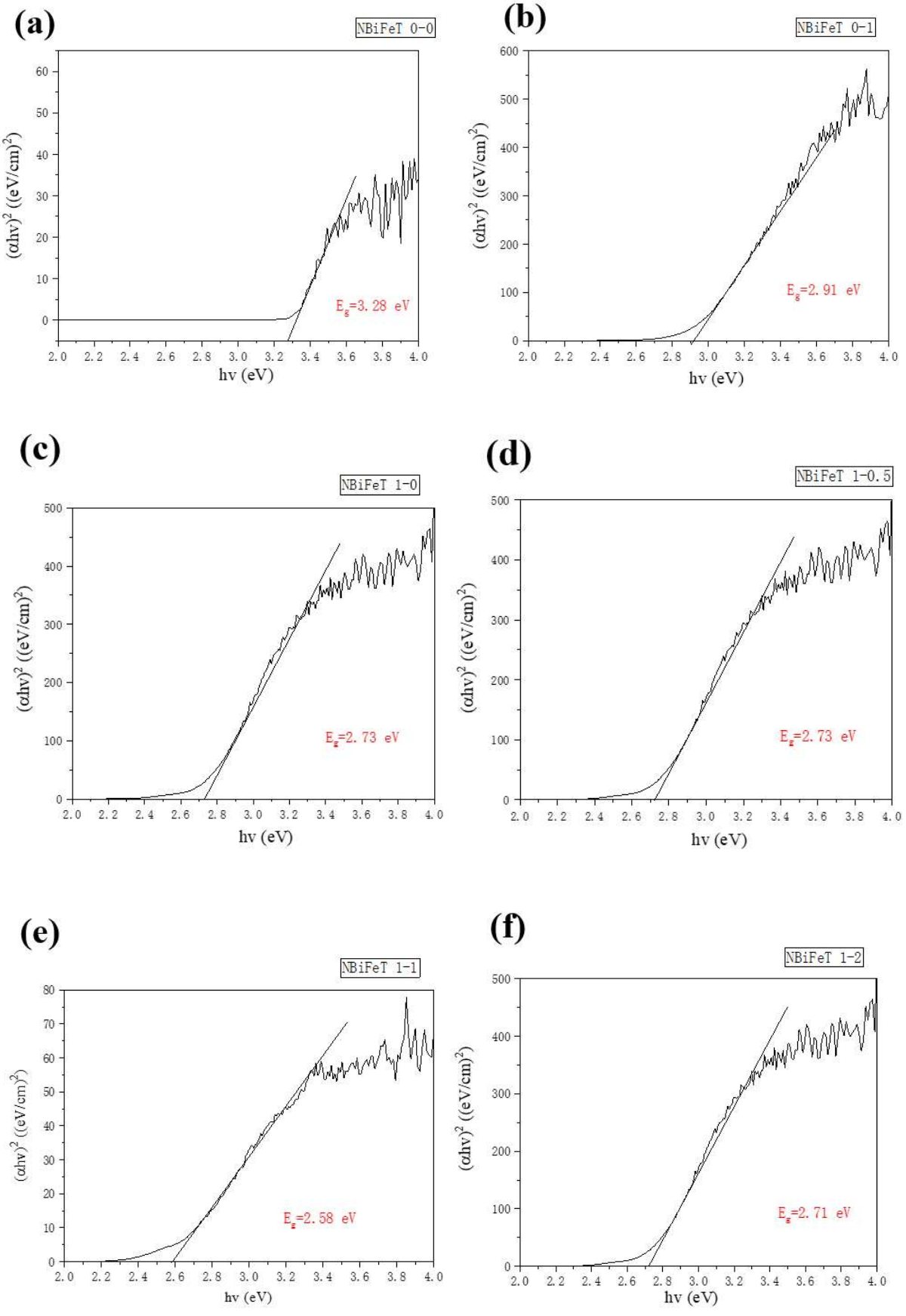
(a)
NBiFeT 0-0
E_g=3.28 eV
(b)
NBiFeT 0-1
E_g=2.91 eV
(c)
NBiFeT 1-0
E_g=2.73 eV
(d)
NBiFeT 1-0.5
E_g=2.73 eV
(e)
NBiFeT 1-1
E_g=2.58 eV
(f)
NBiFeT 1-2
E_g=2.71 eV
$(\alpha h\nu)^2$ ((eV/cm)^2)
hv (eV)

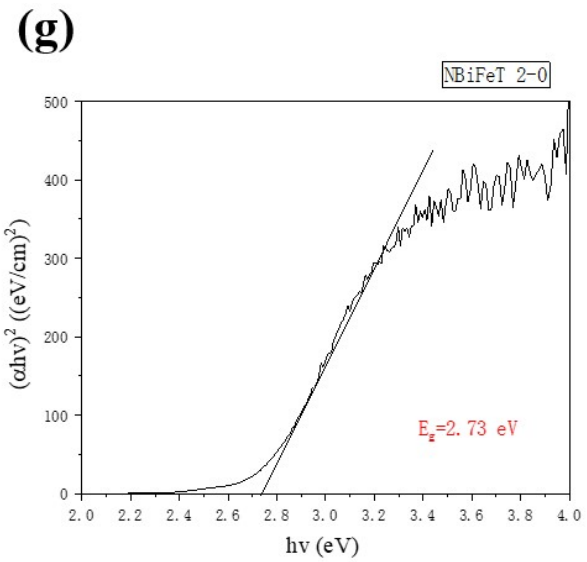

Figure 3.15 Tauc's Plot of (a)NBiFeT 0-0, (b)NBiFeT 0-1, (c)NBiFeT 1-0, (d)NBiFeT 1-0.5, (e)NBiFeT 1-1, (f)NBiFeT 1-2, (g)NBiFeT 2-0 nanosheets.

Table 3.1 Estimated optical band gap of NBiFeT x-y (x=0,1,2 y=0,0.5,1,2) nanosheets.

Sample	E_g (eV)
NBiFeT 0-0	3.28
NBiFeT 0-1	2.91
NBiFeT 1-0	2.73
NBiFeT 1-0.5	2.73
NBiFeT 1-1	2.58
NBiFeT 1-2	2.71
NBiFeT 2-0	2.73

3.6. BET analysis

Table 3.2 presents the surface areas the NBiFeT x-y nanosheets determined by the BET analysis. A notable trend is observed: an increase in the amount of Fe doping leads to a larger surface area obtained. As shown in Table 3.2, the surface area of NBiFeT 0-0 is measured as 1.09 m^2/g. After the Fe doping content (i.e., x) increases to 1 and 2, the surface areas increase to 2.41 m^2/g and 12.27 m^2/g, respectively. However, such an increasing trend has not been observed for the nanosheets doped with excess Fe (i.e., y > 0). As discussed in the SEM analysis, the nanosheets doped with excess Fe exhibit a smaller particle size. For example, the particle size of NBiFeT 1-1 is 0.35 μm, where that of NBiFeT 1-0 is 3.82 μm. This phenomenon may stem from the diminished affinity of nitrogen towards NBiFeT nanosheets after the addition of excess Fe [84], [85].

Table 3.2 BET data of NBiFeT x-y (x=0,1,2 y=0,0.5,1,2) nanosheets.

Sample	BET surface area (m^2/g)
NBiFeT 0-0	1.09
NBiFeT 0-1	20.46
NBiFeT 1-0	2.41
NBiFeT 1-0.5	7.40
NBiFeT 1-1	4.03
NBiFeT 1-2	21.18
NBiFeT 2-0	12.27

3.7. Conclusion

The NBiFeT x-y nanosheets have been successfully fabricated by the molten salt synthesis technique using different amount of salt mixture. As indicated by the SEM analysis, the optimal content of added salt mixture for of the NBiFeT 0-0 nanosheets is 1:60:60. In comparing with the standard $Na_{0.5}Bi_{4.5}Ti_4O_{15}$ crystal structure, the crystalline structure of all the nanosheets has been confirmed by the XRD analysis. The investigations also reveal the ferroelectric nature of the NBiFeT 0-0 (as an example) at room temperature. As evidenced by the TEM analysis, the exposed plane of the NBiFeT 0-0 nanosheets is primarily {001} facet. The ferroelectric nature has also been corroborated by the slightly open P-E loop measured at 100°C.

After the doping of Fe (exact), the lattice spacings of the NBiFeT nanosheets increase, making the XRD pattern shifted towards the lower 2θ values. The particle size of the nanosheets also decrease with increasing the Fe doping.

Furthermore, the doping with excess Fe also leads to a decrease in the particle size of the NBiFeT nanosheets. This should be attributed to the accumulation of dopants at grain boundaries, hindering particle growth. Additionally, a higher Fe content provides more opportunities for the reactions with Bi_2O_3, ultimately leading to the formation of $BiFeO_3$ (BFO).

The optical band gaps of the NBiFeT x-y nanosheets are estimated through diffuse reflectance spectroscopy. After the doping of Fe or excess Fe, the band gap of the NBiFeT 0-0 nanosheets decreases significantly. The ferroelectric properties of the Fe-doped nanosheets have confirmed by the PFM, P-E loop and temperature-dependent dielectric properties measurements.

Chapter 4 Photocatalytic performance of NBiFeT x-y nanosheets

4.1. Introduction

As discussed in Chapter 3, both the undoped and Fe-doped NBiFeT x-y nanosheets exhibit ferroelectric properties characterized by a spontaneous polarization. It has been elucidated that the inherent electric field resulting from the spontaneous polarization can effectively steer photogenerated electrons and holes to opposite sides, thereby facilitating high-efficiency charge separation [16].

This chapter delves into the photocatalytic performances of the NBiFeT 0-0 nanosheets. The nanosheets synthesized using the molten salt synthesis technique with a mole ratio of 1:60:60 (nominal NBiFeT x-y nanosheets to salt mixture) exhibited a reduction in the particle size, which suggests a potentially enhanced photocatalytic degradation capability for the NBiFeT 0-0 nanosheets. The plausible photocatalytic mechanism of the NBiFeT nanosheets explored based on the correlation of the photocatalytic degradation performances with the crystal structure and morphology is demonstrated. Additionally, the photocatalytic performance of the Fe-doped and excess Fe-doped NBiFeT x-y nanosheets are also presented, with the aim of elucidating the effect of the Fe doping on the photocatalytic degradation.

Also, the investigation of the predominant active species involved in the photocatalytic RhB removal process based on the active species trapping experiments is presented.

It is suggested anticipated that $\bullet O_2^-$ radicals constitute the primary active species responsible for the photocatalytic degradation process. Lastly, the influence of pH values on the degradation process is discussed.

4.2. Photocatalytic performance of NBiFeT 0-0 nanosheets

The photocatalytic performance of NBiFeT 0-0 nanosheets in degrading RhB in aqueous solution under simulated sunlight irradiation (with a light intensity of 300 mW/cm^2) using solar simulator. Figure 4.1a depicts the degradation curves of RhB (C/C_0) for the NBiFeT 0-0 photocatalysts as a function of experimental time. In this context, C_0 denotes the initial concentration of RhB (i.e., experimental time = 0), and C represents the corresponding concentration after a specific reaction duration. As discussed in Chapter 2, the suspension comprising the pollutant RhB solution and photocatalysts will be continuously stirred in the dark for 30 minutes to achieve an adsorption-desorption equilibrium before the photo-degradation evaluation. In this study, this 30-minute stirring period is included in the experimental time, i.e., the first 30 minutes in Figure 4.1a (and the other degradation curves) refers to this 30-minute stirring period. It should be noted that the suspension will be continuously stirred during the whole experimental process. For comparison purposes, the degradation curve for the suspension without the NBiFeT 0-0 photocatalysts has also been determined, giving the results shown in Figure 4.1a. It can be seen that the observed C/C_0 remains unchanged throughout the whole process, i.e., 30-minute stirring in the dark and 180-minute stirring under simulated sunlight irradiation. This highlights the stability of RhB as well as the limited effect of simulated sunlight irradiation on RhB degradation. On the other hand, in a high photocatalytic efficiency is obtained after introduction of the NBiFeT 0-0 photocatalysts. As depicted in Figure 4.1a,

a remarkable 98% degradation of RhB is achieved after 180 minutes of irradiation, underscoring the prevailing role of photocatalytic degradation. It is interesting to note that the observed C/C_0 starts to decrease before the irradiation, i.e., within the first 30-minute stirring in the dark, and the decrease becomes saturated at 7% under the irradiation. This phenomenon will be discussed further in the following section. The rates of RhB photodegradation for the photocatalysts can be determined using the kinetics equation $\ln(C_0/C) = kt$ [86], where t denotes the time of light irradiation and k represents the rate constant. As shown in Figure4.1b, the observed C_0/C during the irradiation period, i.e., after 30 minutes, are used to determine the rate constant k value for the NBiFeT 0-0 nanosheets, giving an average value of 0.0192 min^{-1}.

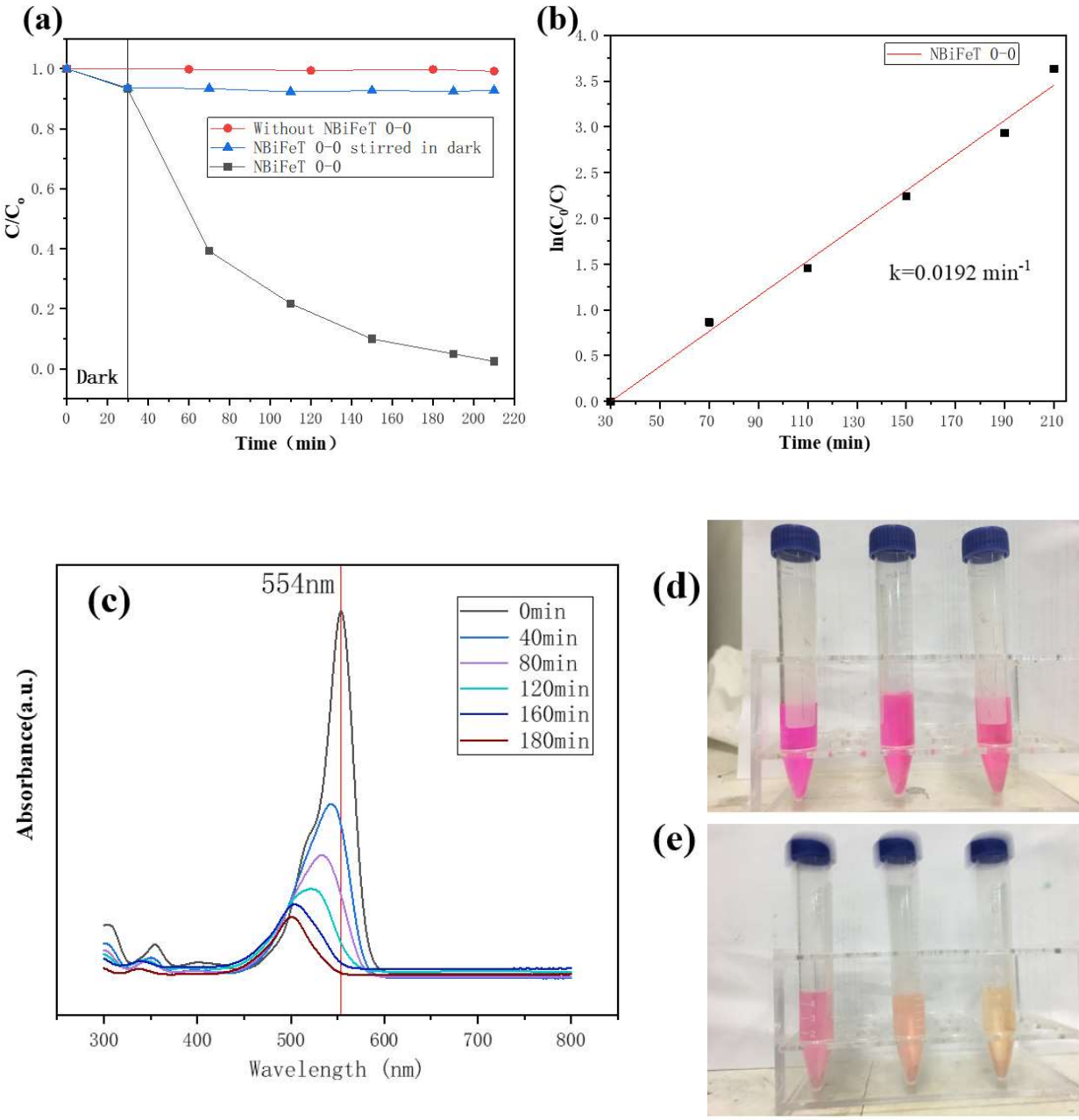

Figure 4.1 (a) C/C_0 curve and (b) rate constant of the RhB degradation with NBiFeT 0-0 nanosheet. (c) UV–vis absorption spectra of RhB. (d) colour observed from 0 to 80 minutes and (e) 120 to 180 minutes.

Figure 4.1c depicts the UV–vis absorption spectra of the RhB solutions after different irradiation durations and removal of the NBiFeT 0-0 photocatalysts. As previously mentioned, the maximum absorption peak of RhB occurs at 554 nm. The gradual reduction in

absorbance with increasing irradiation time indicates the progressive decrease in RhB concentration of the aqueous solution. Ultimately, a remarkable 98% degradation of RhB is achieved after 180 minutes of irradiation. It is noteworthy that the maximum absorption peak of the degraded solution experiences a hypsochromic shift over the course of irradiation. This shift should be attributed to the de-ethylation of fully N,N,N0,N0-tetraethylated rhodamine (i.e., RhB) into de-ethylated intermediates [72], and serves as an indicator of photocatalytic degradation. It has been reported that the maximum absorption peak locates at 554 nm for RhB, and shifts to 539 nm for N,N,N0-triethylated rhodamine, 522 nm for N,N0-diethylated rhodamine, 510 nm for N-ethylated rhodamine, and 498 nm for Rhodamine [72]. The visual representation of the color change in the RhB solution is presented in Figures 4.1d-e.

4.2.1 Photocatalytic mechanism

Drawing upon the degradation efficiency, morphology, and crystal structure of the NBiFeT 0-0 nanosheets, we can delineate the factors underlying the augmented photocatalytic performance and subsequently propose a mechanism for the photocatalysis of NBiFeT 0-0 nanosheets. The high photocatalytic efficiency is primarily interconnected with factors such as light absorption efficiency (η_{abs}), efficiency in charge excitation and separation (η_{cs}), charge migration and transfer efficiency (η_{cmt}), and the efficiency of charge utilization in photocatalytic reactions (ηcu) [87]. The ferroelectric properties of single-crystal $Na_{0.5}Bi_{4.5}Ti_4O_{15}$ are markedly anisotropic, stemming from its layered perovskite configuration. This configuration comprises interleaved fluorite-like $(Bi_2O_2)^{2+}$ layers and TiO_6 octahedra (perovskite slab) oriented along the c-axis, as depicted in Figure 4.2a [88]. The NBiFeT 0-0 nanosheets manifest a saturated polarization (Ps) of 1.4 $\mu C/cm^2$ along the c-axis (Fig. 3.5), as previously tested. It has been established that the

polarization of ferroelectric materials can enhance photocatalytic activities [89]. The inherent orientation of the internal polarization electric field is perpendicular to the surface of the nanosheets, thereby facilitating the accumulation of negative and positive charges in opposite directions. Upon sunlight exposure, the NBiFeT 0-0 nanosheet, featuring {001} facet, generates photoinduced electron–hole pairs. These electron–hole pairs are subsequently driven apart toward different directions by the internal electric field, thereby achieving effective spatial separation of the photoinduced carriers (Fig. 4.2b) [90]. Consequently, the efficiency of segregating photoinduced charge pairs along the [001] direction of NBiFeT 0-0 nanosheets is enhanced (Figure 4.2c). In addition, a screening effect prompts the emergence of a depolarization field within the bulk crystals, which further mitigates the recombination of charge carriers [27], [39].

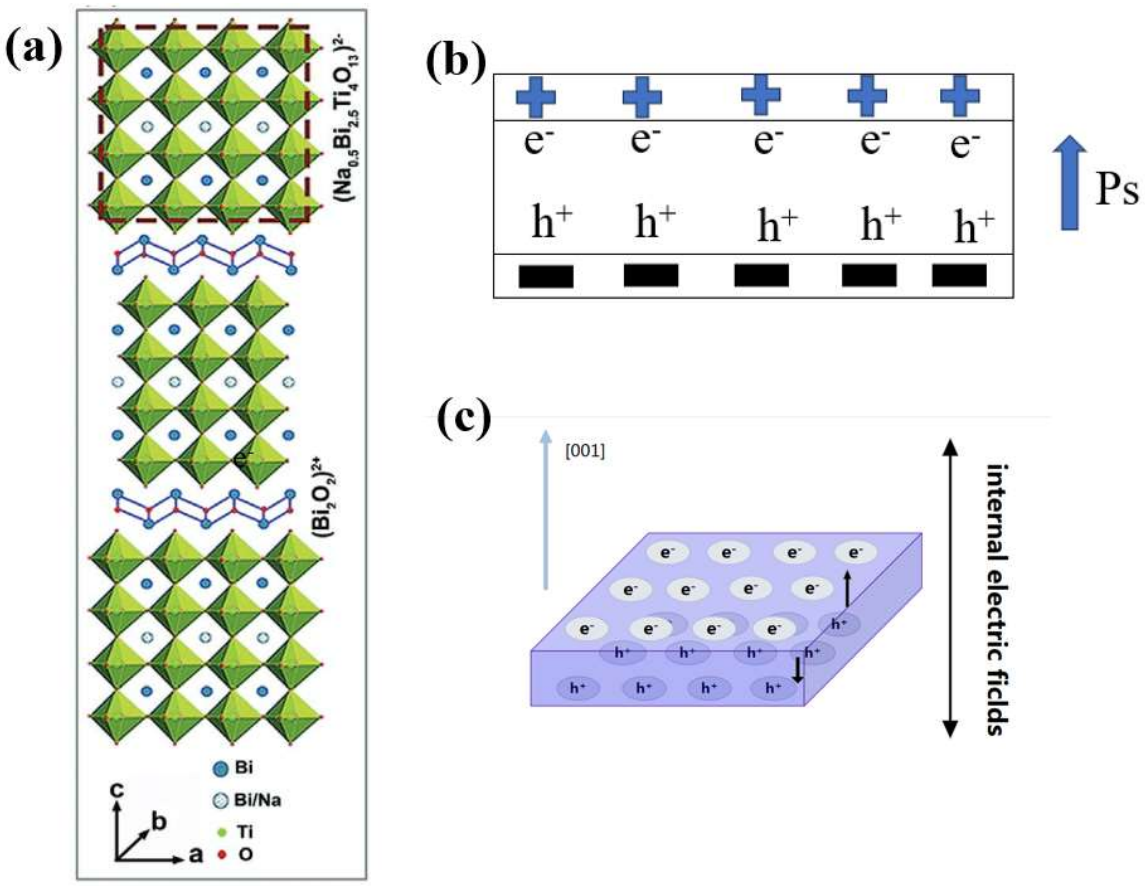

Figure 4.2 (a) The crystal structure of Na0.5Bi4.5Ti4O15 viewed along c-axis. [88]. (b) Suggested the mechanism of the photogenerated carriers which separated by P_s. (c) Schematic diagram of NBiFeT 0-0 nanosheets with the internal electric field.

4.3. Photocatalytic performance of Fe-doped NBiFeT nanosheets

The photocatalytic efficiencies of the Fe-doped NBiFeT nanosheets, i.e., NBiFeT 1-0 and NBiFeT 2-0, in degrading Rhodamine B (RhB) have been evaluated. Figure 4.3a depicts the degradation curves of RhB (C/C_0) for NBiFeT 0-0, NBiFeT 1-0, and NBiFeT 2-0. Similar to NBiFeT 0-0 mentioned before, the observed C/C_0 for NBiFeT 1-0 and NBiFeT 2-0 starts to decrease in the absence of light and reaches a decrease of 40% and

18%, respectively, after the 30-minute stirring in the dark. For NBiFeT 1-0, the degradation of RhB reach about 92%, which is slightly lower than that for NBiFeT 0-0 (98%). Among the three samples, NBiFeT 2-0 exhibits a minimum degradation of ~67%. Figure 4.3b compare the rate constant (k) of NBiFeT 0-0, NBiFeT 1-0, and NBiFeT 2-0. The calculated k values for NBiFeT 0-0, NBiFeT 1-0 and NBiFeT 2-0 are 0.0192, 0.0110 and 0.0052 min^{-1}, respectively, underscoring that the photocatalytic activity of NBiFeT 0-0 is the highest, being 1.75 and 3.66 times greater than that of NBiFeT 1-0 and NBiFeT 2-0, respectively. Furthermore, Figures 4.3c-d illustrate the UV-vis absorption spectra of the RhB solutions after the degradation with NBiFeT 1-0 and NBiFeT 2-0 nanosheets for different irradiation durations. Both the spectra exhibit a hypsochromic shift of the absorption peak towards lower wavelengths, attributed to the de-ethylation of RhB, which serves as an indicator of photocatalytic degradation.

As elucidated in Chapter 3, the BET analysis results (refer to Table 3.2) revealed an increase in surface area of the NBiFeT nanosheets after the Fe doping. The surface areas for NBiFeT 0-0, NBiFeT 1-0, and NBiFeT 2-0 are measured as 1.09, 2.41, and 12.27 m^2/g, respectively. As also revealed by the SEM images (Fig. 3.8), the average particle sizes are determined as 1.49 μm for NBiFeT 0-0, 3.82 μm for NBiFeT 1-0, and 2.13 μm for NBiFeT 2-0. It is evident that NBiFeT 2-0 possesses the largest surface area and the smallest particle size, yet exhibits the lowest photocatalytic degradation efficiency. This observation suggests that enhanced surface area cannot improve photocatalytic performance in this study. Furthermore, Zhu et al. have reported a decrease in photocatalytic activity with an increase in Fe doping under similar experimental conditions. [91]. This phenomenon has been attributed to the higher concentration of Fe^{3+} ions replacing Ti^{4+} in

the lattice, which serves as recombination sites for photogenerated charge carriers. Consequently, the higher Fe concentration can impede the photocatalytic efficiency of the nanosheets. Hence, it is deduced that the lower degradation efficiency of NBiFeT 2-0 as compared to NBiFeT 0-0 and NBiFeT 1-0 should be due to this effect.

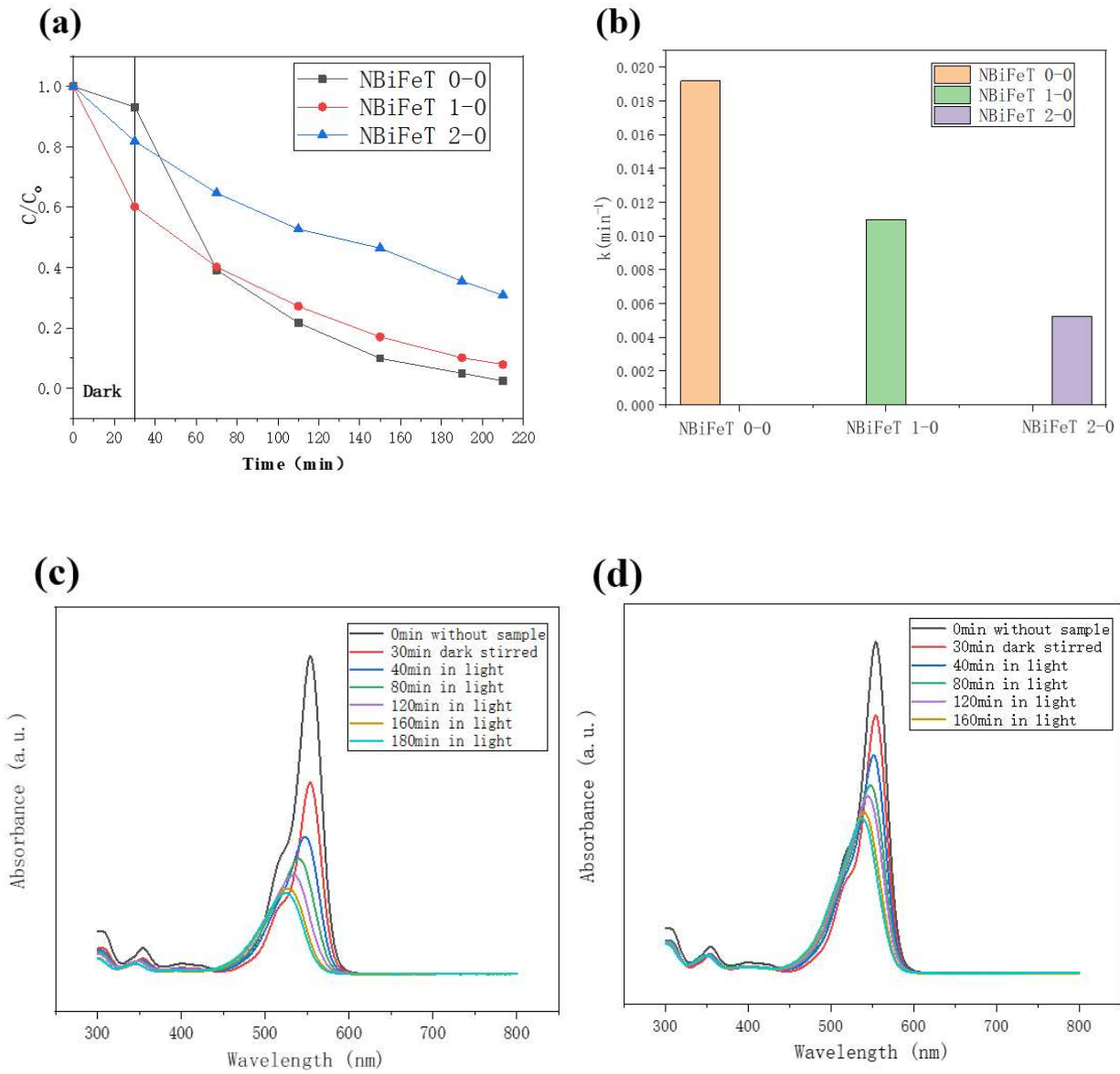

Figure 4.3 (a) C/C_0 curve of RhB degradation with NBiFeT 0-0, 1-0 and 2-0 nanosheets. (b) Comparison of the rate constant for photodegradation of RhB using NBiFeT 0-0, 1-0,

and 2-0 nanosheets under solar irradiation. The UV–vis absorption spectra of RhB with nanosheets (c) NBiFeT 1-0 and (d)NBiFeT 2-0.

4.4. Photocatalytic performance of excess Fe-doped NBiFeT nanosheets

According to the results discussed before, the NBiFeT 0-0 nanosheets show the best performance in photocatalytic degradation. Therefore, they are selected as the base material for studying the effect of excess Fe doping on the photocatalytic degradation. In this study, the NBiFeT 0-0, NBiFeT 0-0.5 and NBiFeT 0-2 nanosheets have been used as the photocatalysts to degrade RhB, giving the results shown in Figure 4.5a. It can be seen that the observed C/C_0 for all the nanosheets starts to decrease during the first 30-minute stirring in the dark. More importantly, the dark adsorption i.e., the decrease of C/C_0 in the dark, enhances significantly from 7% to 71% and 72% respectively, after the excess Fe doping. As also shown in Figure 4.5a, the degradation of RhB continues and reaches 98%, 96% and 90% for NBiFeT 0-0, NBiFeT 0-0.5 and NBiFeT 0-2, respectively, after an irradiation of 180 minutes. The rate constants (k) of the nanosheets are compared in Figure 4.5b. The calculated k values, based on the observed C/C_0 during the 180 minutes irradiation, for NBiFeT 0-0, NBiFeT 0-0.5, and NBiFeT 0-2 are 0.0192, 0.0106 and 0.0056 respectively. It is clear that the photocatalytic performance was worsen after the excess Fe doping. Although 96% and 90% of RhB have been "degraded" by NBiFeT 0-0.5 and NBiFeT 0-2, the most of them were adsorbed by adsorption, not photocatalysis. A similar tendency in photocatalytic degradation has been observed for the nanosheets doped with (exact) Fe (Fig. 4.3a). Therefore, it is confirmed that a high concentration of Fe could provide more recombination sites of the photogenerated charge carries that result

in restricting the photocatalytic activity of materials [91]. Figures 4.5 c-d show the UV–vis absorption spectra of the RhB solutions after the degradation with NBiFeT 0-0.5 and NBiFeT 0-2, respectively, for different irradiation durations. A hypsochromic shift of the absorption peak towards lower wavelengths attributed to the de-ethylation of RhB is observed for both the nanosheets during the 180-minute irradiation process. It can also be seen that, for both the nanosheets, the maximum absorption peak remains at 554 nm, suggesting that adsorption rather than degradation of RhB takes place during the stirring in the dark.

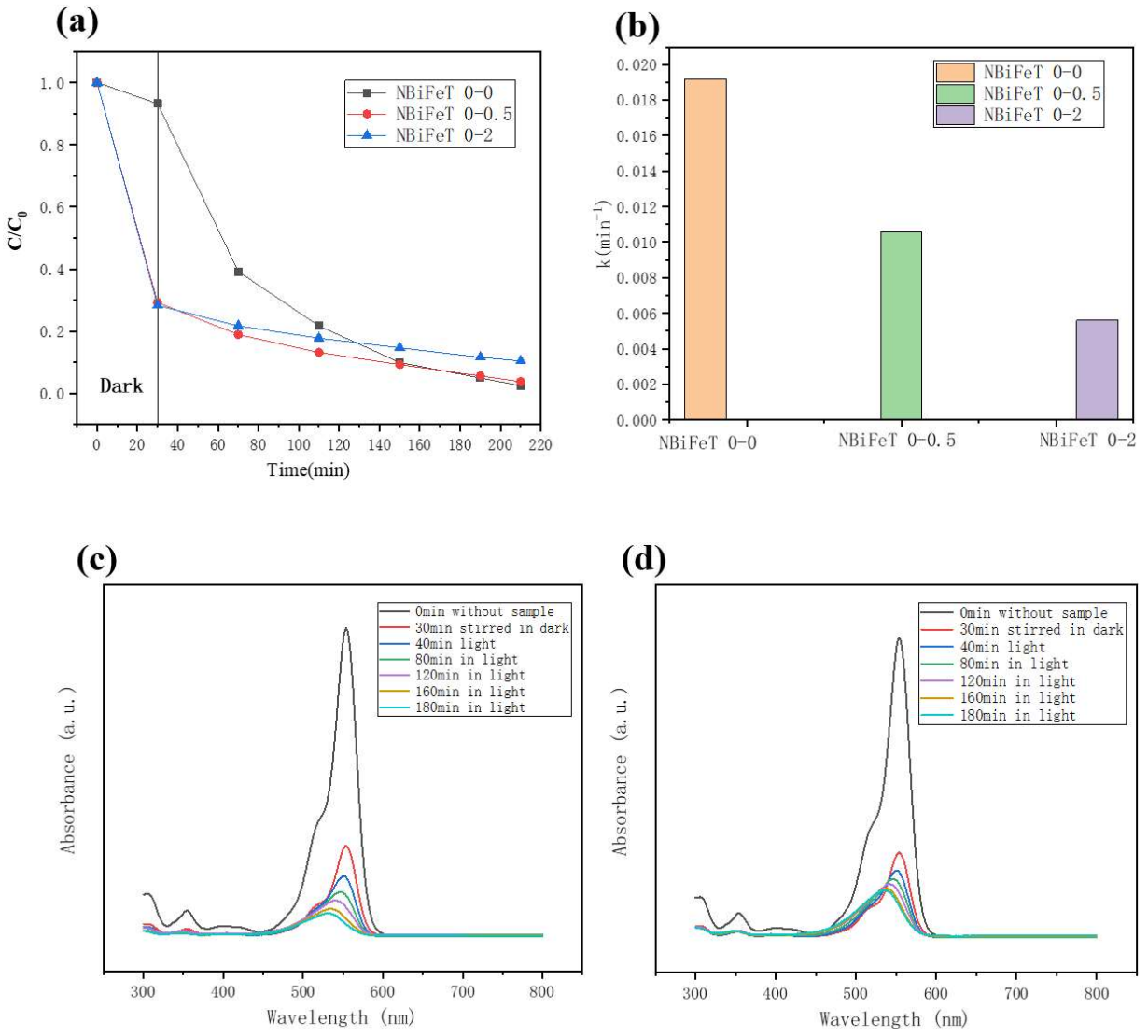

Figure 4.4 (a) C/C_0 curve of RhB degradation with NBiFeT 0-0, NBiFeT 0-0.5 and NBiFeT 0-2 nanosheets. (b) Comparison of the rate constant for photodegradation of RhB using NBiFeT 0-0, NBiFeT 0-0.5, and NBiFeT 0-2 nanosheets under irradiation. The UV–vis absorption spectra of RhB with nanosheets (c) NBiFeT 0-0.5 and (d)NBiFeT 0-2.

4.5. Active species trapping experiments

In order to elucidate the primary active specie involved in the photocatalytic processes governing the removal of RhB, trapping experiments have been conducted. NBiFeT 0-0 is selected for this study because of its highest photocatalytic performance. Ethylenediaminetetraacetic acid (EDTA), p-benzoquinone (BQ), and isopropyl alcohol (IPA) are selected as scavengers for capturing photogenerated holes (h^+), superoxide radicals ($\bullet O_2^-$), and hydroxyl radicals (•OH) species [92],[93], respectively. The efficiency of RhB degradation has been scrutinized within the reaction system for the NBiFeT 0-0 photocatalyst, both in the presence and absence of these scavengers, giving the results depicted in Figure 4.5. In the presence of BQ, the RhB degradation efficiency is remarkably reduced, leaving about 67% of RhB after light irradiation for 180 minutes. The photodegradation of the RhB is obviously inhibited, when compared to high degradation of RhB (98%) in the absence of scavengers. On the other hand, almost no effects on the photocatalytic activity are observed for the usage of IPA and EDTA. This indicates that •OH and h^+ are not the main active species in the photocatalytic process. This observation signifies the predominant involvement of superoxide radicals in the photocatalytic degradation of RhB dye.

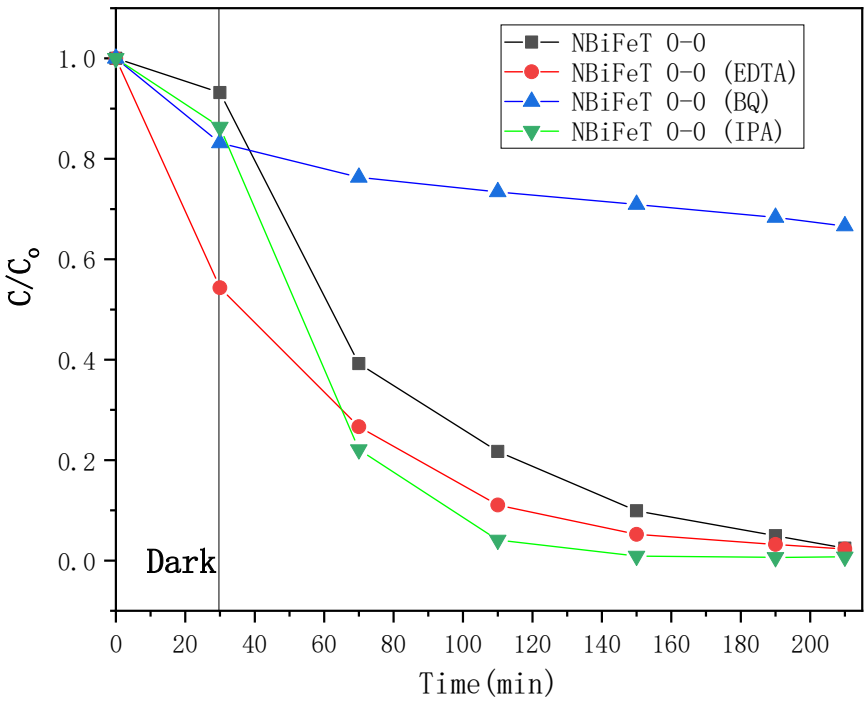

Figure 4.5 RhB removal efficiency of NBiFeT 0-0 nanosheets obtained from trapping experiments with different scavengers.

4.6. The effect of pH value in photocatalytic performance

It has been shown that the pH value of the solution exerts a substantial influence on the degradation efficiency of the photocatalytic reaction [94]. When the pH value of the solution approaches the catalyst's isoelectric point, the catalyst particles are prone to agglomeration, driven by van der Waals forces [95]. This aggregation results in the formation of larger particles, subsequently leading to reductions in specific surface area and photochemical activity. Conversely, when the pH value of the solution significantly deviates from the isoelectric point, the repulsive forces between particles facilitate better dispersion of the catalyst in the solution, thereby enhancing the removal rate. Furthermore, the pH value of the solution is instrumental in determining the nature and quantity of

charges present on the catalyst's surface, which in turn influences the adsorption behaviour of organic pollutants. Therefore, an exploration into the effect of pH value on the degradation of RhB using the NBiFeT nanosheets has been undertaken in this study.

In general, the pH value of RhB solution is 4.7. In this study, it has been adjusted by using different amounts of NaOH solution to 7.2 and 11. As shown in Figure 4.6, although the NBiFeT 0-0 nanosheets can almost completely degrade the RhB after 3 hours of irradiation at the three pH values, the degradation rate is different in the first 2 hours. For the normal case (pH = 4.7), the degradation of RhB reaches 80% after 2 hours of light irradiation. As the pH value increases to 7.2, the degradation is almost complete (99%) in the first 2 hours of irradiation. Nonetheless, it is noteworthy that the degradation efficiency experiences a notable decline in alkaline conditions. At pH =11, the degradation of RhB only reaches 66% after 2 hours of light irradiation. Interestingly, almost no dark adsorption (the decrease of C/C_0 during the first 30-minute stirring in the dark) is observed in the alkaline environment. This phenomenon should be attributed to a large number of hydroxyl groups (OH^-) in alkaline environment, which makes the adsorption difficult to occur. The surfaces of nanosheets are covered with a high concentration of OH^-, which results in a negatively charged surface. In an alkaline environment, the RhB dye becomes deprotonated, causing the repulsion to nanosheets with the negatively charged surface [96].

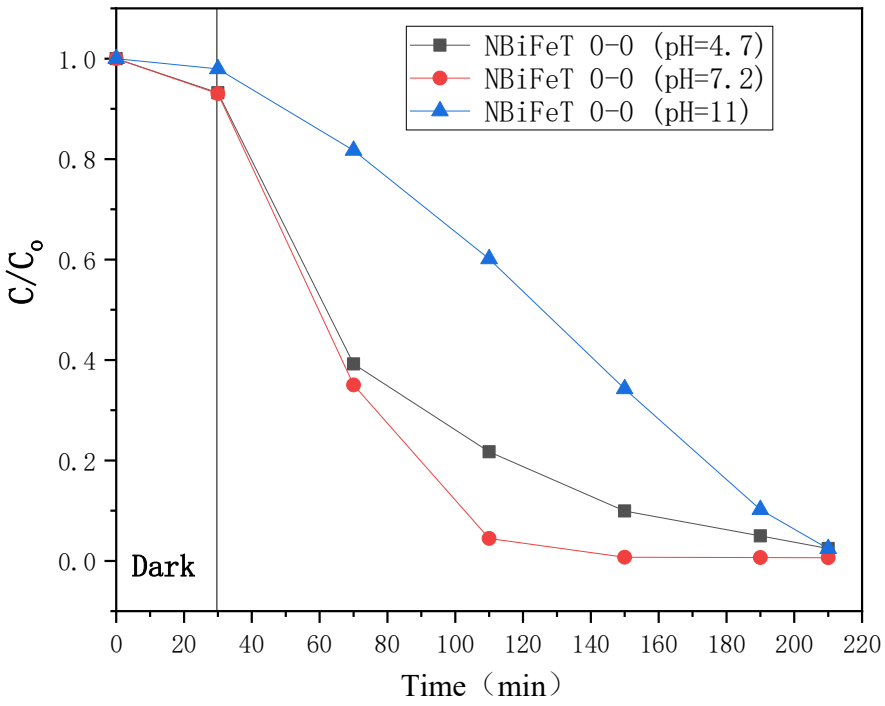

Figure 4.6 RhB removal efficiency of NBiFeT 0-0 nanosheets obtained under different pH value.

4.7. Conclusion

The photocatalytic performances of undoped and Fe-doped NBiFeT nanosheets have been investigated.

For the undoped nanosheets, i.e., NBiFeT 0-0, the degradation of RhB reaches 98% after 180 minutes of irradiation. The maximum absorption peak of the RhB solution experiences a hypsochromic shift towards lower wavelengths. It is due to the de-ethylation process of RhB which can be considered as the indicator of the photocatalytic degradation process. Base on the results of crystal structure, morphology and degradation efficiency, the photocatalytic mechanism of the NBiFeT 0-0 nanosheets has been suggested. The

good photocatalytic performance is attributed to the internal polarization electric field of the NBiFeT 0-0 nanosheets feature with {001} facets. Under sunlight irradiation, the nanosheet initiates the generation of photoinduced electron–hole pairs. Subsequently, these electron–hole pairs undergo separation with the aid of the internal electric field, leading to efficient spatial segregation of the photoinduced carriers.

The photocatalytic performances of nanosheets doped with (exact) Fe, i.e., NBiFeT x-0, have been investigated and compared with that of undoped nanosheets. In general, the photocatalytic performance becomes worse after the doping of Fe. The degradation of RhB decreases from 98% to 92% and 67%, respectively, for NBiFeT 1-0 and NBiFeT 2-0, while the calculated rate constant (k) decreases from 0.019 to 0.0110, and 0.0052 min^{-1}, respectively. The decrease should be attributed to the more recombination sites for photogenerated charge carriers generated by the high Fe content.

The photocatalytic performances of nanosheets doped with Fe, i.e., NBiFeT 0-y, have also been investigated. The degradation of RhB reaches 96%, and 90% for NBiFeT 0-0.5 and NBiFeT 0-2, respectively, while the calculated rate constants are 0.0106 and 0.0056, respectively. Although the excess Fe doping does not affect photocatalytic performance too much, it enhances significantly the absorption of RhB during the first 30 minutes of stirring in the dark. Most of the RhB have become adsorbed by adsorption, not photocatalysis. In general, the excess Fe doping exhibits similar effects on the photocatalytic performances to the exact doping.

The primary active specie involved in the photocatalytic degradation has been investigated by the trapping experiments. In the presence of BQ, the RhB degradation efficiency is remarkably reduced, leaving about 67% of RhB after 180 minutes of light irra-

diation. Meanwhile, the uses of IPA and EDTA have almost no effect on the photocatalytic activity. The result indicates that $\bullet O_2^-$ is the main active species for RhB photocatalytic degradation.

Finally, the effect of pH value in photocatalytic performance has been investigated. The pH value of the RhB solution has been adjusted from 4.7 to 7.2 and 11 by using different amounts of NaOH solution. Although the NBiFeT 0-0 nanosheets can almost completely degrade the RhB after 3 hours light irradiation at the three pH values, their degradation rates in the first 2 hours are different. As the pH value increases from 4.7 to 7.2, the degradation of RhB reaches 80% in the first 2 hours of irradiation. Nonetheless, it is noteworthy that the degradation efficiency experiences a notable decline in alkaline conditions. At pH =11, the degradation of RhB only reaches 66% after 2 hours of light irradiation. Almost no adsorption is observed in the alkaline environment during the first 30-minute stirring in the dark. This should be attributed to the repulsion force between the negatively charged surfaces of nanosheets and the deprotonated RhB dye.

Chapter 5 Adsorption capability of NBiFeT x-y nanosheets

5.1. Introduction

As discussed in Chapter 4, the Fe-doped NBiFeT nanosheets show excellent capability of RhB adsorption in the dark, without sunlight irradiation.

In this chapter, the adsorption capability of Fe-doped and excess Fe-doped NBiFeT x-y nanosheets are presented, with the aim of studying the effects of the Fe doping on the adsorption. The mechanism of the adsorption capability enhanced after Fe doping is suggested based on the experiment results. The influence of the pH values on adsorption is also discussed. Finally, modification of magnetic properties of the nanosheets has been explored for facilitating the separation and recovery of the adsorbent from solution.

5.2. Adsorption capability of Fe-doped NBiFeT nanosheets

The adsorption capability of the Fe-doped NBiFeT nanosheets, i.e., NBiFeT 0-0, NBiFeT 1-0 and NBiFeT 2-0, in adsorption of RhB have been evaluated. Figure 5.1 presents the adsorption curves of RhB ($\Delta C/C_0$) for NBiFeT 0-0, NBiFeT 1-0, and NBiFeT 2-0. The adsorption capability of NBiFeT 0-0 is the weakest, engendering the smallest observed $\Delta C/C_0$ value of 7% after 80 minutes of stirring in the absence of light. However, the nanosheets demonstrate a pronounced affinity for adsorbing RhB dyes in the absence of light after Fe doping, i.e., NBiFeT x-0 (x=1,2). It is evident that the Fe doping plays an important role in the adsorption capability. As shown in Figure 5.1, NBiFeT 1-0 adsorbs 67% of RhB within the initial 30 seconds of stirring and the adsorption becomes saturated after 5 minutes of stirring. Nonetheless, as the Fe doping increases, i.e., for NBiFeT 2-0, the adsorption decreases, giving a lower observed $\Delta C/C_0$ value of 18%, after

80 minutes of stirring in the dark. As discussed in Chapter 3, the surface area increases with increasing the Fe doping level. Notably, the NBiFeT 2-0 nanosheet shows a larger surface area coupled with a smaller particle size. The adsorption reduction observed in NBiFeT 2-0 as compared with NBiFeT 1-0 should not be resulted from the difference in specific surface areas of the nanosheets. As shown in Chapter 3, the main diffraction peaks of NBiFeT 2-0 shift towards the lower 2θ values (Fig. 3.7). The shift should be attributed to the differences in ionic radius and valence between the host ion Ti^{4+} and the dopant Fe^{3+}. The introduction of dopants leads to an expansion of the interplanar (d) distance within the doped material. Therefore, it is suggest that the reduced adsorption capability of NBiFeT 2-0, should be resulted from the retardation of dye molecules in pore channels that physically prevent RhB molecules from diffusing into the liquid to enter into the assembly of particles [49].

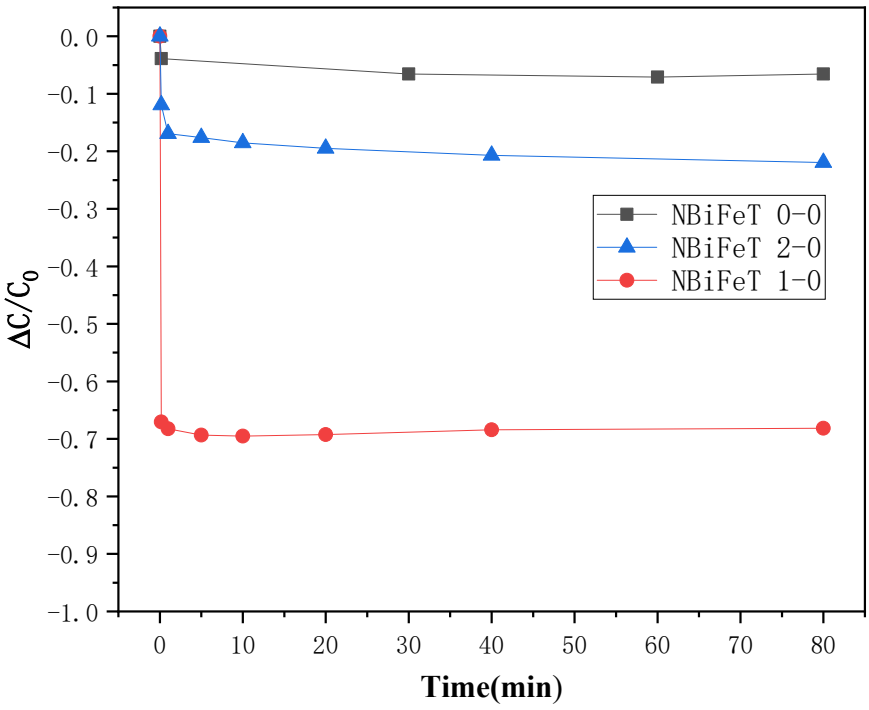

Figure 5.1 ($\Delta C/C_0$) plots for adsorption process of NBiFeT x-0 (x=0,1,2) nanosheets.

5.3. Adsorption capability of excess Fe-doped NBiFeT nanosheets

As discussed above, the NBiFeT 1-0 nanosheets show the best capability in adsorption of RhB. Therefore, they are selected as the base material for studying the effect of excess Fe doping on the adsorption capability. In this study, the NBiFeT 1-y (y=0,0.5,1,2) nanosheets have been used as the adsorbent to adsorb RhB, giving the results shown in Figure 5.2. It can be seen the observed $\Delta C/C_0$ for all the adsorbents becomes saturated after 20 minutes of stirring in the absence of light. The maximum dark adsorption of NBiFeT 1-0, NBiFeT 1-0.5, NBiFeT 1-1 and NBiFeT 1-2 are 70%, 88%, 92% and 92%, respectively. These results show that the adsorption capability is enhanced significantly after the excess Fe doping. This may be due to the average particles size and the BFO produced. As discussed before, the excess Fe doping will decrease the particle size that may increase the adsorption capability. The average particle size of NBiFeT 1-0 (3.82μm) decreases successively to 0.58 μm, 0.35 μm, and 0.32 μm, respectively, as the excess Fe doping increase from 0 to 2, i.e., NBiFeT 1-0.5, NBiFeT 1-1 and NBiFeT 1-2. A recent research work has reported that carbon fibers coated with $BiFeO_3$ particles can enhance its adsorption capability [82]. For the excess Fe-doped NBiFeT nanosheets, distinct diffraction peaks corresponding to the $BiFeO_3$ phase have been observed at 22.4° and 32°, respectively, (Fig. 3.12). To conclude, as excess Fe doping increases, the particle size of the NBiFeT 1-0 nanosheets decreases because of the accumulation of dopants, which can impede the particle growth. Furthermore, a higher level of Fe doping provides

more chances for Fe to react with Bi to form BFO at the surfaces of the nanosheets. The BFO particles can enhance the adsorption capability.

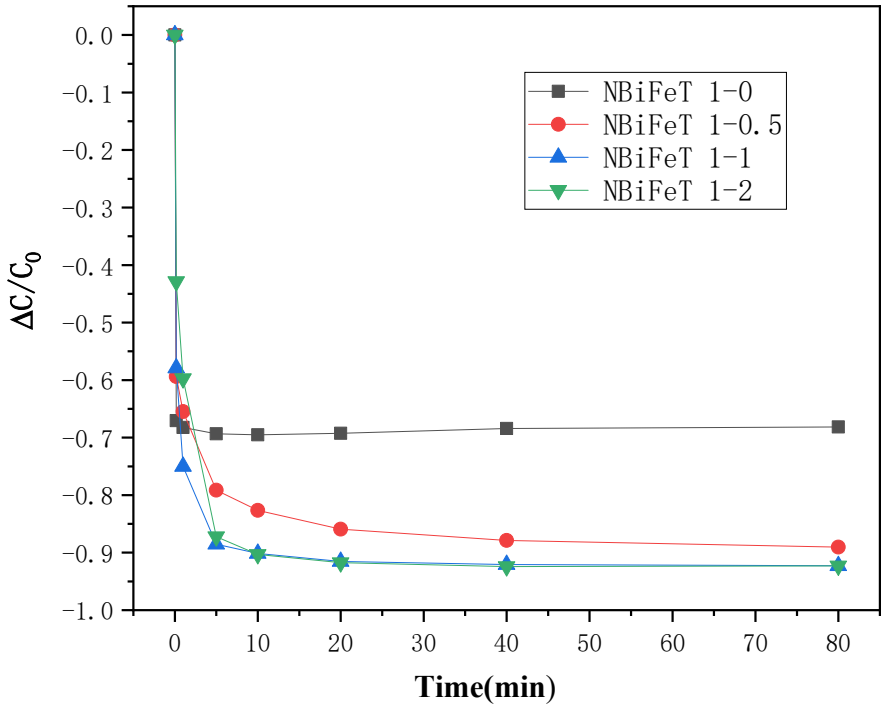

Figure 5.2 Δ(C/C0) plots for adsorption process of NBiFeT 1-y (y=0, 0.5, 1, 2).

5.4. The effect of pH value in adsorption capability

During the adsorption process, the pH value of the solution exerts a significant influence due to its impact on the characteristics of the adsorbent surface. Because of the enhanced adsorption capability, the NBiFeT 1-1 nanosheets are employed as the adsorbent for investigating the influence of the solution pH value. The results of the adsorption experiments, involving variations in pH values ranging from 4.7 to 11, are shown in Figure 5.3. The figure reveals that the pH value of the RhB solution significantly impacts the adsorption capability of the NBiFeT 1-1 nanosheets. At a pH value of 11, no discernible

adsorption is observed. This should be attributed to the substantial presence of hydroxyl groups in the alkaline environment, which hinders the occurrence of adsorption processes. This result is the same as that of photocatalytic performance in an alkaline environment. Furthermore, it is noteworthy that the adsorption capability of NBiFeT 1-1 exhibits a minor increment at pH 4.7 in comparison to that at pH 7.1. This should be attributed to the protonation of the nanosheets' surfaces, resulting in positively charged surfaces. At a pH value of 4.7, an attractive interaction occurs between the deprotonated carboxyl group and the slightly protonated surfaces of the nanosheets [97] .

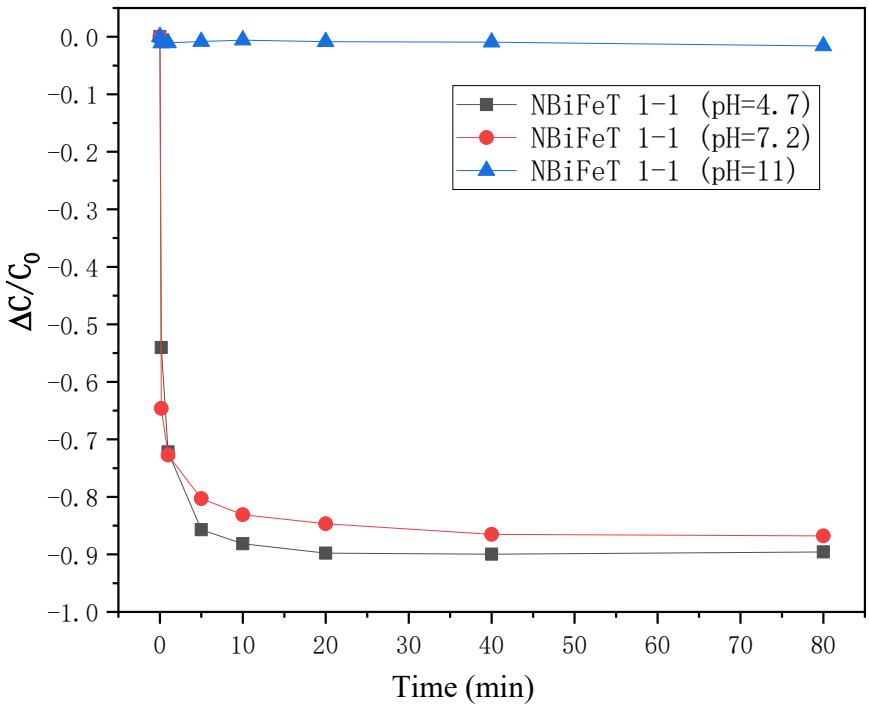

Figure 5.3 Δ(C/C0) plots for adsorption process of NBiFeT 1-1 nanosheets under different pH value.

5.5. Magnetic modification experiment

The NBiFeT x-y nanosheets exhibit paramagnetic behavior at room temperature, which is not conducive to magnetic recyclability. As mentioned, an efficient adsorbent should exhibit characteristics that allow for easy separation and recovery. Consequently, Ni and Eu are added as substitutes for Fe in the NBiFeT 1-1 nanosheets to enhance their magnetic properties. Figure 5.4a shows the magnetic hysteresis (M-H) loop of the NBiFeT 1-1 nanosheets doped with 0.1 mol of Ni and 0.1 mol of Eu. It is evident that there is a substantial enhancement in the saturation magnetization, M_s, after the addition of Ni and Eu. The observed M_s reaches 1.22 emu/g about 9 times higher than that of the undoped NBiFeT 1-1 nanosheets (0.12 emu/g). Figure 5.4b shows the photograph of the solution containing the Ni,Eu-doped nanosheets placed nearby a magnet several minutes later. This photo illustrates the straightforward recovery of the NBiFeT 1-1 nanosheets through magnetic means. However, Figure 5.4c shows the comparison of the adsorption capability of the Ni,Eu-doped NBiFeT 1-1 nanosheets and undoped nanosheets. It shows that the adsorption capability decreases from 92% to 81% after enhancing the magnetism.

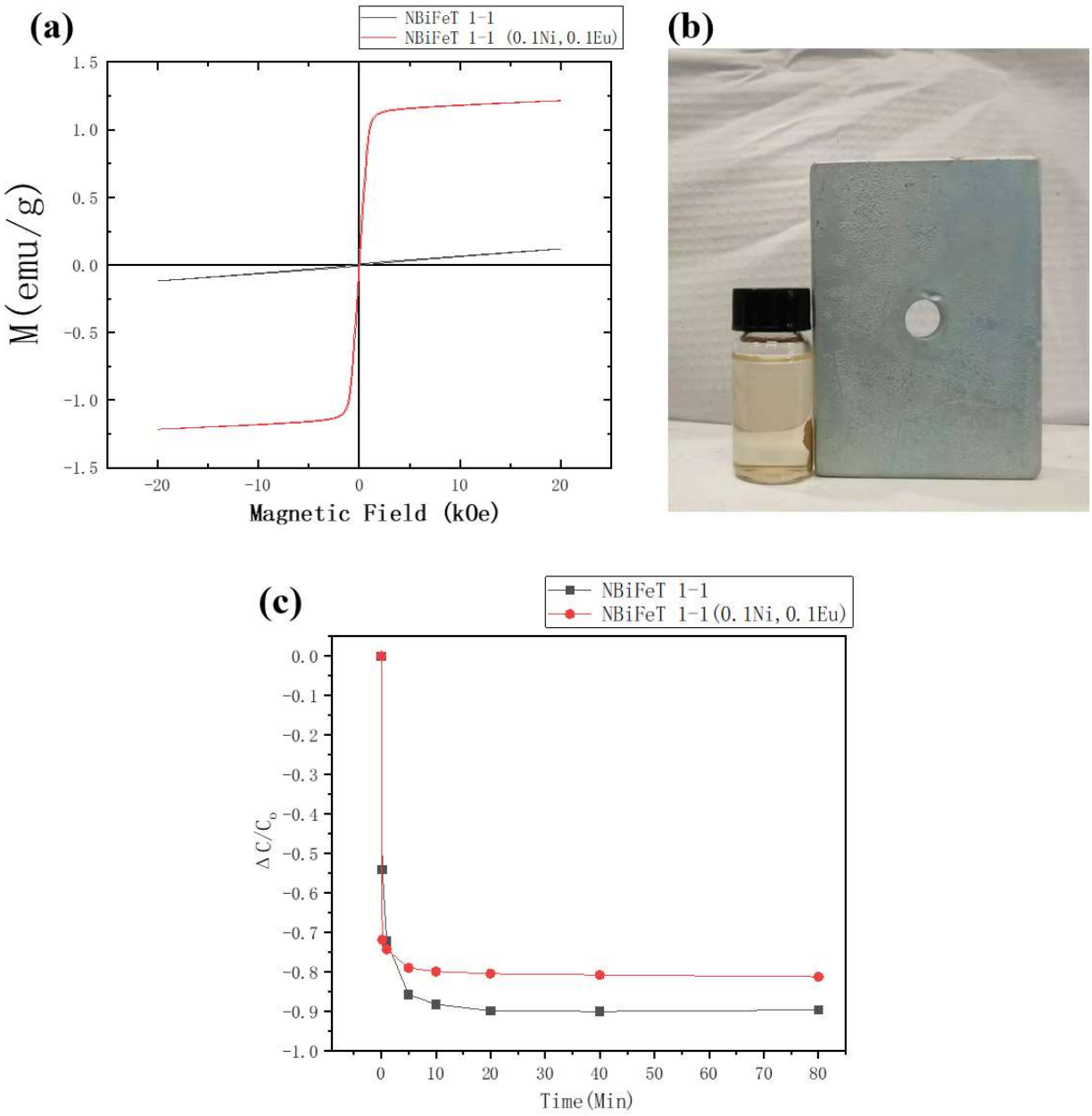

Figure 5.4 (a) M-H hysteresis loops of NBiFeT 1-1 nanosheets. (b) photograph capturing the solution placed in close proximity to a magnet for several minutes.(c) adsorption capability between Ni, Eu-doped NBiFeT 1-1 and the undoped sample.

5.6. Conclusion

The adsorption capability of Fe doped and excess Fe doped NBiFeT nanosheets are investigated. Among all the nanosheets, NBiFeT 1-1 shows the strongest adsorption capability, engendering a maximum RhB adsorption 92% after 80 minutes of stirring in the dark.

The Fe doping plays an important role in adsorption capability. After Fe doping with 1 mol of Fe, the adsorption capability increases from 7% (NBiFeT 0-0) to 67% (NBiFeT 1-0). This should be due to the increase in surface area after Fe doping. However, despite the larger surface area of the nanosheets doped with 2 mol of Fe (NBiFeT 2-0), the adsorption capability becomes weaker. The diminished adsorption capability observed in NBiFeT 2-0 nanosheets should be attributed to the retardation caused by the RhB molecules within the pore channels. This hindrance physically obstructs the diffusion of RhB molecules in the solution, impeding their entry into the nanosheets from the surfaces.

The effect of excess Fe doping on adsorption has also been investigated. The results show that the adsorption capability increases with increasing the level of excess Fe doping. This should be contributed to the high concentration of Fe which reacts with Bi to form $BiFeO_3$ in the synthesis process. The BFO growths on the surfaces of the NBiFeT nanosheets and enhances the adsorption capability. Moreover, the decrease in particles size arisen from the after excess Fe doping also enhances the adsorption capability.

In addition, the pH value of the RhB solution also affect the adsorption capability. In an alkaline system, the adsorption reaction is harder to occur since the presence of a large amount of hydroxyl group. On the other hand, the adsorption capability increased

in an acidic system. The surface of the nanosheet is protonated in an acidic system that attracting the deprotonated carboxyl groups.

Finally, Ni and Eu are doped as substitutes for Fe in the NBiFeT 1-1 nanosheets to enhance their magnetic properties. This augmentation yields a pronounced increase in the saturation magnetization. Specifically, the M_s value increases from 0.12 emu/g to 1.22 emu/g after doping with 0.1 mol of Ni and 01 mol of Eu. However, the adsorption capability of NBiFeT 1-1 decreases from 92% to 81% after enhancing the magnetism.

Chapter 6 Conclusion

This study demonstrates the excellent performances of Fe-doped NBiFeT nanosheets in photocatalytic degradation and adsorption capability. It shows that the photocatalytic performance and adsorption capability of the NBiFeT nanosheets can be improved by the Fe doping. Fe doping plays an important role in adsorption. Among the samples, the NBiFeT 0-0 (undoped with Fe) nanosheets exhibits an excellent performance in the photocatalytic degradation while the NBiFeT 1-1 (doped with 1 mol of Fe and 1 mol of excess Fe) nanosheets exhibits an excellent performance in adsorption. The NBiFeT x-y nanosheets has been effectively synthesized using different salt-to-product ratios by the molten salt synthesis technique. The optimal salt-to-product ratio has been identified, based on a comprehensive scanning electron microscope (SEM) analysis, as 1:60:60. As substantiated by X-ray diffraction (XRD) patterns, all the NBiFeT nanosheets have the standard crystal structure of $Na_{0.5}Bi_{4.5}Ti_4O_{15}$. Furthermore, after the doping of Fe (exact), an expansion of the lattice spacing of NBiFeT nanosheets is resulted, leading to a noticeable shift of the XRD pattern towards lower 2θ values. Additionally, the doping induces a reduction in the particle size. Remarkably, a pivotal discovery is that the excessive incorporation of Fe prompts the formation of $BiFeO_3$ (BFO), consequently augmenting the adsorption performance. The TEM analysis shows that the exposed plane of the NBiFeT 0-0 nanosheets is primarily {001} facet. The investigations also reveal the ferroelectric nature of NBiFeT 0-0, in the form of

ceramic disk for the ease of dielectric properties and P-E loop measurements. As the temperature increases from room temperature to 100°C, observed remnant polarization (P_r) increase from 0.3 μC/cm² to 1.39 μC/cm², while the observed saturated polarization (P_s) from 1.4 μC/cm² to 3.3 μC/cm². When Fe or an excess amount of Fe is doped into the NBiFeT 0-0 nanosheets, the band gap decreases significantly.

The photocatalytic performances of undoped and Fe-doped NBiFeT nanosheets have been investigated. The findings demonstrate a substantial degradation rate of 98% for RhB after 180 minutes of irradiation, utilizing NBiFeT 0-0 nanosheets as the photocatalyst. Throughout the course of the photocatalytic degradation process, a noticeable hypochromic shift is observed in the absorption maximum of the RhB solution. It is due to the de-ethylation process of RhB which can be considered as the indicator of the photocatalytic degradation process. Subsequently, based on the results of crystal structure, morphology and degradation efficiency, the photocatalytic mechanism of the NBiFeT 0-0 nanosheets has been suggested. The investigation indicates that the inherent spontaneous polarization within the NBiFeT x-y nanosheets contributes to the enhancement of their photocatalytic performance. Furthermore, an exploration into the photocatalytic performance of Fe-doped NBiFeT 0-0 nanosheets is conducted. The degradation efficiency of RhB for NBiFeT 1-0 and NBiFeT 2-0 are 92% and 67%, respectively. The degradation of RhB decreases with increasing the Fe doping. This should be attributed to the high concentration of Fe^{3+} ions, which function as recombination

centers for photogenerated charge carriers, consequently hampering the overall photocatalytic activity. The effect of excessive Fe doping on photocatalytic degradation has also been investigated. The degradation efficiency of RhB is measured as 98%, 96% and 90% for NBiFeT 0-0, NBiFeT 0-0.5 and NBiFeT 0-2, respectively. The results highlight a decrease in photocatalytic performance as the level of excess Fe doping increases. This trend should be attributed to the elevated concentration of Fe^{3+} ions, which is consistent with the effect observed in the case of Fe doping on photocatalytic performance. After that, trapping experiments have been carried out to identify the primary active specie involved in the photocatalytic processes. The results strongly suggest that superoxide radicals ($\bullet O_2^-$) primarily contribute to the RhB photocatalytic degradation. Then, the influence of solution pH on photocatalytic performance is thoroughly examined. Specifically, at a pH of 7.1, the surface activity of the NBiFeT 0-0 nanosheets exhibit optimal behavior. Conversely, under an alkaline environment, the abundance of hydroxyl groups (OH^-) hinders the occurrence of the adsorption.

The adsorption capability of Fe-doped NBiFeT 1-0 nanosheets have been investigated. Among all the nanosheets, NBiFeT 1-1 nanosheets exhibit the excellent adsorption capability. The maximum adsorption of RhB reaches 92% within 80 minutes of dark adsorption. The adsorption capability increases after Fe doping; the adsorption efficiency of NBiFeT 0-0 is 7%, while that of NBiFeT 1-0 is 67%. However, the maximum adsorption of NBiFeT 2-0 is measured at 22%. The decrease in adsorption observe in NBiFeT 2-0 nanosheets should be attributed to the retardation caused by RhB

molecules within the pore channels. This hindrance physically obstructs the diffusion of RhB molecules in the solution, thereby impeding their ingress into the nanosheets from the surface. Furthermore, the effect of excess Fe doping on the adsorption is examined utilizing NBiFeT 1-0 nanosheets. The results demonstrate an augmentation in adsorption capability with the escalation of excess Fe doping. This phenomenon should be attributed to the higher concentration of Fe, which has the potential to react with Bi during the synthesis process, leading to the formation of $BiFeO_3$. The growths of $BiFeO_3$ on the surface of NBiFeT nanosheets subsequently enhance the adsorption capability. Additionally, the pH values of the RhB solution also exert an effect on adsorption. In an alkaline system, the occurrence of the adsorption reaction becomes more challenging due to the prevalence of a substantial amount of hydroxyl groups. This should be attributed the repulsion of the nanosheets and deprotonated RhB dye. Conversely, the adsorption capability experiences an increment in an acidic environment. This should be attributed to the protonation of the adsorbent's surface in an acidic environment, resulting in the development of a positive charge on the surface. Lastly, the 0.1 mol of Ni and 0.1 mol of Eu are doped into the NBiFeT 1-1 nanosheets to enhance their magnetic properties. The M_s value exhibits a notable rise, transitioning from 0.12 emu/g to 1.22 emu/g subsequent after Ni, Eu doping. However, it is noteworthy that the maximum adsorption of NBiFeT 1-1 experiences a reduction from 92% to 81% following the enhancement of the magnetism.

To conclude, our result shows that Fe doping plays an important role in the performance of photocatalytic and adsorption. The NBiFeT 0-0 nanosheets have the well performance in photocatalytic degradation process and NBiFeT 1-1 nanosheets have a good performance in adsorption. Also, it shows a new path to enhance the adsorption capability by the weak adsorption material by controlling the content of excessive dopant.

Reference

[1] M. T. Yagub, T. K. Sen, S. Afroze, and H. M. Ang, 'Dye and its removal from aqueous solution by adsorption: A review', *Adv. Colloid Interface Sci.*, vol. 209, pp. 172–184, Jul. 2014, doi: 10.1016/j.cis.2014.04.002.

[2] T. K. Sen, S. Afroze, and H. M. Ang, 'Equilibrium, Kinetics and Mechanism of Removal of Methylene Blue from Aqueous Solution by Adsorption onto Pine Cone Biomass of Pinus radiata', *Water. Air. Soil Pollut.*, vol. 218, no. 1–4, pp. 499–515, Jun. 2011, doi: 10.1007/s11270-010-0663-y.

[3] M. H. Han and Y.-S. Yun, 'Mechanistic understanding and performance enhancement of biosorption of reactive dyestuffs by the waste biomass generated from amino acid fermentation process', *Biochem. Eng. J.*, vol. 36, no. 1, pp. 2–7, Aug. 2007, doi: 10.1016/j.bej.2006.06.010.

[4] Y. L. Pang and A. Z. Abdullah, 'Current Status of Textile Industry Wastewater Management and Research Progress in Malaysia: A Review', *CLEAN - Soil Air Water*, vol. 41, no. 8, pp. 751–764, Aug. 2013, doi: 10.1002/clen.201000318.

[5] E. A. Clarke and R. Anliker, 'Organic Dyes and Pigments', in *Anthropogenic Compounds*, vol. 3 / 3A, in The Handbook of Environmental Chemistry, vol. 3 / 3A. , Berlin, Heidelberg: Springer Berlin Heidelberg, 1980, pp. 181–215. doi: 10.1007/978-3-540-38522-6_7.

[6] K. Kadirvelu, M. Kavipriya, C. Karthika, M. Radhika, N. Vennilamani, and S. Pattabhi, 'Utilization of various agricultural wastes for activated carbon preparation and application for the removal of dyes and metal ions from aqueous solutions', *Bioresour. Technol.*, vol. 87, no. 1, pp. 129–132, Mar. 2003, doi: 10.1016/S0960-8524(02)00201-8.

[7] T. L. Silva, A. L. Cazetta, P. S. C. Souza, T. Zhang, T. Asefa, and V. C. Almeida, 'Mesoporous activated carbon fibers synthesized from denim fabric waste: Efficient adsorbents for removal of textile dye from aqueous solutions', *J. Clean. Prod.*, vol. 171, pp. 482–490, Jan. 2018, doi: 10.1016/j.jclepro.2017.10.034.

[8] ��Ngela Anglada, A. Urtiaga, and I. Ortiz, 'Contributions of electrochemical oxidation to waste-water treatment: fundamentals and review of applications', *J. Chem. Technol. Biotechnol.*, vol. 84, no. 12, pp. 1747–1755, Dec. 2009, doi: 10.1002/jctb.2214.

[9] S. M. Ghoreishi and R. Haghighi, 'Chemical catalytic reaction and biological oxidation for treatment of non-biodegradable textile effluent', *Chem. Eng. J.*, vol. 95, no. 1–3, pp. 163–169, Sep. 2003, doi: 10.1016/S1385-8947(03)00100-1.

[10] R. Guo, L. Fang, W. Dong, F. Zheng, and M. Shen, 'Enhanced Photocatalytic Activity and Ferromagnetism in Gd Doped $BiFeO_3$ Nanoparticles', *J. Phys. Chem. C*, vol. 114, no. 49, pp. 21390–21396, Dec. 2010, doi: 10.1021/jp104660a.

[11] L. Qifeng, M. Jingjun, M. Sharma, and R. Vaish, 'Photocatalytic, piezocatalytic, and piezo-photocatalytic effects in ferroelectric (Ba $_{0.875}$ Ca $_{0.125}$)(Ti $_{0.95}$ Sn $_{0.05}$)O $_3$ ceramics', *J. Am. Ceram. Soc.*, vol. 102, no. 10, pp. 5807–5817, Oct. 2019, doi: 10.1111/jace.16502.

[12] M. A. Khan, M. A. Nadeem, and H. Idriss, 'Ferroelectric polarization effect on surface chemistry and photo-catalytic activity: A review', *Surf. Sci. Rep.*, vol. 71, no. 1, pp. 1–31, Mar. 2016, doi: 10.1016/j.surfrep.2016.01.001.

[13] F. Liu, X. Zhuang, Z. Du, Y. Dan, Y. Huang, and L. Jiang, 'Enhanced photocatalytic performance by polarizing ferroelectric KNbO3 for degradation of plastic wastes under mild conditions', *Appl. Catal. B Environ.*, vol. 318, p. 121897, Dec. 2022, doi: 10.1016/j.apcatb.2022.121897.

[14] M. Stock and S. Dunn, 'Influence of the Ferroelectric Nature of Lithium Niobate to Drive Photocatalytic Dye Decolorization under Artificial Solar Light', *J. Phys. Chem. C*, vol. 116, no. 39, pp. 20854–20859, Oct. 2012, doi: 10.1021/jp305217z.

[15] Z. Zhang, P. Sharma, C. N. Borca, P. A. Dowben, and A. Gruverman, 'Polarization-specific adsorption of organic molecules on ferroelectric LiNbO3 surfaces', *Appl. Phys. Lett.*, vol. 97, no. 24, p. 243702, Dec. 2010, doi: 10.1063/1.3525373.

[16] H. T. Yi, T. Choi, S. G. Choi, Y. S. Oh, and S.-W. Cheong, 'Mechanism of the Switchable Photovoltaic Effect in Ferroelectric BiFeO3', *Adv. Mater.*, vol. 23, no. 30, pp. 3403–3407, Aug. 2011, doi: 10.1002/adma.201100805.

[17] P. Lunkenheimer *et al.*, 'Multiferroicity in an organic charge-transfer salt that is suggestive of electric-dipole-driven magnetism', *Nat. Mater.*, vol. 11, no. 9, pp. 755–758, Sep. 2012, doi: 10.1038/nmat3400.

[18] D. Damjanovic, 'Ferroelectric, dielectric and piezoelectric properties of ferroelectric thin films and ceramics', *Rep. Prog. Phys.*, vol. 61, no. 9, pp. 1267–1324, Sep. 1998, doi: 10.1088/0034-4885/61/9/002.

[19] J. Wu, *Advances in Lead-Free Piezoelectric Materials*. Singapore: Springer Singapore, 2018. doi: 10.1007/978-981-10-8998-5.

[20] E. V. Alekseev *et al.*, 'K[AsW2O9], the first member of the arsenate–tungsten bronze family: Synthesis, structure, spectroscopic and non-linear optical properties', *J. Solid State Chem.*, vol. 204, pp. 59–63, Aug. 2013, doi: 10.1016/j.jssc.2013.04.038.

[21] C. H. Ahn, K. M. Rabe, and J.-M. Triscone, 'Ferroelectricity at the Nanoscale: Local Polarization in Oxide Thin Films and Heterostructures', *Science*, vol. 303, no. 5657, pp. 488–491, Jan. 2004, doi: 10.1126/science.1092508.

[22] A. R. Damodaran, E. Breckenfeld, Z. Chen, S. Lee, and L. W. Martin, 'Enhancement of Ferroelectric Curie Temperature in BaTiO $_3$ Films via Strain-Induced Defect Dipole Alignment', *Adv. Mater.*, vol. 26, no. 36, pp. 6341–6347, Sep. 2014, doi: 10.1002/adma.201400254.

[23] J. Jiang, K. Zhao, X. Xiao, and L. Zhang, 'Synthesis and Facet-Dependent Photoreactivity of BiOCl Single-Crystalline Nanosheets', *J. Am. Chem. Soc.*, vol. 134, no. 10, pp. 4473–4476, Mar. 2012, doi: 10.1021/ja210484t.

[24] G. Naresh and T. K. Mandal, 'Efficient COD Removal Coinciding with Dye Decoloration by Five-Layer Aurivillius Perovskites under Sunlight-Irradiation', *ACS Sustain. Chem. Eng.*, vol. 3, no. 11, pp. 2900–2908, Nov. 2015, doi: 10.1021/acssuschemeng.5b00853.

[25] S. Tu, H. Huang, T. Zhang, and Y. Zhang, 'Controllable synthesis of multi-responsive ferroelectric layered perovskite-like Bi4Ti3O12: Photocatalysis and piezoelectric-catalysis and mechanism insight', *Appl. Catal. B Environ.*, vol. 219, pp. 550–562, Dec. 2017, doi: 10.1016/j.apcatb.2017.08.001.

[26] Y. Liu, M. Zhang, L. Li, and X. Zhang, 'One-dimensional visible-light-driven bifunctional photocatalysts based on Bi4Ti3O12 nanofiber frameworks and Bi2XO6 (X=Mo, W) nanosheets', *Appl. Catal. B Environ.*, vol. 160–161, pp. 757–766, Nov. 2014, doi: 10.1016/j.apcatb.2014.06.023.

[27] H. He *et al.*, 'Size controllable synthesis of single-crystal ferroelectric Bi4Ti3O12 nanosheet dominated with {0 0 1} facets toward enhanced visible-light-driven photocatalytic activities', *Appl. Catal. B Environ.*, vol. 156–157, pp. 35–43, Sep. 2014, doi: 10.1016/j.apcatb.2014.03.003.

[28] H. Huang *et al.*, 'Bi $_2$ O $_2$ (OH)(NO $_3$) as a desirable [Bi $_2$ O $_2$] $^{2+}$ layered photocatalyst: strong intrinsic polarity, rational band structure and {001} active facets co-beneficial for robust photooxidation capability', *J. Mater. Chem. A*, vol. 3, no. 48, pp. 24547–24556, 2015, doi: 10.1039/C5TA07655B.

[29] D. S. Bhatkhande, V. G. Pangarkar, and A. A. Beenackers, 'Photocatalytic degradation for environmental applications - a review', *J. Chem. Technol. Biotechnol.*, vol. 77, no. 1, pp. 102–116, Jan. 2002, doi: 10.1002/jctb.532.

[30] Y. Guo, P. S. Qi, and Y. Z. Liu, 'A Review on Advanced Treatment of Pharmaceutical Wastewater', *IOP Conf. Ser. Earth Environ. Sci.*, vol. 63, p. 012025, May 2017, doi: 10.1088/1755-1315/63/1/012025.

[31] P. Kanhere and Z. Chen, 'A Review on Visible Light Active Perovskite-Based Photocatalysts', *Molecules*, vol. 19, no. 12, pp. 19995–20022, Dec. 2014, doi: 10.3390/molecules191219995.

[32] R. Saravanan, F. Gracia, and A. Stephen, 'Basic Principles, Mechanism, and Challenges of Photocatalysis', in *Nanocomposites for Visible Light-induced Photocatalysis*, M. M. Khan, D. Pradhan, and Y. Sohn, Eds., in Springer Series on Polymer and Composite Materials. , Cham: Springer International Publishing, 2017, pp. 19–40. doi: 10.1007/978-3-319-62446-4_2.

[33] H. Wang *et al.*, 'Semiconductor heterojunction photocatalysts: design, construction, and photocatalytic performances', *Chem. Soc. Rev.*, vol. 43, no. 15, p. 5234, Jul. 2014, doi: 10.1039/C4CS00126E.

[34] V. Subramanian, E. Wolf, and P. V. Kamat, 'Semiconductor−Metal Composite Nanostructures. To What Extent Do Metal Nanoparticles Improve the Photocatalytic Activity of TiO $_2$ Films?', *J. Phys. Chem. B*, vol. 105, no. 46, pp. 11439–11446, Nov. 2001, doi: 10.1021/jp011118k.

[35] N. Zhang, D. Chen, F. Niu, S. Wang, L. Qin, and Y. Huang, 'Enhanced visible light photocatalytic activity of Gd-doped BiFeO3 nanoparticles and mechanism insight', *Sci. Rep.*, vol. 6, no. 1, p. 26467, May 2016, doi: 10.1038/srep26467.

[36] S. Kalikeri and V. Shetty Kodialbail, 'Solar light-driven photocatalysis using mixed-phase bismuth ferrite (BiFeO3/Bi25FeO40) nanoparticles for remediation of dye-contaminated water: kinetics and comparison with artificial UV and visible light-mediated photocatalysis', *Environ. Sci. Pollut. Res.*, vol. 25, no. 14, pp. 13881–13893, May 2018, doi: 10.1007/s11356-018-1291-0.

[37] A. Mukherjee, Sk. M. Hossain, M. Pal, and S. Basu, 'Effect of Y-doping on optical properties of multiferroics BiFeO3 nanoparticles', *Appl. Nanosci.*, vol. 2, no. 3, pp. 305–310, Sep. 2012, doi: 10.1007/s13204-012-0114-8.

[38] M. Ge, Y. Li, L. Liu, Z. Zhou, and W. Chen, 'Bi_2O_3 −Bi_2WO_6 Composite Microspheres: Hydrothermal Synthesis and Photocatalytic Performances', *J. Phys. Chem. C*, vol. 115, no. 13, pp. 5220–5225, Apr. 2011, doi: 10.1021/jp108414e.

[39] B. Liao *et al.*, 'Built in electric field boosted photocatalytic performance in a ferroelectric layered material SrBi2Ta2O9 with oriented facets: Charge separation and mechanism insights', *J. Mater. Sci. Technol.*, vol. 123, pp. 222–233, Oct. 2022, doi: 10.1016/j.jmst.2022.01.023.

[40] A. Dąbrowski, 'Adsorption — from theory to practice', *Adv. Colloid Interface Sci.*, vol. 93, no. 1–3, pp. 135–224, Oct. 2001, doi: 10.1016/S0001-8686(00)00082-8.

[41] R. Agarwala and L. Mulky, 'Adsorption of Dyes from Wastewater: A Comprehensive Review', *ChemBioEng Rev.*, vol. 10, no. 3, pp. 326–335, Jun. 2023, doi: 10.1002/cben.202200011.

[42] H. Ali, 'Biodegradation of Synthetic Dyes—A Review', *Water. Air. Soil Pollut.*, vol. 213, no. 1–4, pp. 251–273, Nov. 2010, doi: 10.1007/s11270-010-0382-4.

[43] G. Crini, 'Non-conventional low-cost adsorbents for dye removal: A review', *Bioresour. Technol.*, vol. 97, no. 9, pp. 1061–1085, Jun. 2006, doi: 10.1016/j.biortech.2005.05.001.

[44] S. E. Bailey, T. J. Olin, R. M. Bricka, and D. D. Adrian, 'A review of potentially low-cost sorbents for heavy metals', *Water Res.*, vol. 33, no. 11, pp. 2469–2479, Aug. 1999, doi: 10.1016/S0043-1354(98)00475-8.

[45] M. Vakili *et al.*, 'Application of chitosan and its derivatives as adsorbents for dye removal from water and wastewater: A review', *Carbohydr. Polym.*, vol. 113, pp. 115–130, Nov. 2014, doi: 10.1016/j.carbpol.2014.07.007.

[46] I. Grinberg *et al.*, 'Perovskite oxides for visible-light-absorbing ferroelectric and photovoltaic materials', *Nature*, vol. 503, no. 7477, pp. 509–512, Nov. 2013, doi: 10.1038/nature12622.

[47] M. H. Zhao, D. A. Bonnell, and J. M. Vohs, 'Effect of ferroelectric polarization on the adsorption and reaction of ethanol on BaTiO3', *Surf. Sci.*, vol. 602, no. 17, pp. 2849–2855, Sep. 2008, doi: 10.1016/j.susc.2008.07.011.

[48] Y. Yun and E. I. Altman, 'Using Ferroelectric Poling to Change Adsorption on Oxide Surfaces', *J. Am. Chem. Soc.*, vol. 129, no. 50, pp. 15684–15689, Dec. 2007, doi: 10.1021/ja0762644.

[49] W. J. Tseng and R.-D. Lin, 'BiFeO3/α-Fe2O3 core/shell composite particles for fast and selective removal of methyl orange dye in water', *J. Colloid Interface Sci.*, vol. 428, pp. 95–100, Aug. 2014, doi: 10.1016/j.jcis.2014.04.040.

[50] B. Nandi, A. Goswami, and M. Purkait, 'Removal of cationic dyes from aqueous solutions by kaolin: Kinetic and equilibrium studies', *Appl. Clay Sci.*, vol. 42, no. 3–4, pp. 583–590, Jan. 2009, doi: 10.1016/j.clay.2008.03.015.

[51] S. Chowdhury, S. Chakraborty, and P. Saha, 'Biosorption of Basic Green 4 from aqueous solution by Ananas comosus (pineapple) leaf powder', *Colloids Surf. B Biointerfaces*, vol. 84, no. 2, pp. 520–527, Jun. 2011, doi: 10.1016/j.colsurfb.2011.02.009.

[52] E. A. Al-Maliky, H. A. Gzar, and M. G. Al-Azawy, 'Determination of Point of Zero Charge (PZC) of Concrete Particles Adsorbents', *IOP Conf. Ser. Mater. Sci. Eng.*, vol. 1184, no. 1, p. 012004, Sep. 2021, doi: 10.1088/1757-899X/1184/1/012004.

[53] G. Sharifzade, A. Asghari, and M. Rajabi, 'Highly effective adsorption of xanthene dyes (rhodamine B and erythrosine B) from aqueous solutions onto lemon citrus peel active carbon: characterization, resolving analysis, optimization and mechanistic studies', *RSC Adv.*, vol. 7, no. 9, pp. 5362–5371, 2017, doi: 10.1039/C6RA23157H.

[54] C. Hu *et al.*, 'Efficient dye-removal via Ni-decorated graphene oxide-carbon nanotube nanocomposites', *Mater. Chem. Phys.*, vol. 260, p. 124117, Feb. 2021, doi: 10.1016/j.matchemphys.2020.124117.

[55] F. Deng and Z. Xu, 'Heteroatom-substituted rhodamine dyes: Structure and spectroscopic properties', *Chin. Chem. Lett.*, vol. 30, no. 10, pp. 1667–1681, Oct. 2019, doi: 10.1016/j.cclet.2018.12.012.

[56] R. Jain, M. Mathur, S. Sikarwar, and A. Mittal, 'Removal of the hazardous dye rhodamine B through photocatalytic and adsorption treatments', *J. Environ. Manage.*, vol. 85, no. 4, pp. 956–964, Dec. 2007, doi: 10.1016/j.jenvman.2006.11.002.

[57] 'Review of Using Rhodamine B as a Marker for Wildlife Studies', 2023.

[58] N. Pourreza, S. Rastegarzadeh, and A. Larki, 'Micelle-mediated cloud point extraction and spectrophotometric determination of rhodamine B using Triton X-100', *Talanta*, vol. 77, no. 2, pp. 733–736, Dec. 2008, doi: 10.1016/j.talanta.2008.07.031.

[59] M. Rochkind, S. Pasternak, and Y. Paz, 'Using Dyes for Evaluating Photocatalytic Properties: A Critical Review', *Molecules*, vol. 20, no. 1, pp. 88–110, Dec. 2014, doi: 10.3390/molecules20010088.

[60] F. Wang, I. Grinberg, and A. M. Rappe, 'Band gap engineering strategy via polarization rotation in perovskite ferroelectrics', *Appl. Phys. Lett.*, vol. 104, no. 15, p. 152903, Apr. 2014, doi: 10.1063/1.4871707.

[61] Y. Yuan, Z. Xiao, B. Yang, and J. Huang, 'Arising applications of ferroelectric materials in photovoltaic devices', *J Mater Chem A*, vol. 2, no. 17, pp. 6027–6041, 2014, doi: 10.1039/C3TA14188H.

[62] S. Iqbal *et al.*, 'The electrochemical, dielectric, and ferroelectric properties of Gd and Fe doped LaNiO3 with an efficient solar-light driven catalytic activity to oxidize malachite green dye', *J. Colloid Interface Sci.*, vol. 607, pp. 568–583, Feb. 2022, doi: 10.1016/j.jcis.2021.08.209.

[63] J. P. Zuniga, M. Abdou, S. K. Gupta, and Y. Mao, 'Molten-Salt Synthesis of Complex Metal Oxide Nanoparticles', *J. Vis. Exp.*, no. 140, p. 58482, Oct. 2018, doi: 10.3791/58482.

[64] B. J. Inkson, 'Scanning electron microscopy (SEM) and transmission electron microscopy (TEM) for materials characterization', in *Materials Characterization Using Nondestructive Evaluation (NDE) Methods*, Elsevier, 2016, pp. 17–43. doi: 10.1016/B978-0-08-100040-3.00002-X.

[65] D. Titus, E. James Jebaseelan Samuel, and S. M. Roopan, 'Nanoparticle characterization techniques', in *Green Synthesis, Characterization and Applications of Nanoparticles*, Elsevier, 2019, pp. 303–319. doi: 10.1016/B978-0-08-102579-6.00012-5.

[66] 'The structure of some crystals as indicated by their diffraction of X-rays', *Proc. R. Soc. Lond. Ser. Contain. Pap. Math. Phys. Character*, vol. 89, no. 610, pp. 248–277, Sep. 1913, doi: 10.1098/rspa.1913.0083.

[67] E. Soergel, 'Piezoresponse force microscopy (PFM)', *J. Phys. Appl. Phys.*, vol. 44, no. 46, p. 464003, Nov. 2011, doi: 10.1088/0022-3727/44/46/464003.

[68] Y. Liu, Y. Zhang, M.-J. Chow, Q. N. Chen, and J. Li, 'Biological Ferroelectricity Uncovered in Aortic Walls by Piezoresponse Force Microscopy', *Phys. Rev. Lett.*, vol. 108, no. 7, p. 078103, Feb. 2012, doi: 10.1103/PhysRevLett.108.078103.

[69] M. Naderi, 'Surface Area', in *Progress in Filtration and Separation*, Elsevier, 2015, pp. 585–608. doi: 10.1016/B978-0-12-384746-1.00014-8.

[70] S. Brunauer, P. H. Emmett, and E. Teller, 'Adsorption of Gases in Multimolecular Layers', *J. Am. Chem. Soc.*, vol. 60, no. 2, pp. 309–319, Feb. 1938, doi: 10.1021/ja01269a023.

[71] P. Makuła, M. Pacia, and W. Macyk, 'How To Correctly Determine the Band Gap Energy of Modified Semiconductor Photocatalysts Based on UV–Vis Spectra', *J. Phys. Chem. Lett.*, vol. 9, no. 23, pp. 6814–6817, Dec. 2018, doi: 10.1021/acs.jpclett.8b02892.

[72] L. Hu, Y. Zhang, W. Lu, Y. Lu, and H. Hu, 'Easily recyclable photocatalyst Bi2WO6/MOF/PVDF composite film for efficient degradation of aqueous refractory organic pollutants under visible-light irradiation', *J. Mater. Sci.*, vol. 54, no. 8, pp. 6238–6257, Apr. 2019, doi: 10.1007/s10853-018-03302-w.

[73] Y. Kan, X. Jin, P. Wang, Y. Li, Y.-B. Cheng, and D. Yan, 'Anisotropic grain growth of Bi4Ti3O12 in molten salt fluxes', *Mater. Res. Bull.*, vol. 38, no. 4, pp. 567–576, Mar. 2003, doi: 10.1016/S0025-5408(03)00029-1.

[74] H. He, W. Yao, C. Wang, X. Feng, and X. Lu, 'Morphology-Controlled Synthesis of Sodium Hexa-Titanate Nanowhiskers by Changing Evaporation Rate of NaCl–KCl Molten Salts', *Ind. Eng. Chem. Res.*, vol. 52, no. 43, pp. 15034–15040, Oct. 2013, doi: 10.1021/ie402630h.

[75] R. Hailili *et al.*, 'Oxygen vacancies induced visible-light photocatalytic activities of CaCu3Ti4O12 with controllable morphologies for antibiotic degradation', *Appl. Catal. B Environ.*, vol. 221, pp. 422–432, Feb. 2018, doi: 10.1016/j.apcatb.2017.09.026.

[76] N. H. Yusoff, R. A. M. Osman, M. S. Idris, K. N. D. K. Muhsen, and N. I. M. Nor, 'Dielectric and structural analysis of hexagonal and tetragonal phase BaTiO3', presented at the THE 2ND INTERNATIONAL CONFERENCE ON APPLIED PHOTONICS AND ELECTRONICS 2019 (InCAPE 2019), Putrajaya, Malaysia, 2020, p. 020038. doi: 10.1063/1.5142130.

[77] J. Yao, X. Rao, P. Du, W. Li, X. Mao, and L. Luo, 'Structural, electrical and photochromic properties of Na0.5Bi4.5Ti4O15:xEr3+ ferroelectric ceramics', *Ceram. Int.*, vol. 48, no. 9, pp. 12350–12358, May 2022, doi: 10.1016/j.ceramint.2022.01.098.

[78] X.-P. Jiang *et al.*, 'High performance Aurivillius type Na0.5Bi4.5Ti4O15 piezoelectric ceramics with neodymium and cerium modification', *J. Adv. Ceram.*, vol. 4, no. 1, pp. 54–60, Mar. 2015, doi: 10.1007/s40145-015-0131-7.

[79] C. J. Huang, K. Li, S. Y. Wu, X. L. Zhu, and X. M. Chen, 'Variation of ferroelectric hysteresis loop with temperature in (SrxBa1−x)Nb2O6 unfilled tungsten bronze ceramics', *J. Materiomics*, vol. 1, no. 2, pp. 146–152, Jun. 2015, doi: 10.1016/j.jmat.2015.02.004.

[80] F. D. Cortés-Vega, C. Montero-Tavera, and J. M. Yañez-Limón, 'Influence of diluted Fe3+ doping on the physical properties of BaTiO3', *J. Alloys Compd.*, vol. 847, p. 156513, Dec. 2020, doi: 10.1016/j.jallcom.2020.156513.

[81] D. C. Lupascu, Y. A. Genenko, and N. Balke, 'Aging in Ferroelectrics', *J. Am. Ceram. Soc.*, vol. 89, no. 1, pp. 224–229, Jan. 2006, doi: 10.1111/j.1551-2916.2005.00663.x.

[82] S. Jiao *et al.*, 'Removal of Methylene Blue from Water by BiFeO3/Carbon Fibre Nanocomposite and Its Photocatalytic Regeneration', *Catalysts*, vol. 8, no. 7, p. 267, Jun. 2018, doi: 10.3390/catal8070267.

[83] I. C. Amaechi *et al.*, 'Ultrafast microwave-assisted hydrothermal synthesis and photocatalytic behaviour of ferroelectric Fe3+-doped BaTiO3 nanoparticles under simulated sunlight', *Catal. Today*, vol. 360, pp. 90–98, Jan. 2021, doi: 10.1016/j.cattod.2019.07.021.

[84] K. Sing, 'The use of nitrogen adsorption for the characterisation of porous materials', *Colloids Surf. Physicochem. Eng. Asp.*, vol. 187–188, pp. 3–9, Aug. 2001, doi: 10.1016/S0927-7757(01)00612-4.

[85] F. Ambroz, T. J. Macdonald, V. Martis, and I. P. Parkin, 'Evaluation of the BET Theory for the Characterization of Meso and Microporous MOFs', *Small Methods*, vol. 2, no. 11, p. 1800173, Nov. 2018, doi: 10.1002/smtd.201800173.

[86] Y. Liu *et al.*, 'Enhanced photocatalytic activity of Bi4Ti3O12 nanosheets by Fe3+-doping and the addition of Au nanoparticles: Photodegradation of Phenol and bisphenol A', *Appl. Catal. B Environ.*, vol. 200, pp. 72–82, Jan. 2017, doi: 10.1016/j.apcatb.2016.06.069.

[87] A. Nakada *et al.*, 'Conduction Band Control of Oxyhalides with a Triple-Fluorite Layer for Visible Light Photocatalysis', *J. Am. Chem. Soc.*, vol. 143, no. 6, pp. 2491–2499, Feb. 2021, doi: 10.1021/jacs.0c10288.

[88] X. Liu *et al.*, 'Charge–Ferroelectric Transition in Ultrathin $Na_{0.5}Bi_{4.5}Ti_4O_{15}$ Flakes Probed via a Dual-Gated Full van der Waals Transistor', *Adv. Mater.*, vol. 32, no. 49, p. 2004813, Dec. 2020, doi: 10.1002/adma.202004813.

[89] E. Gutmann *et al.*, 'Pyroelectrocatalytic Disinfection Using the Pyroelectric Effect of Nano- and Microcrystalline $LiNbO_3$ and $LiTaO_3$ Particles', *J. Phys. Chem. C*, vol. 116, no. 9, pp. 5383–5393, Mar. 2012, doi: 10.1021/jp210686m.

[90] Y. Sun, B. S. Eller, and R. J. Nemanich, 'Photo-induced Ag deposition on periodically poled lithium niobate: Concentration and intensity dependence', *J. Appl. Phys.*, vol. 110, no. 8, p. 084303, Oct. 2011, doi: 10.1063/1.3647752.

[91] G. Zhu *et al.*, 'Enhanced photocatalytic activity of Fe-doped Bi4O5Br2 nanosheets decorated with Au nanoparticles for pollutants removal', *Appl. Surf. Sci.*, vol. 526, p. 146760, Oct. 2020, doi: 10.1016/j.apsusc.2020.146760.

[92] Q. Zhang *et al.*, 'Perovskite LaFeO3-SrTiO3 composite for synergistically enhanced NO removal under visible light excitation', *Appl. Catal. B Environ.*, vol. 204, pp. 346–357, May 2017, doi: 10.1016/j.apcatb.2016.11.052.

[93] T. Liu *et al.*, 'Comparative study of the photocatalytic performance for the degradation of different dyes by $ZnIn_2S_4$: adsorption, active species, and pathways', *RSC Adv.*, vol. 7, no. 20, pp. 12292–12300, 2017, doi: 10.1039/C7RA00199A.

[94] F.-N. Shi *et al.*, 'pH Controlled Excellent Photocatalytic Activity of a Composite Designed from CuBi-Based Metal Organic Oxide and Graphene', *Cryst. Growth Des.*, vol. 18, no. 9, pp. 5045–5053, Sep. 2018, doi: 10.1021/acs.cgd.8b00490.

[95] X. Liu, D. Xu, D. Zhang, G. Zhang, and L. Zhang, 'Superior performance of 3 D Co-Ni bimetallic oxides for catalytic degradation of organic dye: Investigation on the effect of catalyst morphology and catalytic mechanism', *Appl. Catal. B Environ.*, vol. 186, pp. 193–203, Jun. 2016, doi: 10.1016/j.apcatb.2016.01.005.

[96] A. A. Al-Kahtani, 'Photocatalytic Degradation of Rhodamine B Dye in Wastewater Using Gelatin/CuS/PVA Nanocomposites under Solar Light Irradiation', *J. Biomater. Nanobiotechnology*, vol. 08, no. 01, pp. 66–82, 2017, doi: 10.4236/jbnb.2017.81005.

[97] O. Merka, V. Yarovyi, D. W. Bahnemann, and M. Wark, 'pH-Control of the Photocatalytic Degradation Mechanism of Rhodamine B over $Pb_3Nb_4O_{13}$', *J. Phys. Chem. C*, vol. 115, no. 16, pp. 8014–8023, Apr. 2011, doi: 10.1021/jp108637r.